Quantum Coherence in Trapped Ions

A linear rf trap for robust two-qubit gates

Oliver Corfield

Submitted in partial fulfilment of the requirements for the degree of
Doctor of Philosophy

Imperial College London · Department of Physics

January 2022

This thesis is the author's work, unless otherwise acknowledged or referenced.

Abstract

The techniques of ion trapping have been indispensable for the study of single particles and have greatly increased our understanding of the physical world. With a high degree of control over single quantum systems made possible by recent technical developments, trapped ion researchers are now looking to observe increasingly complex quantum dynamics. There is nothing fundamentally limiting the size such systems can scale to, if the remaining engineering challenges can be overcome, and there is consequently enormous potential for our understanding of physical processes on the boundary between simple quantum and large scale classical effects. The transition between quantum and classical dynamics is characterised by decoherence, which reduces the purity of quantum states as they couple to the environment. Investigation into the mechanisms of decoherence requires the development of novel tools for its classification, which motivates the experiments presented in this work. These show that multi-level coherence in the motional state of a trapped ion can be verified from interference patterns which extend the Ramsey technique. The metric uses simple operations and is shown not to be able to produce false positives, making it of interest in the study of coherence in noisy intermediate scale systems. The motional state of a trapped ion cannot be directly measured, and the scheme shows it is possible to extract information about a quantum system coupled to the measurement basis. Coherence between quantum states can enhance information processing and sensing, which is driving the development of techniques for preserving coherence in the presence of noise. This motivates the project begun in this thesis, which is to design and implement control fields for robust ion trap quantum logic. The rapid progress in the scale of ion trap devices expected in the coming years means new leaps in our understanding of the physical world could happen at any moment.

Acknowledgements

I will always be grateful to Richard Thompson for the opportunity to work in his group over the last four and a half years, and for his supervision during this time. As well as always being available to discuss the latest problem, the freedom he has given me to work independently and make mistakes has been invaluable. Richard's enthusiasm for experimental physics has been inspiring, and I cannot imagine having had a better supervisor. It is an honour to be joining the ranks of former Imperial ion trappers, and I am especially grateful to Pavel, Vincent, and Manoj for their help during our brief time together. As well as never tiring of repeating explanations, they showed me how a functioning lab operates, and set a high standard for what can be achieved in a PhD.

The work presented in this thesis would not have been possible without the combined efforts of many people. Firstly Brian Willey, who fabricated the new trap, and contributed his significant expertise to its design. Johannes Heinrich put in a huge amount of work into trapping our first ions, and without his dedication during the darker days of vacuum issues it would almost certainly not have been possible to publish results by now. Simon Webster has been vital in his development of our experimental control infrastructure, and his wide-ranging expertise has enabled us to attain our current research capacity. Jacopo Mosca Toba has built a lot of the optical systems, including the imaging system, and has done excellent work in characterising and optimising laser cooling techniques. I am also grateful for his detailed comments on this thesis. Chungsun Lee has made many valuable contributions to the experiment, not least his taming of the spectroscopy laser. The experiment was conceived by our theoretical collaborators Florian Minternt and Jake Lishman. Jake has done a huge amount of work on our published experiment, from implementation to analysis, and has been a pleasure to work with during our PhDs.

I am very grateful to everyone involved in the Quantum Systems Engineering doctoral program, not only for the opportunity they have given me to work in this exciting field, but for developing such a comprehensive and enjoyable training.

It goes without saying I am grateful to all my family for all they have given and done for me. Finally I am indebted to Gaia Chanrai for her encouragement and patience over the last 6 years.

Contents

List of Figures

List of Tables

Chapter 1

Introduction

The structure of the physical world and the fundamental laws which describe it are revealed through experimental physics. To confine the foundational particles of nature in space was therefore a long-held dream, as exemplified by Georg Lichtenburg in the 18th century who thought it “a sad situation in all our chemistry that we are unable to suspend the constituents of matter free” [1]. Progress in technology and technique have steadily increased the precision with which matter can be investigated, and advances in the control of electromagnetic fields at the beginning of the 20th century made it increasingly possible to manipulate charged particles. This enabled the filtering and focussing of ion beams, to reduce the variation in their composition and to increase the strength of interactions. Progress in the early part of the century was sporadic until spurred by industrial interest in the 1950s, when a wide range of analytical problems in chemistry and engineering prompted the rapid development of mass spectrometers [2].

In 1910 J.J. Thomson showed that positively charged beams were deflected by strong electric fields [3], and would follow a parabolic path dependent on their charge-to-mass ratio. These methods were developed by Aston to focus the beam based on its velocity [4], leading to the discovery of stable atomic isotopes. A charged particle in a uniform magnetic field will undergo cyclotron motion around the field lines. Applications of this phenomenon in electron discharge tubes were investigated by Frans Penning in the 1930s, where electrons with a velocity component parallel to the magnetic field would “describe a cycloidal path of considerable length” [5]. The magnetic field enhances radial confinement of charged particles within the tube, extending their effective interaction time. A formalism for restricting the axial degree of freedom with a harmonic electric potential was described by J.R. Pierce [6], who first used the term 'trap' to describe these emerging techniques. In 1959 Hans Dehmelt at the University of Washington applied this electric field in conjunction with a strong magnetic field to create the Penning trap. Meanwhile at Bonn, Wolfgang Paul had identified the use of electrodynamic quadrupole fields in mass filtering, eliminating the need for magnetic fields [7]. Parameters of the field could be tuned to filter particles by their charge-to-mass ratios with greatly increased resolution over existing techniques. Applying the dynamic field to the ideal hyperbolic electrodes of Pierce enabled three-dimensional confinement of charged particles by Paul's group [8], and this method had been adopted by Dehmelt in 1962 for its simplicity [9]. However developments in techniques for the preparation and measurement of atomic states were still required to fully open up the study of trapped particles.

David Wineland had worked with Dehmelt in Washington before moving to NIST in 1975, where his group oversaw a dramatic expansion in the experimental control of trapped ions. This was by driven by the development of the laser, particularly tunable dye lasers in the 1970s, which enabled prolonged confinement and observation of single particles [10], and the first observation of individual quantum systems. With this it was possible to show that Schrödinger's "ridiculous consequences", such as quantum jumps [11] and macroscopic superpositions [12], did in fact occur in nature [13]. More generally Wineland showed that there was no fundamental limit to the creation of increasingly complex quantum systems, and that the challenge lay 'only' in technical improvements. Ion traps were able to revolutionise the understanding of quantum mechanics as particles can be highly localised, with exceptional stability and strong isolation from the environment. Laser cooling techniques made it possible to reduce the three-dimensional motion of particles to the quantum ground state, shown in Paul traps by 1995 [14, 15], and in the axial [16] and radial [17] motion of a Penning trap by this group in the last few years. At this level it becomes possible to manipulate the quantum motion through interactions with the atom, enabling the creation of more complex quantum dynamics.

In his 1981 talk on "Simulating physics with computers", Richard Feynman stressed that it would only be possible to simulate complex quantum systems using quantum computation. This is because the correlations between simple quantum mechanical systems have too many variables to be efficiently simulated with a classical machine. With greater control over single trapped ions in the 1990s, interest shifted to looking at increasingly complex dynamics between ions to observe larger scale effects. More ions enable the simulation of more complex dynamics, as quantum information can be stored in the atomic states, which are coupled via shared motional modes. In 2019 IonQ revealed an 11 qubit quantum computer using fully connected trapped ion qubits, in a fully programmable machine [18]. Even more recently Rainer Blatt's group at the University of Innsbruck have built a 24 qubit device in a compact and robust system [19]. Rapid progress in the development of ion trapping techniques is underway as a result of sudden financial investment in quantum computing, due to applications in the pharmaceutical and financial industries. This will fund the development of devices that can help experimental physicists understand the quantum world with greater clarity, because, as Feynman closed his lecture, "Nature isn't classical, dammit, and if you want to make a simulation of Nature, you'd better make it quantum mechanical" [20].

1.1 Quantum Information Processing

A motivating force in the development of quantum information processing and computing was provided by the desire to elucidate the mysteries of quantum mechanics. Although computation more generally is a historic concept, modern computer science began with Alan Turing in 1936. Turing introduced the concept of a programmable computer, and showed that a Universal Turing Machine could in principle simulate any algorithm. The von Neumann architecture and development of the transistor in 1947 have resulted in a steady growth in computational power ever since, which will ultimately be limited by quantum effects [21]. However there are algorithms which cannot be run efficiently[i] on a classical computer. Operating in different computing paradigms could therefore enable certain tasks to be performed faster, given sufficient resources. In 1977 Solovay and Strassen showed that computers with access to a random number generator could efficiently perform certain tasks that were inefficient on a classical computer, hinting at the possibility of finding more fundamental computing machines [22].

This generated great interest in a definition of computing based on physical laws, leading naturally to investigations into quantum mechanical models. In 1985 David Deutsch de-

---

[i] As defined in computational complexity, runs in polynomial time with the size of the problem.

fined a Universal Quantum Computer [23], in an attempt to describe a device that could efficiently simulate any physical system. While a quantum computer could not be simulated on a classical device, there were only contrived examples to show that this new paradigm could actually solve problems that were classically infeasible until Peter Shor's work in the mid-1990s [24]. By efficiently performing Fourier transforms on a quantum device, Shor presented algorithms for solving discrete logarithms and factorising integers, the classical inefficiency of which underpins much of our current encryption protocol. The inherently counter-intuitive nature of quantum mechanics makes it difficult to design algorithms that are naturally suited to quantum devices but classically hard, and consequently there is much to be learned about the potential of quantum computers, and the quantum mechanical world itself [22]. Another interesting point made by Nielsen and Chuang in their seminal book is that while quantum computing has taught us to "think physically about computation, we can also learn to think computationally about physics". This could revolutionise our understanding of what happens when simple physical systems scale, revealing novel properties that arise in the complex dynamics of the natural world, and enabling more universal physical theories.

Bits are the fundamental unit of information in both classical and quantum computation, however quantum bits (qubits) unlike their classical counterparts can be prepared in linear combinations, or superpositions, of the two basis states. Any classical program can be implemented by a combination of bit flips, the NOT gate, and a single two-bit gate, such as the AND or XOR. Similarly, Deutsch showed that universal quantum computation was possible with the ability to manipulate the state of single qubits, and perform one type of two-qubit entangling gate [25]. As bits are physically implemented in real systems, they are subject to errors. In classical computation errors can be mitigated by redundancy, simply keeping many copies of the state of each bit, however a fundamental feature of quantum systems is that they cannot be copied, as shown by the no-cloning theorem [26]. In 1995 Peter Shor presented quantum error correcting codes which encode the state of one logical qubit in many physical qubits, and can therefore tolerate a certain amount of noise [27]. The ability to extract reliable results from noisy machines removed the last barrier to realising quantum algorithms in real quantum systems, where delicate superpositions decay over time, and as systems scale.

The criteria for building a Universal Quantum Computer were formalised in 2000 by David DiVincenzo [28], with one requirement being a universal set of gates. The highest single and entangling gate fidelities are shown in trapped ions. There are also blueprints for building scalable trapped ion architectures [29, 30], another criterion, and gates are becoming faster [31, 32]. While it is not possible to say which hardware platform will emerge as the transistor of qubits, trapped ions remain a leading platform, and the technology is entering the noisy intermediate scale quantum (NISQ) regime. Although fault tolerant quantum computation (FTQC) is a long way from reality, partly a result of the overheads incurred in error correction, it will have a transformative impact on society according to John Preskill [33]. However despite the fact that such machines do not yet exist, current noisy devices are beginning to solve useful problems describing physical processes. The theory of quantum electrodynamics describes the interaction between atoms and light, but it is not possible to solve the equations describing even very simple systems with classical computers. Trapped ion simulators in the NISQ era can observe quantum dynamics that cannot be classically simulated, such as long range interactions in the Ising model [34, 35]. They have also been able to estimate the ground state energy of water molecules [36], with the possibility of simulating fundamental particles. It is expected that a quantum computer of 50-100 qubits could offer significant insight into many body problems, as an impractical number of classical bits would be required to describe all of the entangling correlations between qubits. It is an exciting time for experimental quantum physics, and unanticipated breakthroughs could happen at any moment.

1.1.1 Robust Two–qubit Gates

A qubit realised in the electronic state of a single trapped ion can have a very long coherence time relative to the duration of individual gates, as shown by their history as atomic frequency standards. Cirac and Zoller identified a way to implement a two-qubit gate with trapped ions in 1995 [37], removing a fundamental barrier to a trapped ion quantum computer. This was followed in 1999 by the Mølmer–Sørensen (MS) gate [38], which can entangle multiple ions using a global field, and variations of this technique now dominate. Experiments over the next decade steadily increased the quality of gates, and number of ions entangled [39–43]. In 2016 two-qubit gates with fidelities around 99.9% were shown [44, 45], which approach a fault tolerant threshold, although this is hard to quantify. However these are only proof-of-principle experiments, implemented in large traps, and fidelities quickly drop below this threshold in devices with more ions. One reason for the increasing errors is that the MS gate uses linear dynamics, which require weak coupling between qubits. Entanglement between ions is mediated via their shared motion, and the mode density increases with the number of ions, exhibiting increasingly non-linear behaviour which is not typically accounted for. This presents a fundamental limit to fidelities of gates in larger trapped ion systems, motivating the project begun in this thesis: to investigate robust ion trap logic with strong coupling. The recent techniques outlined by theory collaborators [46] show that the limits of having to use weak coupling can be overcome with more complex control fields. The increasing simplicity of generating arbitrary fields means it is possible to control more complex dynamics, which suppress fundamental and realistic sources of noise, to drive further progress in the capacity of NISQ devices.

The state of a qubit $|\psi\rangle$ is described by the complex amplitudes α and β of two distinct basis states,

$$|\downarrow\rangle = \begin{bmatrix} 1 \\ 0 \end{bmatrix}, \qquad \text{and} \qquad |\uparrow\rangle = \begin{bmatrix} 0 \\ 1 \end{bmatrix}, \qquad |\psi\rangle = \alpha\,|\downarrow\rangle + \beta\,|\uparrow\rangle\,. \tag{1.1.1}$$

Being a probability, the amplitudes are normalised by $|\alpha|^2 + |\beta|^2 = 1$, and the qubit state can therefore be described by a unit vector in a two-dimensional Hilbert space. Measurement of a quantum system collapses the superposition into one of the states, with the probability given by the square modulus of the amplitude. The interference between state probability amplitudes as the system evolves unmeasured distinguishes quantum information processing from its classical equivalent, and it is this “hidden information” from which quantum computing derives its power [22]. A state $|\psi\rangle$ evolves under single qubit operations, and any manipulation, or rotation of the state vector, can be expressed by the Pauli matrices,

$$\sigma_x = \begin{bmatrix} 0 & 1 \\ 1 & 0 \end{bmatrix}, \qquad \sigma_y = \begin{bmatrix} 0 & -i \\ i & 0 \end{bmatrix}, \qquad \sigma_z = \begin{bmatrix} 1 & 0 \\ 0 & -1 \end{bmatrix}. \tag{1.1.2}$$

A composite system, such as two coupled qubits, can be described by a product state, expressed as a sum of tensor products

$$|\Psi\rangle = [\alpha_1 |{\downarrow}\rangle_1 + \beta_1 |{\uparrow}\rangle_1] \otimes [\alpha_2 |{\downarrow}\rangle_2 + \beta_2 |{\uparrow}\rangle_2] \tag{1.1.3}$$

$$= \gamma_1 |{\downarrow\downarrow}\rangle + \gamma_2 |{\downarrow\uparrow}\rangle + \gamma_3 |{\uparrow\downarrow}\rangle + \gamma_4 |{\uparrow\uparrow}\rangle , \tag{1.1.4}$$

where $|{\downarrow}\rangle_1 \otimes |{\downarrow}\rangle_2$ is written $|{\downarrow\downarrow}\rangle$. This more clearly shows the inherent problems of classical simulation, as the dimension of the vector space scales as 2^N of the number of qubits N. Storing the state of only 100 qubits would therefore require $2^{100} \approx 1 \times 10^{30}$ variables. The prototypical two-qubit entangled gate is the controlled-NOT (CNOT) gate, described by the operation

$$U_{CN} = |{\downarrow}\rangle \langle{\downarrow}| \otimes I + |{\uparrow}\rangle \langle{\uparrow}| \otimes \sigma_x = \begin{bmatrix} 1 & 0 & 0 & 0 \\ 0 & 1 & 0 & 0 \\ 0 & 0 & 0 & 1 \\ 0 & 0 & 1 & 0 \end{bmatrix}. \tag{1.1.5}$$

The σ_x term flips the state of the target qubit if the control is up, and the identity matrix leaves the target unaffected when the control is down. This is a unitary operation as $U^{\dagger}_{CN} U_{CN} = I$, and quantum computing, like quantum mechanics, but unlike classical computation, is therefore reversible[ii]. The MS gate engineers a spin dependent flip in the state of the target atomic qubit, and can maximally entangle atoms prepared in the basis states:

$$|{\downarrow\downarrow}\rangle \rightarrow [|{\downarrow\downarrow}\rangle + i |{\uparrow\uparrow}\rangle] / \sqrt{2}, \tag{1.1.6}$$

$$|{\downarrow\uparrow}\rangle \rightarrow [|{\downarrow\uparrow}\rangle - i |{\uparrow\downarrow}\rangle] / \sqrt{2}, \tag{1.1.7}$$

$$|{\uparrow\downarrow}\rangle \rightarrow [|{\uparrow\downarrow}\rangle - i |{\downarrow\uparrow}\rangle] / \sqrt{2}, \tag{1.1.8}$$

$$|{\uparrow\uparrow}\rangle \rightarrow [|{\uparrow\uparrow}\rangle + i |{\downarrow\downarrow}\rangle] / \sqrt{2}. \tag{1.1.9}$$

Combined with single qubit rotations the MS gate is equivalent to the CNOT gate.

A quantum circuit is built up from a series of single and two qubit gates acting on an initial register of qubits. Decoherence of superposition states is caused by any noise in these

---

[ii] In reversible computing information is not lost. As information is ulimately physical, the lost bit in a classical AND gate is converted into heat, placing a fundamental limit on the energy efficiency of irreversible machines [47, 48].

processes, or “measurement” by the environment, and is a leading factor in limiting circuit depth, the number of operations that can be run consecutively. The performance of single and multi-qubit gates is determined by randomised benchmarking [49, 50], which gives an average error rate over many operations. However decoherence processes, especially in higher order superpositions, are not extensively studied. This motivates the development of techniques to certify coherence between the motional states of a single ion using simple interference patterns, which are presented as results in this thesis.

1.2 Thesis Outline

This thesis presents developments in the Imperial ion trapping group between the last experiment in the Penning trap and the first in a new Paul trap, detailed in the publications

- P. Hrmo, M.K. Joshi, V. Jarlaud, O. Corfield, and R.C. Thompson, "Sideband cooling of the radial modes of motion of a single ion in a Penning trap", Phys. Rev. A **100**, 043414 (2019).
- O. Corfield*, J. Lishman*, C. Lee, J. Mosca Toba, G. Porter, J.M. Heinrich, S.C. Webster, F. Mintert, and R.C. Thompson, "Certifying multilevel coherence in the motional state of a trapped ion", PRX Quantum **2**, 040359 (2021).

The new project is funded by a grant to investigate "optimal control for robust ion trap quantum logic", and to develop novel methods of entanglement control. In chapter 2 the mechanisms for ion trapping introduced by Dehmelt and Paul are outlined, and the Imperial traps are described. This includes development of the new experiment, which is designed to investigate the strong coupling regime between ions. The trap requires low inherent noise, so it can be controllably introduced, and should achieve a high degree of coherence in the states of simple quantum systems. Developments in the standardisation of experimental control software and hardware mean it is possible to build state of the art experiments with increasing ease. The design is informed by the theoretical considerations presented in chapter 3.

It is a long way from the trapping of single ions to running experiments. In chapter 4 the implementation of ground state cooling is shown, after detailing the wider experimental control systems that have been developed with the project. This result, shown over 30 years ago, is a long way from probing novel physics. The undefined nature of quantum resources like entanglement and superposition mean they require metrics for quantifying the coherence in quantum states. The first demonstration of a certification procedure to determine the number of coherently superposed states is presented in chapter 5. The exacting control over the delicate motional state is a natural place to conclude the initial building phase of the experiment, and in chapter 6 we look towards future developments.

---

[*] Joint first author

Chapter 2

Ion Traps

The divergence of an electric field in free space being zero, it is impossible to generate a three dimensional minimum in a static potential. As a result ion traps typically employ one of two principal techniques for the confinement of charged particles [51]. The Penning trap uses a strong magnetic field to restrict radial motion, with a static electric field providing axial trapping. In the Paul trap a time dependent electric field can confine a charge in two or three dimensions depending on the electrode configuration. In the linear Paul trap the oscillating field provides radial confinement, with axial freedom restricted by a static field. Although the dynamic field heats the motion of ions more than the static fields of a Penning trap, several features of the magnetic field make the Paul trap, and more specifically the linear trap, more appealing for quantum simulation [52–54] and quantum information processing [55, 56]. Motion in the crossed fields of the Penning trap is fundamentally more difficult to cool, and the Zeeman effect also imposes a large splitting in the energy levels of the ions which complicates cooling processes further. Additionally it is difficult, and expensive, to generate a large magnetic field; however this will become less of a problem in micro-fabricated traps with embedded magnetic field coils close to the ion [57]. If the inherent complexities of the Penning trap can be overcome it may be more favourable for scaling to larger numbers of ions in quantum simulation and information processing due to the fundamental noise driven by the oscillating field of the Paul trap.

The Penning trap is discussed in section 2.1, which provides an overview of the Imperial trap. Following this section 2.2 describes the Paul trap, including the design and realisation of a linear trap.

2.1 The Penning Trap

In the Penning arrangement described by Dehmelt [9], a uniform magnetic field $\mathbf{B}$, with amplitude B_0, is combined with an electric field $\mathbf{E}$, defined by the static potential Φ. These are given in cylindrical coordinates, where $\rho = \sqrt{x^2 + y^2}$, by

$$\Phi(\rho, z) = A_0(2z^2 - \rho^2), \qquad \text{and} \qquad \mathbf{B} = B_0\hat{\boldsymbol{z}}. \tag{2.1.1}$$

The electric field produces a harmonic potential well along the magnetic field axis $\hat{\boldsymbol{z}}$, with radial symmetry. Such a field can be generated by applying a potential difference between electrodes which follow the equipotential surfaces of Φ[i]. The amplitude of the electric potential is given by

$$A_0 = \frac{\alpha U}{\rho_0^2 + 2z_0^2} = \frac{\alpha U}{R_0^2}, \tag{2.1.2}$$

and is proportional to the voltage U applied between axial endcap and ring electrodes as indicated in fig. 2.1.2. This also defines the dimensional constants z_0 and ρ_0, which are combined to give a trap dimension R_0 defining the electric potential of eq. (2.1.1). The potential is further scaled by a geometric constant, defined for hyperbolic electrodes as $\alpha = 1$, and reduced from unity for different electrode configurations. This is discussed in more detail in section 2.1.2.

2.1.1 Motion

The equations of motion describing a single charged particle in the fields defined in eq. (2.1.1) are derived in refs [51, 58],

$$\begin{bmatrix} \ddot{\rho} \\ \ddot{z} \end{bmatrix} = \omega_z^2 \begin{bmatrix} \frac{1}{2}\rho \\ -z \end{bmatrix} + \omega_c \begin{bmatrix} \dot{\rho} \\ 0 \end{bmatrix}. \tag{2.1.3}$$

The axial z motion, which is unaffected by the magnetic field, undergoes harmonic oscillation at frequency $\omega_z = \sqrt{4qA_0/M}$. In the absence of an electric field, the cyclotron frequency $\omega_c = qB_0/M$ describes the frequency of a circular motion defined by the field magnitude B_0 and the charge to mass ratio of the particle q/M. However the electric field

---

[i] The surfaces of equal potential are hyperboloids of revolution, generated by rotating hyperbolic functions $\rho^2/\rho_0^2 - z^2/z_0^2 = \pm 1$, where $\rho_0 = \sqrt{2}z_0$, about the z axis.

in the radial plane $\Phi(\rho, 0)$ forms a potential hill, and so the direction of $\mathbf{E}$ is always away from the trap centre. The resultant $\mathbf{E} \times \mathbf{B}$ drift leads to an orbital motion around the trap axis, in the same direction as the cyclotron motion, termed the magnetron motion. The potential hill also acts to reduce the centrifugal force experienced by the ion, modifying the cyclotron frequency.

Motion in the radial plane is a superposition of the magnetron and modified cyclotron modes of oscillation, resulting in the epicyclic orbit shown in fig. 2.1.1. Solutions to the equations of motion in eq. (2.1.3) determine particle trajectories, defined in terms of axial, modified cyclotron, and magnetron amplitudes $r_{z,+,-}$ and initial phases $\theta_{z,+,-}$:

$$\begin{aligned} x(t) &= r_- \cos(\omega_- t + \theta_-) + r_+ \cos(\omega_+ t + \theta_+), \\ y(t) &= -r_- \sin(\omega_- t + \theta_-) - r_+ \sin(\omega_+ t + \theta_+), \\ z(t) &= r_z \cos(\omega_z t + \theta_z). \end{aligned} \tag{2.1.4}$$

The two radial frequencies are given by

$$\omega_\pm = \frac{1}{2}\left(\omega_c \pm \sqrt{\omega_c^2 - 2\omega_z^2}\right) = \frac{1}{2}\omega_c \pm \omega_1. \tag{2.1.5}$$

The condition for stable solutions to eq. (2.1.5), for real radial frequencies, limits the axial frequency for a given cyclotron frequency. This defines the maximum voltage that can be applied to the electrodes before the trap becomes unstable,

$$\omega_z^2 < \frac{1}{2}\omega_c^2, \qquad\qquad A_0 < \frac{qB_0^2}{8M}. \tag{2.1.6}$$

As the true cyclotron frequency is dependent on fundamental properties of the particle, precise measurement of this value is used for mass spectrometry. However the result of summing the measured values of the modified cyclotron ω_+ and magnetron ω_- frequencies, $\omega_c = \omega_+ + \omega_-$, is sensitive to any imperfection in the fields. The invariance theorem defined by $\omega_c^2 = \omega_+^2 + \omega_-^2 + \omega_z^2$ [58], does give an accurate measure of the true cyclotron frequency where higher order quadratic terms in the electric field, or misalignment with the magnetic field, are present, and greatly increases the accuracy of Penning traps as mass spectrometers.

Rotating Frame

In a frame of reference rotating at frequency $\omega_c/2$, the radial equations of motion are decoupled; following eq. (2.1.5), the two modes describe positive and negative circular motion about the origin at frequency ω_1 [59]. In this frame the radial motion is described by two-dimensional simple harmonic oscillation, induced by an effective potential proportional to $\omega_1^2 = \omega_c^2/4 - \omega_z^2/2$. This highlights the contribution of the magnetic field in providing radial confinement, whilst the axial field is deconfining.

Energy

The sum of the kinetic and potential energy of a particle is constant, and can be written in terms of the energy in each mode [60] as

$$E = \frac{1}{2}M\left[r_z^2\omega_z^2 + 2r_+^2\omega_+\omega_1 - 2r_-^2\omega_-\omega_1\right]. \tag{2.1.7}$$

Energy in the magnetron mode contributes negatively to the total, as its kinetic energy is less than the negative potential energy in the radial plane, which forces the particle away from the trap centre, $\nabla\Phi(\rho, 0) = -2A_0\rho$. Consequently the mode is unstable; if the ion loses kinetic energy through a dissipative process, it rolls down the potential hill, until lost from the trap. To reduce the magnetron amplitude energy must be added, equivalent to pushing the ion up the potential hill. However as the modified cyclotron mode is cooled by removing energy, the cooling process is greatly complicated.

Axialisation Field

The axialisation technique [61] uses an oscillating quadrupole potential to couple the radial modes. This is of the form

$$\phi_a = \frac{V_a}{2\rho_0^2}\left[x^2 - y^2\right]\sin(\omega_c t), \tag{2.1.8}$$

where V_a is the amplitude of the rf field applied at the true cyclotron frequency ω_c. This couples the radial modes, leading to a coherent exchange of energy between the modified cyclotron and magnetron motion, shown in fig. 2.1.1. As the averaged amplitudes of the modes are equalised, damping the motion of one mode can therefore remove kinetic energy from both.

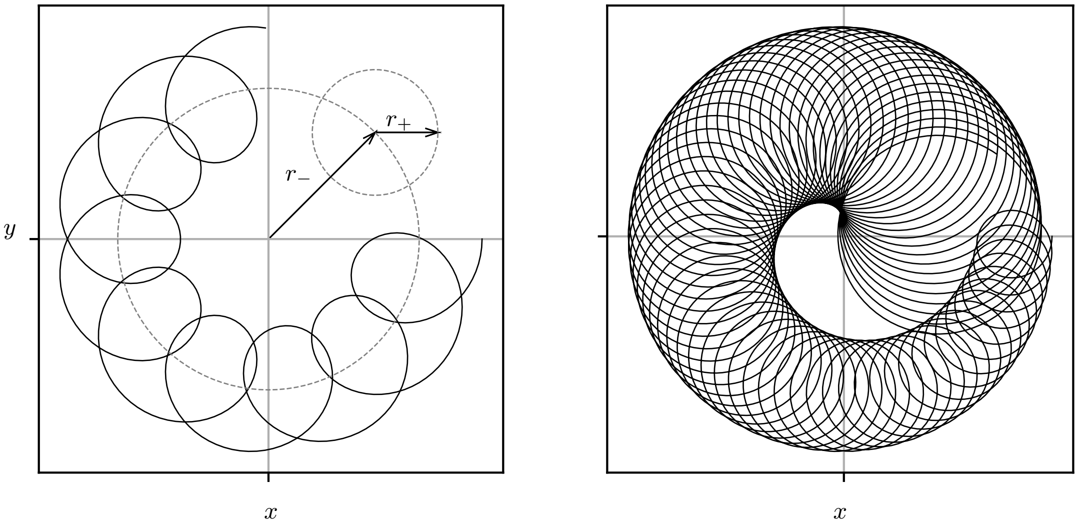

Figure 2.1.1: (Left) epicyclic radial motion in a Penning trap. The radial extent of the motion is bound by mode amplidudes ($|r_- - r_+|$ and $r_- + r_+$). (Right) with the addition of the axialisation field of eq. (2.1.8) the radial modes are coupled causing sinusoidal oscillation between amplitudes r_+ and r_-. [scale arbitrary for illustration]

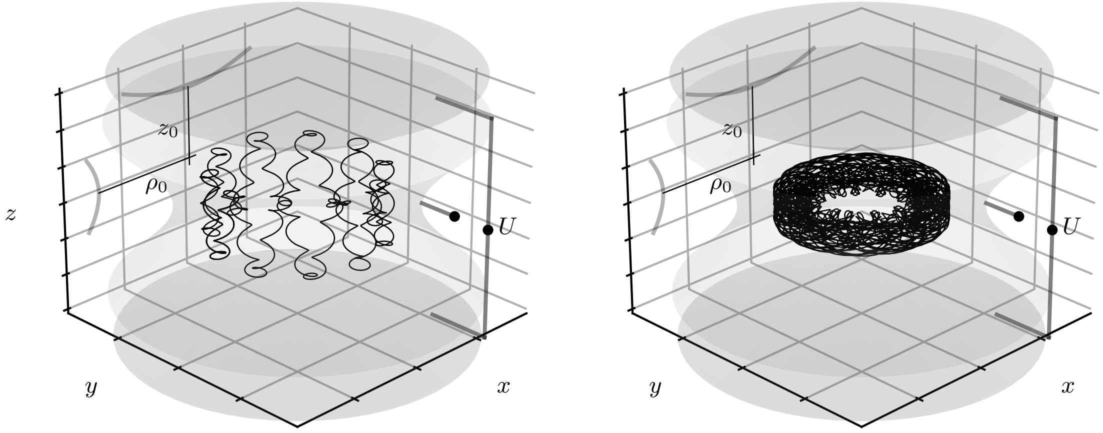

Figure 2.1.2: Example trajectories of a single ion following eq. (2.1.4). Ions are initially captured in large orbits and cooled to the trap centre. Ideal hyberbolic electrodes are shown, with trap voltage U applied between the endcaps (darker) and ring electrode (lighter). [scale arbitrary for illustration]

2.1.2 Imperial Penning Trap

The current Penning trap at Imperial College was established in 2011 in collaboration with the HITRAP facility at GSI, Darmstadt [62], and is shown in fig. 2.1.3. This is known as the SpecTrap, and was designed to perform fundamental tests of QED using highly charged ions [63]. By stripping all but one electron from heavy atoms, high resolution spectroscopy can be performed on the simple hydrogen-like energy level structure. To this end, the trap consists of stacked cylindrical electrodes which facilitate the capture of externally generated highly charged ions. The Imperial branch of the collaboration originally investigated the radial compression of ion plasma clouds using a 'rotating wall' technique, as higher cloud densities increase the measurable signal [64]. This is a similar technique to axialisation, which enhances radial laser cooling in single ions and small clouds [61]. The rotating wall and axialisation fields are applied to the separate segments of the ring electrode, shown in fig. 2.1.3, which allows the generation of dipole and quadrupole fields at the ion.

Inter-ion Coulomb repulsion becomes significant as energy is removed from the motion in small clouds via laser cooling. This leads to the formation of ion Coulomb crystals (ICCs), whose configuration depends on trapping and laser cooling parameters [65]. For small numbers of ions, Doppler cooling enables resolution of optical sidebands on the narrow linewidth quadrupole transition, and the determination of mode energies [66][ii]. Optical sideband cooling to the zero-point energy was first shown in a Paul trap in 1995 [15], establishing their dominance in quantum information processing with trapped ions. Sideband cooling to the ground state of the axial motion in a single ion was shown in the Imperial Penning trap in 2016 [16][iii]. These techniques were extended to ground state cooling of axial modes in two-ion crystals [69], as well as small numbers of ions in planar crystals [70]. Multi-mode sideband cooling was applied to the radial motion in 2019 [17][iv], showing that it is possible to cool the motion of a single ion in a Penning trap to the ground state in all dimensions.

[ii] Development of the apparatus from [62] detailed in ref [67].

[iii] With further detail of the extended apparatus in ref [68].

[iv] Detail of extended trapping apparatus not given here can be found in ref [71].

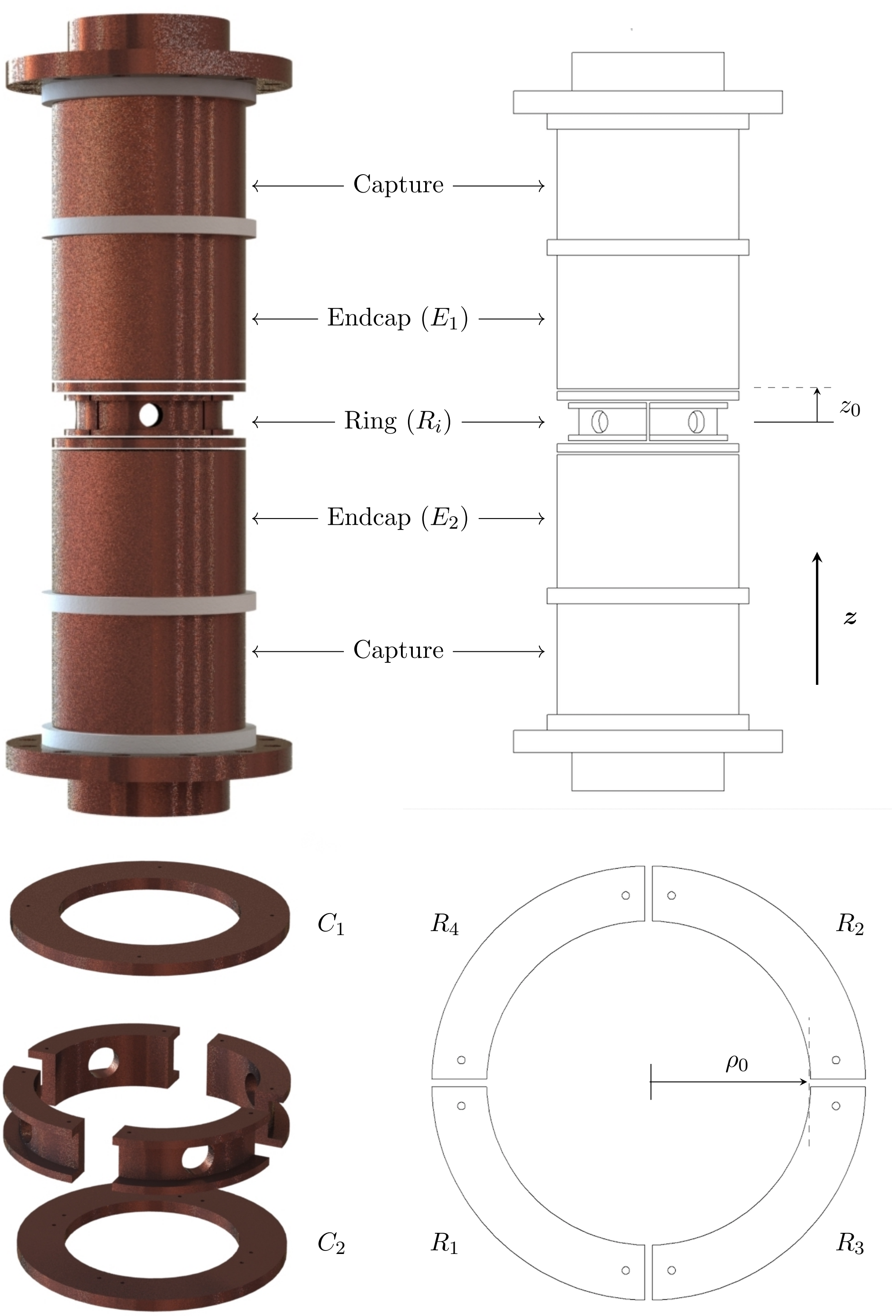

Figure 2.1.3: The stacked cylindrical electrodes of the Imperial SpecTrap are separated by ceramic rings and held together with rods. This design allows for good optical access, and is easily fabricated. The trap dimensions are $z_0 = 5.65\,\text{mm}$ and $\rho_0 = 10.6\,\text{mm}$, and with compensation electrodes $C_{1,2}$ the anharmonic terms expected for non-hyperbolic electrodes can be minimised. The voltage U is applied to endcaps $E_{1,2}$ with ring segments connected to ground. Corrective fields applied to axial compensation $C_{1,2}$ and radial ring R_{1-4} electrodes are derived from a potential difference $V_z = |V_{C1} - V_{C2}|$; and, as the radial compensation field is symmetrical, between ring segments, e.g. $V_r = |V_{R3} - V_{R4}|$. The split ring electrode also enables application of rf fields. Holes in the ring segments with $\varnothing 4\,\text{mm}$ provide access for laser beams and imaging of the ion. The capture electrodes were designed to slow externally generated highly charged ions.

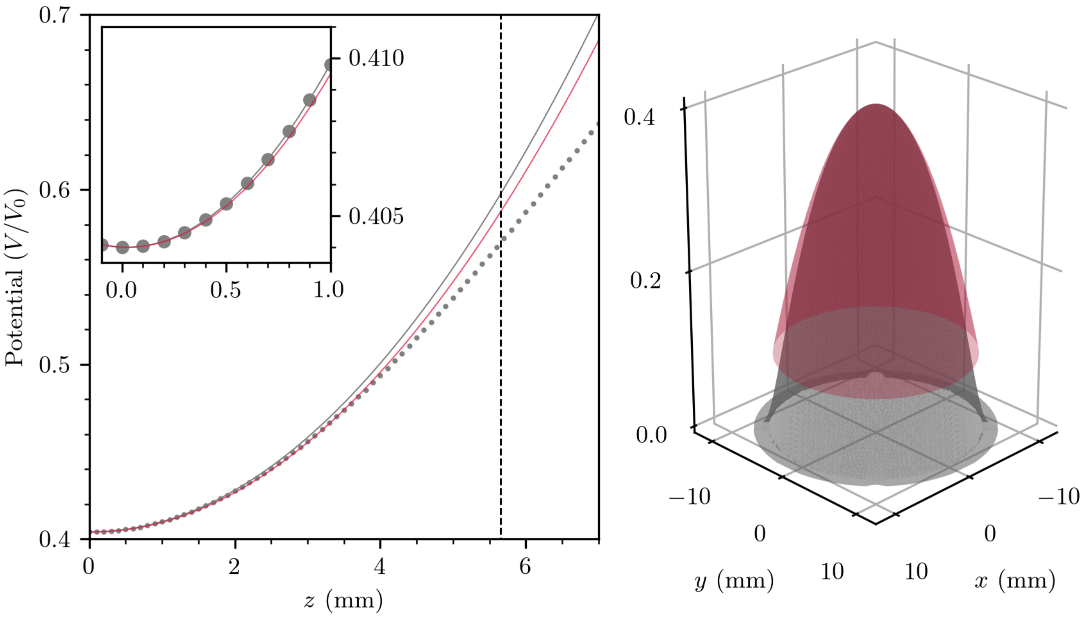

Figure 2.1.4: Electric potential in the Imperial SpecTrap with $U = 1\,\mathrm{V}$ applied to endcaps and all other electrodes grounded. (Left) simulation of the axial potential, $\Phi(0, z)$, is shown (points), with the fit (grey) to the ideal field defined in eq. (2.1.1) giving $\bar{\alpha} = 0.54$. The effective potential (red) is projected from direct measurement of the trap frequency, which implies $\alpha = 0.52$. The dashed line shows the extent of the cylindrical endcap. (Right) simulation of the radial potential (grey), $\Phi(\rho, 0)$. Electrodes have radial symmetry, shown by the fit (red), and therefore produce the field of eq. (2.1.1). [Fits performed in $1\,\mathrm{mm}^3$ volume].

Electric Field

The field produced by non-hyperbolic cylindrical electrodes can be estimated from simulation, which is discussed further in section 2.2.2. In fig. 2.1.4 the potential is shown in the axial and radial directions. This can be compared to measurement of the trap frequency as a function of voltage, from which the geometric term α can be inferred. Using the effective trap dimensions ρ_0 and z_0 defined in fig. 2.1.3, the geometric constant is determined from simulation $\bar{\alpha} = 0.54$, and direct measurement of the trap frequency $\alpha = 0.52$. Whilst the shape of the electrodes causes a reduction in the field amplitude A_0 for an applied voltage, the potential is harmonic around the trap centre, and is therefore well described by eq. (2.1.1).

Magnetic Field

The magnetic field is provided by a superconducting magnet which is cooled by liquid helium to 4.2 K. This generates a uniform magnetic field in a small region at the center of the solenoid, where the trap is positioned. Patch potentials, variations in the electrostatic potential across the electrode surface, can shift over time, and the compensation fields enable precise alignment of the electric and magnetic fields.

2.2 The Linear Paul Trap

In a linear Paul trap, charged particles are confined radially by a two-dimensional oscillating quadrupole field [72]. This is produced by applying an rf voltage $V(t) = V_0 \cos(\Omega t)$, with amplitude V_0 and frequency Ω, to the hyperbolic electrodes shown in fig. 2.2.1 (a). The potential is scaled by the trap dimension r_0, the distance between electrodes and the trap axis, and a geometric constant κ_r, which is reduced from its ideal value of unity by non-hyperbolic electrodes. The potential

$$\Phi(x, y, t) = \frac{\kappa_r V(t)}{2r_0^2} \left[x^2 - y^2\right] \tag{2.2.1}$$

is shown in fig. 2.2.1 (b), and oscillates between confining in x and deconfining in y at $t = 0$, and vice versa after half a period at $t = \pi/\Omega$. Under certain conditions the time averaged effect is a finite ponderomotive force which drives charged particles to the region of weaker field. The red ball demonstrates how a net confining force can be produced if, on average, the particle spends more time displaced in x when the field is strongly confining in x, and near the x origin when the field is deconfining in x. The conditions for radial confinement are discussed in section 2.2.1.

Axial confinement is produced by a static harmonic potential, approximated at the trap centre by

$$\Psi(x, y, z) = \frac{\kappa_z U_0}{2z_0^2} \left[2z^2 - x^2 - y^2\right] . \tag{2.2.2}$$

This is produced by endcap electrodes on the trap axis at $\pm z_0$. As these electrodes cannot follow equipotential surfaces of eq. (2.2.2), axial confinement is weaker for the applied voltage U_0 than would be the case for ideal electrodes. This is accounted for by the constant κ_z. Geometric constants for the Imperial trap are determined in section 2.2.2.

If the quadrupole potential is generated by applying $\pm V(t)/2$ to opposite electrode pairs, the potential along the z axis remains at the ac ground. However in this driving configuration a differential phase delay at each electrode can shift the location of the field minima over the rf period. To avoid this, $V(t)$ is applied to one pair of electrodes, with the other pair held at ac ground. However as a result the absolute potential along the trap axis oscillates between $\pm\kappa_r V_0/2$ at the drive frequency, adding a term $\kappa_r V_0 \cos(\Omega t)/2$

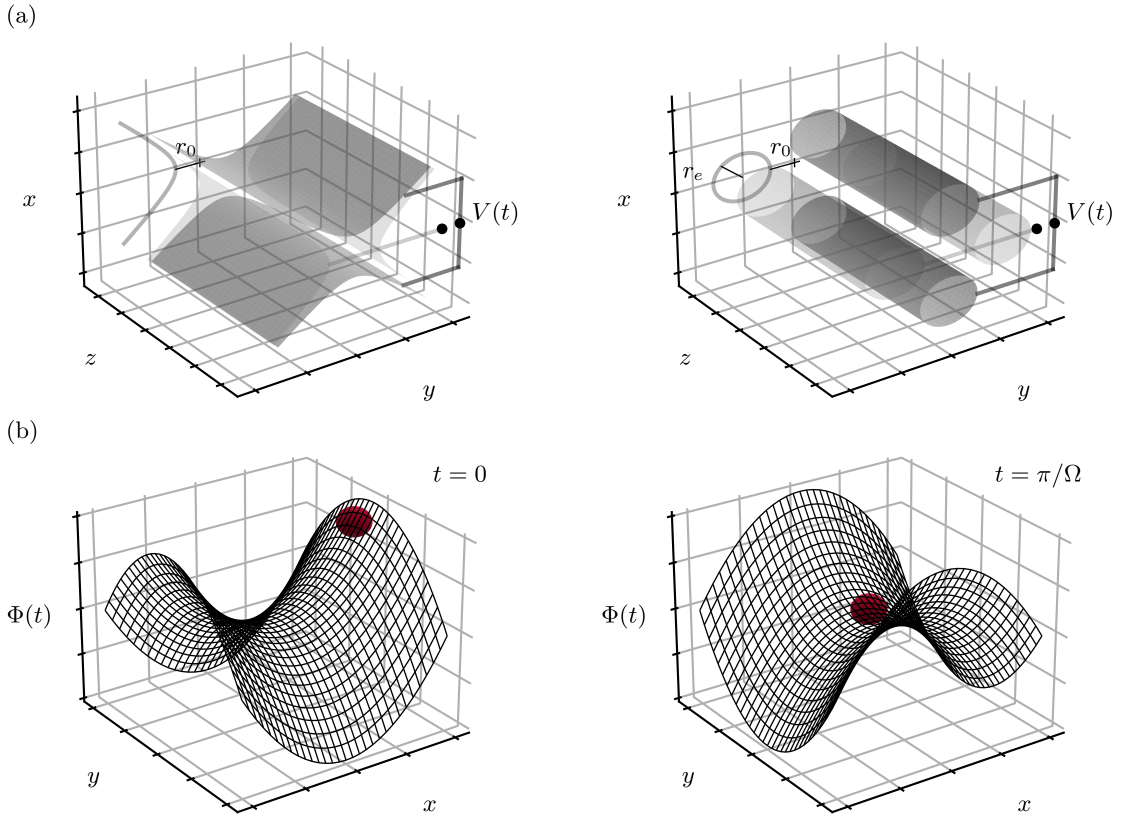

Figure 2.2.1: (a) On the left ideal hyperbolic electrodes are shown, which follow the equipotential surfaces of $\Phi(x, y)$ and are infinite in length (z). Finite length rods were used in the original linear Paul traps, shown right, which produce an approximation of the quadrupole field at the trap centre, optimised for the ratio $r_e/r_0 = 1.15$ [73]. The potential difference $V(t)$ is applied between opposite pairs of electrodes, and the dimension r_0 is defined as half the minimum distance between these pairs. (b) The radial potential $\Phi(x, y, t)$ oscillates between confining in x at $t = 0$ and in y after half a period in the rf frequency Ω.

to the radial potential Φ. This would not affect the motion of the ion if not for the fixed voltage at the endcaps, which leads to an oscillating harmonic potential along the z-axis. The result is a three-dimensional trapping potential which is weakly confining in z. The linear trap in this configuration acts like the classic three-dimensional Paul trap, where the voltage $V(t)$ is applied to electrodes of fig. 2.1.2 in place of U. However in the linear trap the rf contribution to the axial frequency is negligible, as $\kappa_z/z_0^2 \ll \kappa_r/r_0^2$, and the axial motion is consequently dominated by the effect of the dc potential.

2.2.1 Motion

The electric field in the trap is defined by the rf and dc potentials,

$$\boldsymbol{E}(x, y, z, t) = -\left[\nabla\Phi(x, y, t) + \nabla\Psi(x, y, z)\right]. \tag{2.2.3}$$

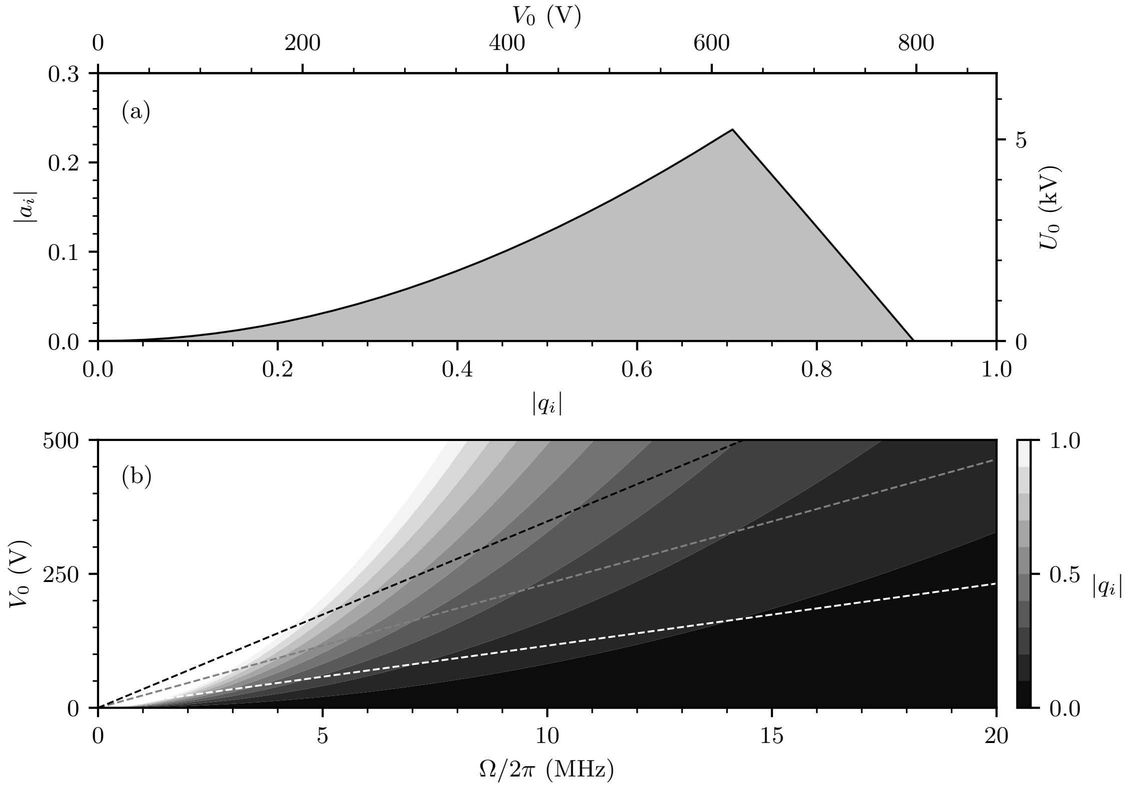

Figure 2.2.2: (a) first Mathieu a–q stability region, symmetric about the a and q axes. (b) q_i parameter as a function of the rf voltage $V(V_0, \Omega) = V_0 \cos(\Omega t)$. The dashed lines show the trap frequency $\omega_i/2\pi = 500\,\mathrm{kHz}$ (white), 1 MHz (grey), and 1.5 MHz (black). The converted scales and contour plot are valid for the Imperial trap parameters: $\Omega/2\pi = 10.3\,\mathrm{MHz}$; dimensions in fig. 2.2.4; geometric scaling in fig. 2.2.5.

The equations of motion for a particle, parameterised by its charge to mass ratio q/M, are then

$$\begin{aligned}\ddot{x} + \left[\frac{-q\kappa_z U_0}{M z_0^2} + \frac{q\kappa_r V_0}{M r_0^2}\cos(\Omega t)\right] x &= 0\\ \ddot{y} + \left[\frac{-q\kappa_z U_0}{M z_0^2} + \frac{-q\kappa_r V_0}{M r_0^2}\cos(\Omega t)\right] y &= 0\\ \ddot{z} + \frac{2q\kappa_z U_0}{M z_0^2} z &= 0.\end{aligned} \tag{2.2.4}$$

The axial motion is described by simple harmonic oscillation at frequency

$$\omega_z = \sqrt{\frac{2q\kappa_z U_0}{M z_0^2}}. \tag{2.2.5}$$

The radial equations are of the Mathieu form,

$$\ddot{u}_i + \left[a_i + 2q_i \cos(\Omega t)\right] \frac{\Omega^2}{4} u_i = 0, \tag{2.2.6}$$

where $i = x, y$, and $\mathbf{u} = u_x\hat{x} + u_y\hat{y}$ is the radial position, defined by the coordinate system in fig. 2.2.1 (a). The radial terms in eq. (2.2.4) are equivalent to eq. (2.2.6) with the substitutions

$$a_x = a_y = -\frac{4q\kappa_z U_0}{Mz_0^2\Omega^2} \qquad \text{and} \qquad q_x = -q_y = \frac{2q\kappa_r V_0}{Mr_0^2\Omega^2}. \tag{2.2.7}$$

Whether a trajectory described by eq. (2.2.6) is stable, will not hit the electrodes at r_0, depends only on the parameters a_i and q_i, and not initial conditions. The first region of a–q stability for both radial modes is shown in fig. 2.2.2 (a), where low absolute values of a_i and q_i are required for stable trajectories. Therefore stability is increased by maximising the drive frequency Ω and minimising the rf field amplitude V_0, shown by the scaling of the q_i parameter as a function of the applied rf voltage in fig. 2.2.2 (b).

Radial confinement of stable trajectories is a result of the induced ponderomotive potential. The ponderomotive force $F_p \propto q^2E^2$ is exhibited as the velocity of a particle in a rapidly oscillating inhomogeneous field is not constant. If the stability parameter $|q_i| < 0.4$, this produces an effective harmonic potential [74, 75] given by

$$\Phi_p = \frac{q^2}{4M\Omega^2}\langle \boldsymbol{E}^2 \rangle. \tag{2.2.8}$$

Combining this with the deconfining axial field [76] gives

$$\Phi^*(x, y) = \left[\frac{q^2\kappa_r^2V_0^2}{4M\Omega^2r_0^4} - \frac{\kappa_z U_0}{2z_0^2}\right]\left[x^2 + y^2\right], \tag{2.2.9}$$

which can be written

$$\Phi^*(x, y) = \frac{1}{2}M\left[\omega_x^2x^2 + \omega_y^2y^2\right], \qquad \text{with} \qquad \omega_i = \frac{1}{2}\Omega\sqrt{a_i + \frac{1}{2}q_i^2}. \tag{2.2.10}$$

The radial trap frequencies therefore depend on the amplitude and frequency of the applied voltage $V(t)$. In fig. 2.2.2 (b) it is evident that increasing the drive frequency enables higher trap frequencies without breaking the effective potential approximation.

Under the effective potential approximation the solutions to eq. (2.2.6) are be described by a small amplitude oscillation at the drive frequency, termed micromotion, superimposed

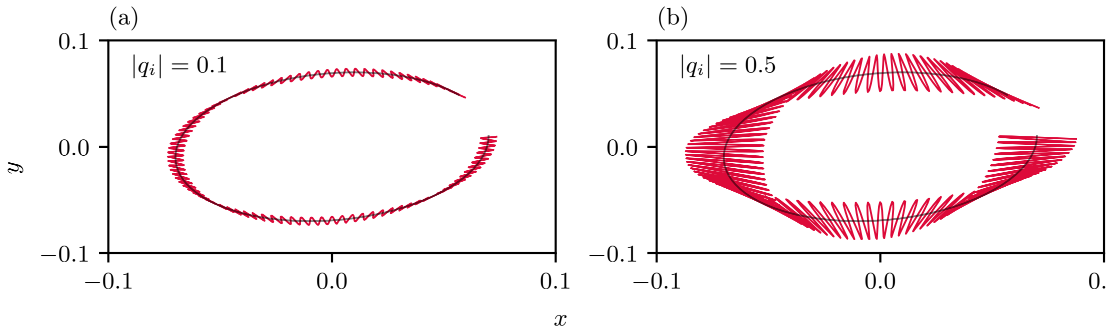

Figure 2.2.3: The radial trajectory of an ion following eq. (2.2.13) for different values of the stability parameter q_i (red). The secular harmonic motion, without micromotion, is also shown (grey).

onto a slow varying harmonic secular motion,

$$u_i(t) = [u_{1i} \cos(\omega_i t + \phi_i)] \left[1 + \frac{q_i}{2} \cos(\Omega t)\right], \tag{2.2.11}$$

for $i = x, y$ and secular motion amplitude u_{1i}. Examples trajectories and are plotted in fig. 2.2.3 (a) and (b), showing the motion in and outside the adiabatic regime.

Excess Micromotion

Misalignment of the rf and dc fields can be modelled by the addition of a uniform static field E_d, which modifies the equations of motion [77],

$$\ddot{u}_i + [a_i + 2q_i \cos(\Omega t)] \frac{\Omega^2}{4} u_i = \frac{q E_d u_{0i}}{M}. \tag{2.2.12}$$

The trajectory of a single ion is then

$$u_i(t) = [u_{0i} + u_{1i} \cos(\omega_i t + \phi_i)][1 + \frac{q_i}{2} \cos(\Omega t)]. \tag{2.2.13}$$

The additional terms, when compared with eq. (2.2.11), are called excess micromotion. If the ion is displaced from the centre of the rf field by an amount u_{0i}, it will oscillate with amplitude $\frac{1}{2} u_{0i} q_i$, even when the amplitude of the secular motion $u_{1i} = 0$.

Since there is also a time dependent potential along the z-axis, the axial micromotion can be determined by defining a q_z parameter,

$$q_z = \frac{2q\kappa_z V_0}{M z_0^2 \Omega^2}. \tag{2.2.14}$$

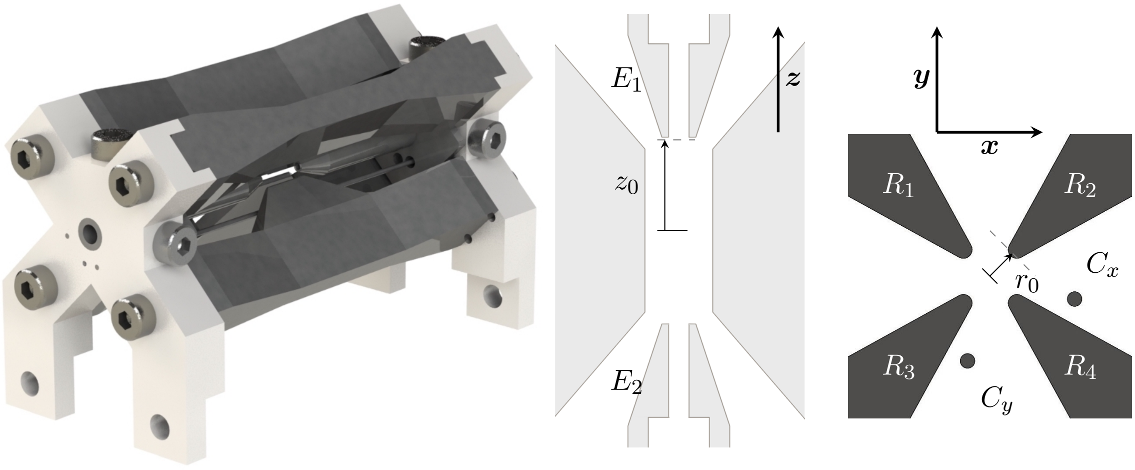

Figure 2.2.4: (Left) render of the Imperial linear Paul trap showing mounted electrodes. (Middle) a cross section through one pair of radial electrodes defines the axial dimension $z_0 = 2.75\,\mathrm{mm}$. (Right) cross section of the radial plane, showing the axes of the lab frame, used for imaging and compensation. $r_0 = 1\,\mathrm{mm}$. Technical drawings of the trap assembly and electrodes are shown in appendix B.

2.2.2 Imperial Paul Trap

A design that has been adopted in a large number of quantum information experiments is the Innsbruck linear blade trap. Developed in the early 2000s, it is named for the radial electrodes which enable a small characteristic dimension r_0, which facilitates the generation of higher radial trapping frequencies, whilst maximising optical access for imaging the ions. The large ion–electrode distance means low heating rates are observed in linear traps [78] when compared with surface traps, where the ion electrode distance is far smaller. The Imperial version of this design is shown in fig. 2.2.4. The electrodes are polished to reduce surface defects and mounted in ceramic (MACOR) supports for accurate alignment.

The final electrode geometry is informed by simulation of trapping fields, discussed in the following section, which enables the determination of the constants κ_r and κ_z. These are used to calculate the expected stability range of the trap and to model compensation of the dc field. Field compensation is possible with voltages applied to $C_{x,y}$, and as a voltage differential between endcaps $E_{1,2}$.

In the remainder of this section, the vacuum system is detailed, as well as a summary of the bakeout procedures used to obtain vacuum. Finally the magnetic fields and trap voltage supplies are discussed.

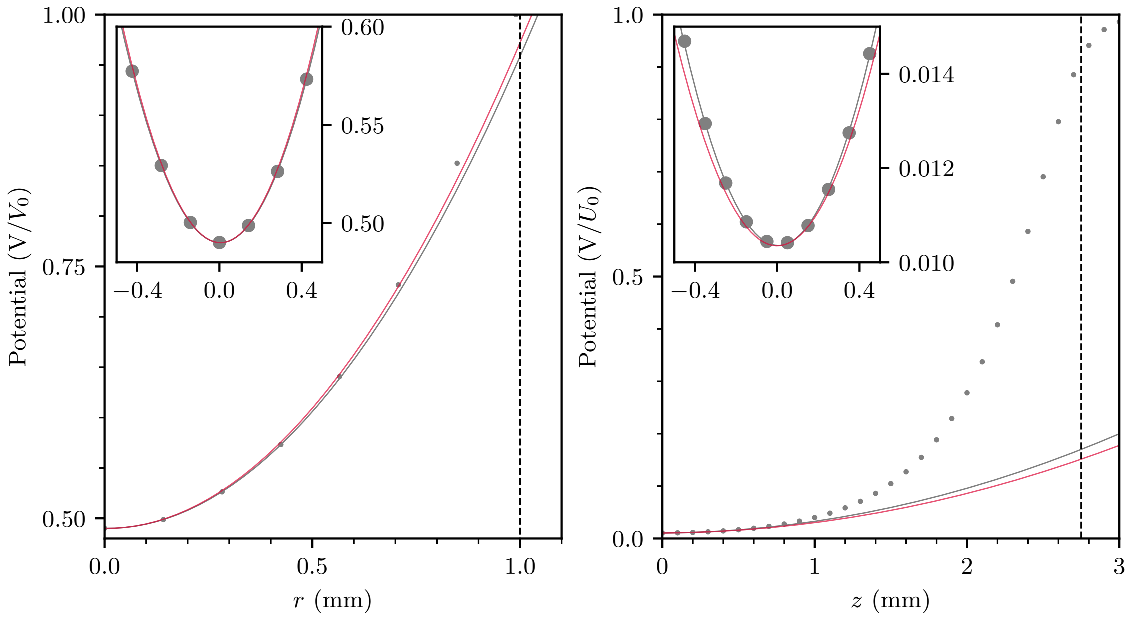

Figure 2.2.5: (Left) simulation of the potential along the x axis at $t = 0$, with $V = V_0$ applied to electrodes $R_{2,3}$ and electrodes $R_{1,4}$ at $V = 0$ (points). The quardratic fit (grey) gives $\bar{\kappa}_x = 0.95$. (Right) potential along the z axis with endcap voltage U_0 applied to endcaps $E_{1,2}$ (points). A quadratic fit to the simulation around the trap centre (grey) enables determination of $\bar{\kappa}_z = 0.155$. The red lines show the implied potential from measurement of the trap frequencies. [Fitting performed in $1\,\mathrm{mm}^3$ volume.]

Electric Fields

The expected trap fields for the electrode geometry shown in fig. 2.2.4 are estimated using the simulation package SIMION[v]. A result of the linearity of Maxwell's equations is that the total potential at any point in free space is the sum of the potential induced by each electrode independently. From a database of the potentials induced by each electrode it is then possible to determine the total potential in the trap for any combination of applied static voltages. In fig. 2.2.5 values of the potential along the x axis are shown for a voltage applied to the radial driving electrodes, and along the z axis with a voltage on the axial endcaps. Geometric factors are extracted from a quadratic fit to the potentials, giving $\bar{\kappa_z} = 0.155$ and $\bar{\kappa}_x = 0.95$, and are used to approximate the trap stability parameters in fig. 2.2.2. Independent measurement of the axial and radial trap frequencies in section 4.3.2 implies the geometric factors are $\kappa_z = 0.132$, and $\kappa_x = 0.97$, shown by the red lines in fig. 2.2.5.

From the simulation it is also possible to estimate the expected field produced by applying compensation voltages to the electrodes C_x and C_y shown in fig. 2.2.4. These enable alignment of the static dc field defined in eq. (2.2.2), such that the centre of the field is

---

[v] Further information can be found at simion.com.

j	Direction	Compensation Field ($\mathrm{V\,m^{-1}}$)		Ion displacement (μm)	
		measured	simulated	measured	simulated
x	horizontal	4.6	8.07	-11.1	-19.5
y	vertical	-	-8.61	-	20.8
z	axial	11.0	10.9	-26.5	-26.3

Table 2.2.1: Simulated compensation field per V_j, and resultant ion displacement near the trap centre at $\omega_j = 1\,\mathrm{MHz}$. Compensation is performed in the lab frame, with voltages V_j applied to compensation electrodes: V_x to C_x, V_y to C_y, $V_z = |V_{E1} - V_{E2}|$. It is not possible to measure vertical displacement of the ion with the imaging camera.

aligned with the null of the rf field. As there is also an oscillating potential along the trap z axis, a voltage differential between the endcaps allows for full three-dimensional alignment of the rf null and the centre of the dc field. The simulated fields produced by compensation electrodes per V_j are given in table 2.2.1. This simulation enables an estimation (shown in grey 'simulated' column) of the expected ion displacement at a trap frequency of 1 MHz. This can be compared with the measured translation of the ion per V_j at a trap frequency of 1 MHz, from which the actual compensation fields can be inferred (shown in grey 'measured' column). The radial offset per volt applied is significantly less than expected, most likely due to the fact that thinner diameter wire was used for the electrodes than modelled.

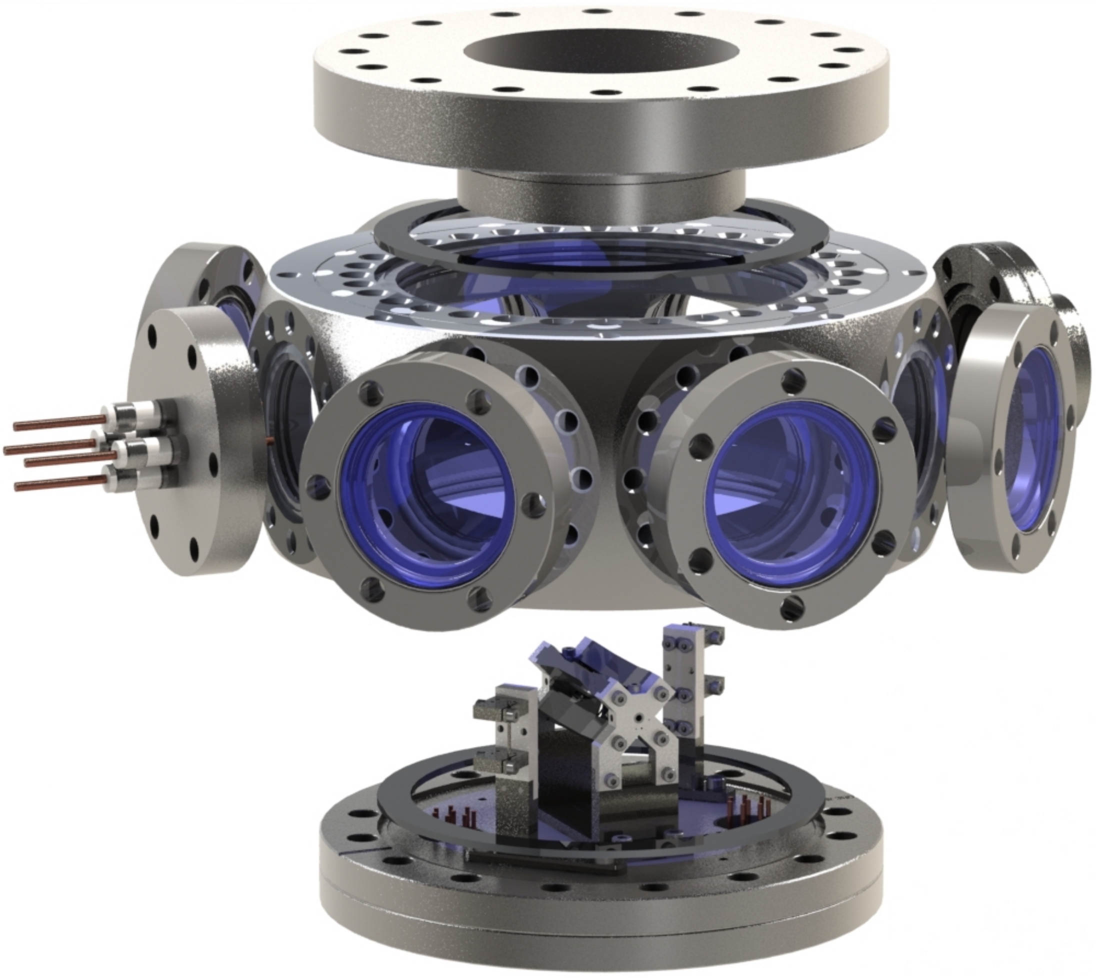

Figure 2.2.6: Paul trap vacuum system. All parts are detailed in appendix A. Silver plated gaskets are used as copper can degrade under vacuum, and the screws (not shown) are also plated to reduce the risk of seizing. The chamber and trap are made from non-magnetic 316L stainless steel. The modified base flange, recessed viewport, and feedthrough connections are detailed in the drawings in appendix B.

Vacuum System

Collision with background gas molecules will destroy any prepared state in the ions' motion. The collision rate is proportional to the pressure in the system, which can be reduced from atmosphere ($\approx 1 \times 10^5\,\mathrm{Pa}$) to the ultra high vacuum (UHV) regime, below $1 \times 10^{-7}\,\mathrm{Pa}$. Very roughly this reduces the collision rate from the order of a billion collisions per second to one every couple of hours. A collision does not typically result in the loss of the ion, at a trap frequency of 1 MHz the trap depth $D = {}^1\!/\!{}_2 M\omega_r^2 r_0^2 \approx 10$ eV, and once sufficiently infrequent, collisions can be accounted for in experimental control.

The vacuum system is assembled from commercially available components, and is shown in fig. 2.2.6 with the mounted trap and atomic ovens. These are attached to the base flange, which contains the dc feedthroughs. The trap rf is applied through a 4 pin feedthrough,

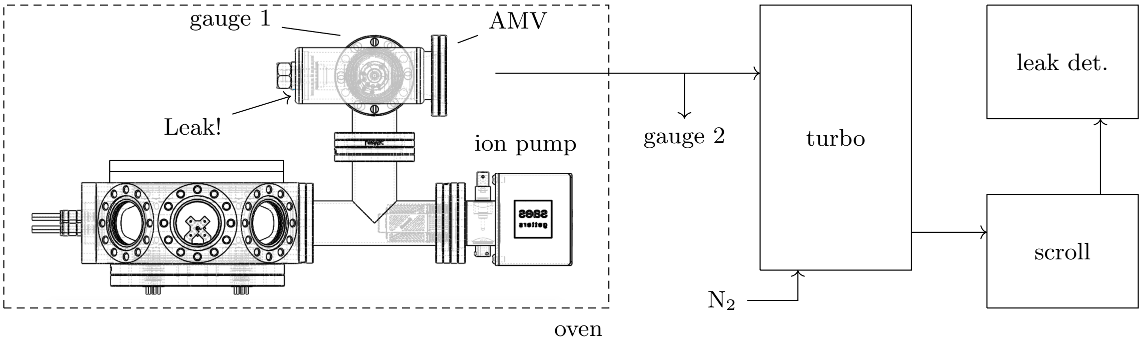

Figure 2.2.7: Schematic of the pumping station. The chamber is conneceted through the AMV to a set of bellows that pass through the oven wall. The pressure can be monitored outside the oven at gauge 2. The scroll pump and leak detector are connected in series after this. When raising the pressure to open the system the turbo is vented with nitrogen gas.

connected on the opposite side of the chamber to the pumps, gauge 1, and the all-metal valve (AMV). The top recessed viewport allows for highly efficient imaging of the ions.

A vacuum pump is better thought of as a one way valve, where particles can only leave the system. An ion pump operates by ionising gas molecules and accelerating them into a getter material where they are trapped. This pump can maintain a pressure below 1×10^{-9} Pa, however cannot reduce the pressure from atmosphere. A scroll pump is used to reduce the pressure in the system quickly, with a pumping speed on the order of $10\,\mathrm{m^3\,h^{-1}}$, however is limited to around 1 Pa. A turbo pump is therefore used to reduce the pressure to the UHV regime, with the pump arrangement shown in fig. 2.2.7.

The ultimate pressure in the chamber is limited by leakage, through gaskets or virtually via out-gassing of internal surfaces. The CF flanges can maintain pressures below 1×10^{-11} Pa, and the AMV at 1×10^{-10} Pa. Out-gassing occurs in components when molecules, mainly hydrogen and water vapour, effectively leak over time from impurities in the structure. Organic matter can be a catastrophic cause of out-gassing, making sterile assembly of internal components essential. All vacuum facing components are therefore cleaned at 35 °C in an ultrasonic bath for 20 minutes with:

- Detergent - to remove the majority of grease from manufacturing and handling.
- Acetone/Ethanol - to remove oils and organic material from stainless steel/ceramic.
- Distilled water - to clean any residue.

Items were handled with gloves during this process, and parts wrapped after drying.

Bakeout

The out-gassing rate of a material is increased with higher temperature. The chamber is therefore baked in an oven whilst pumping through a turbo pump as outlined in fig. 2.2.7. The oven is an insulated metal box, modified to obtain temperatures in excess of 300 °C with externally controllable heating elements. The pressure in the chamber and before the turbo pump can be recorded, and temperatures monitored with up to 8 thermocouples. Many components can withstand the maximum oven temperatures, and benefit from a high temperature or 'hard' bake. To test the pumping station the chamber was initially baked at 300 °C with blank flanges, tee-pieces, gauge, and valve, however the minimum pressure that could be obtained was not in the UHV regime.

On opening the system a mysterious blue substance was found on the gauge, possibly from the dye in coloured gloves which can "leach out when exposed to solvents" [79]. Removing this did not help reach sufficiently low pressures however. Leak detection was enabled by a residual gas analyser connected to the external pumps. This found the all-metal valve to be leaking from the screw side, and on replacing this the pressure dropped quickly.

High temperature baking was then performed with the trap, atomic ovens, and supports, with a current passed through the atomic ovens to out-gas the material further. The final high temperature bake is shown in fig. 2.2.8, and reached a pressure at gauge 2 of 4.5×10^{-8} Pa. Components that are sensitive to temperature are then baked at low temperature. The windows limit this to 200 °C, and the coatings further restrict the temperature gradient that can be tolerated to 2-3 $^{\circ}\mathrm{C\,min^{-1}}$. Additionally the bakeable ion gauge cable and ion pump, with magnets removed, are limited to 250 °C. The final low temperature bake is detailed in fig. 2.2.9, which was ended by a catastrophic oven failure.

When the chamber was valved-off and the ion pump sparked, the pressure in the trap rose rapidly, and more so with the pump turned off. This was fixed by adding a small chamber to the air side of the AMV and pumping the volume with the scroll pump to reduce the pressure differential across the valve. Following this the trap was moved to the optical table, fig. 2.2.10, where the ion pump maintains a final pressure of 1×10^{-8} Pa.

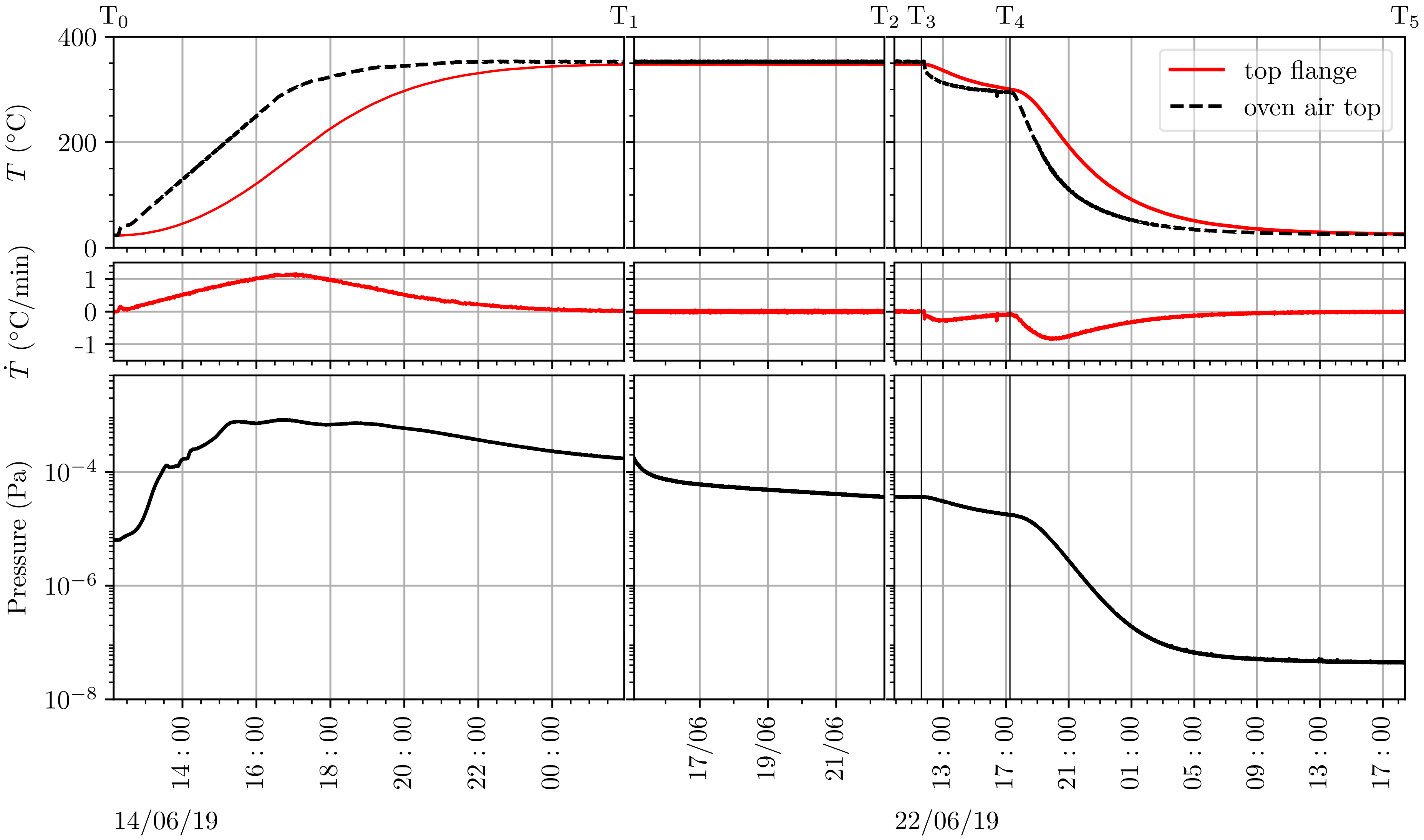

Figure 2.2.8: High temperature hard bakeout. Shows the temperature (top) and gradient (middle) at the top flange. Pressure at gauge 2 (bottom). T$_0$ − T$_1$ shows initial warm up of the oven at a rate of 1°C min^{-1} and then stabilising at 350°C. At T$_3$ one of the heating elements fails, and the temperature is ramped down at T$_4$ after approximately 1 week. Low outgassing is observed as the system has been baked several times, including with the trap assembly and unloaded atomic ovens. A pressure below 4.5×10^{-8} Pa is acheived.

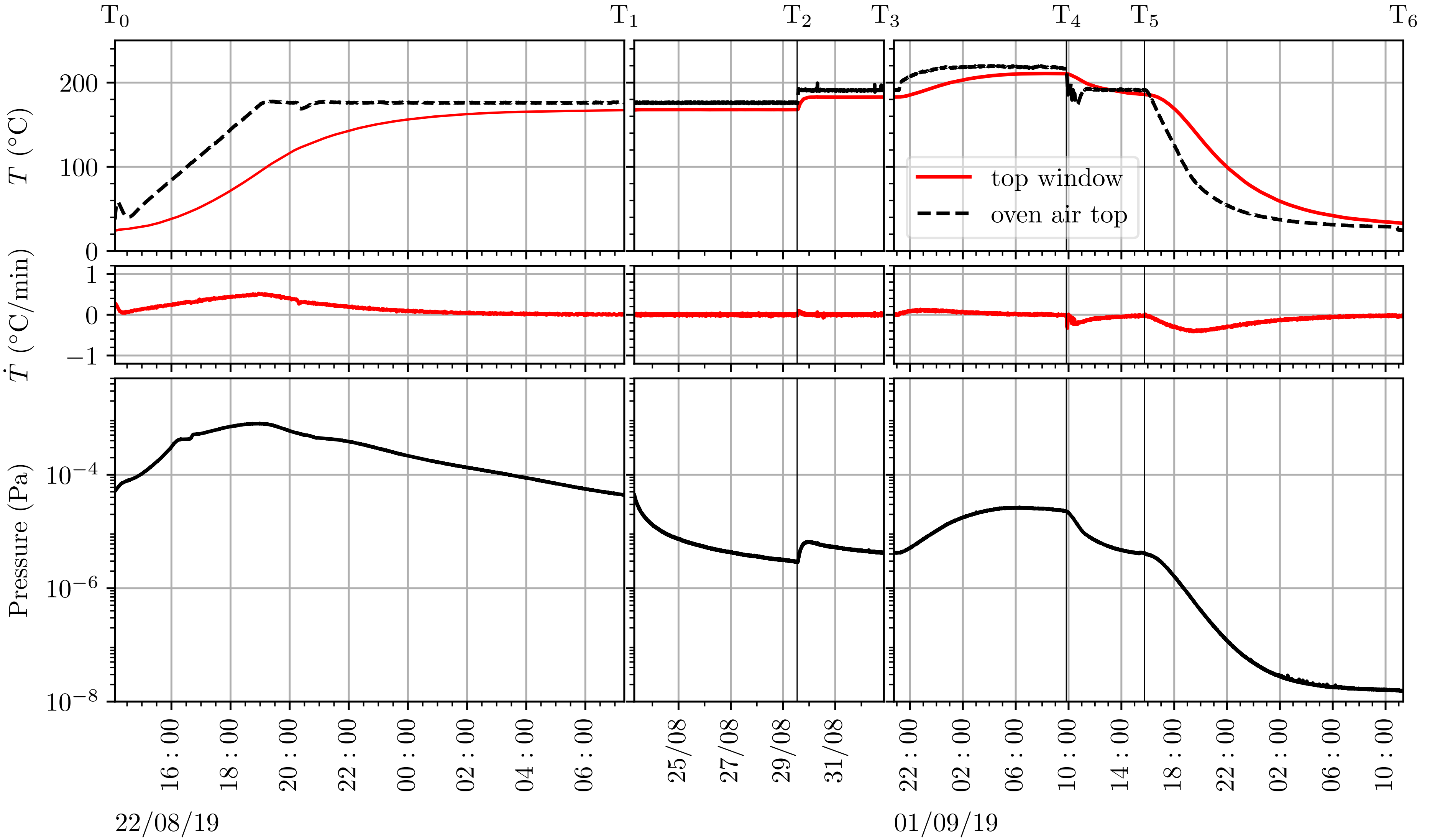

Figure 2.2.9: Low temperature soft bakeout. Shows the temperature (top) and gradient (middle) at the top window. Pressure at the trap gauge 1 (bottom). T$_0$ − T$_1$ shows initial warm up of the oven at a rate of 0.5°C min^{-1}, stabilising at 170°C. After a week, at T$_2$, the temperature is incerased to 190°C. At T$_3$ the temperature controller fails for the first time in over 20 bakes, causing the temperature to rise dangerously. Fortunately only one heater is connected, limiting the temperature at the chamber to 210°C. This is stabilitsed by T$_5$, and the temperature is lowered after almost two weeks. The chamber, heavily insulated in layers of foil, is protected from high temperature gradients in the oven, and no damage is observed. The final pressure reached is 1 × 10^{-8} Pa.

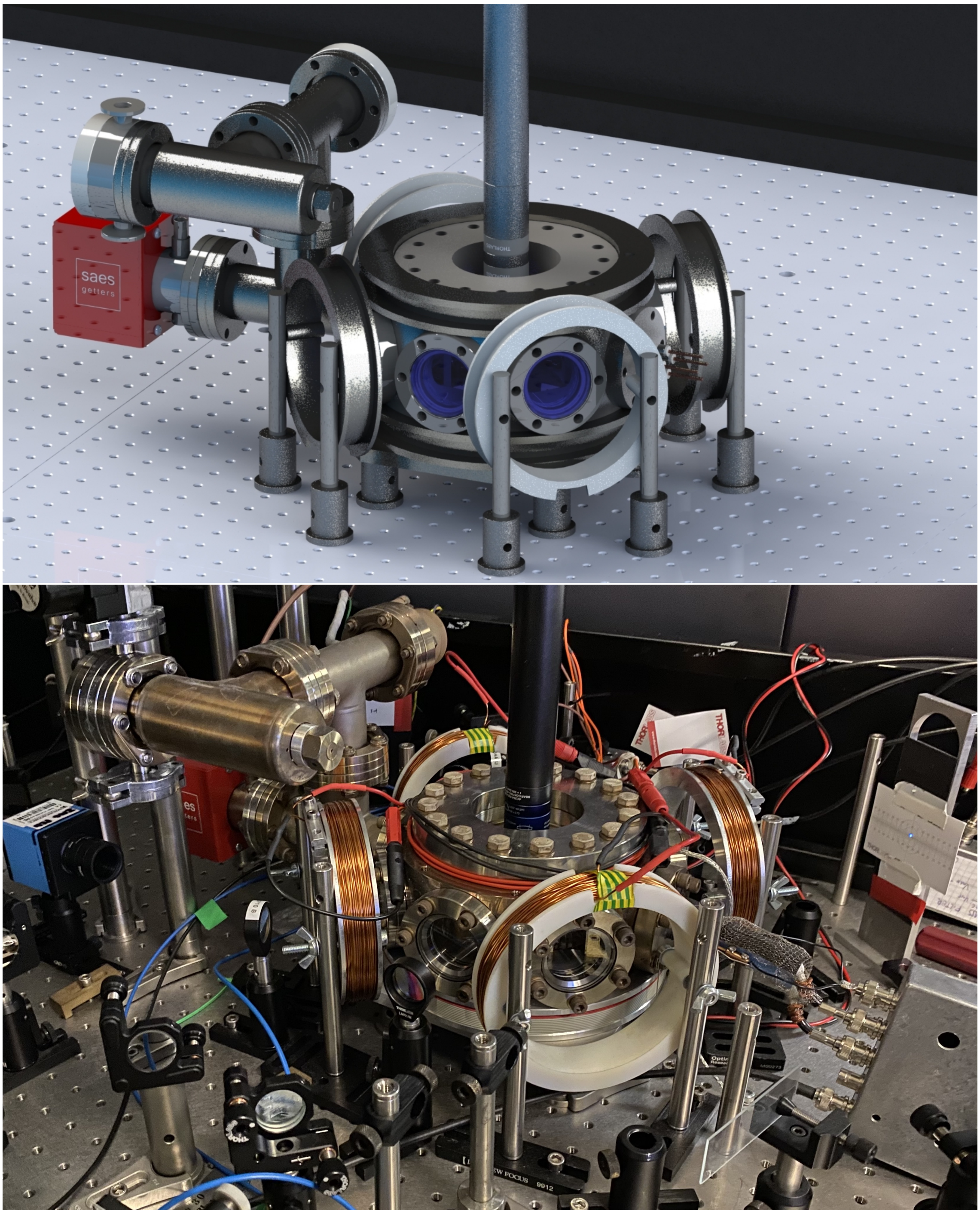

Figure 2.2.10: CAD model of the vacuum system on the optical table (top), and installed trap in reality (bottom). Any direction of magnetic field at the trap centre can be produced by three pairs of coils: horizontal metal and 3D printed coils, with $r_c = 60\,\mathrm{mm}$, and vertical trim coils mounted on the top and bottom flanges of the vacuum system, $r_c = 170\,\mathrm{mm}$.

Magnetic field coils

Engineering the desired interaction between lasers and the trapped ion requires a defined quantisation axis, which is motivated in the following chapter. A uniform magnetic field, up to 10 G, is produced at the ion by a main pair of coils, with two sets of orthogonal trim coils to compensate the field as seen in fig. 2.2.10. The magnitude of the field produced by each coil along the axis, x, defined perpendicular to and through the center of the coil, is

$$\mathrm{B}(x) = \frac{\mu_0 r_c^2 n I}{2(r_c^2 + (x - x_0)^2)^{3/2}}, \tag{2.2.15}$$

with $\mu_0 = 4\pi \times 10^{-7}\ \mathrm{H\,m^{-1}}$ the vacuum permeability, n the number of turns around the coil former, radius r_c, and I the applied current. Using a pair of coils reduces the field gradient at the ion, and the magnitude of the magnetic field is doubled in the Helmholtz configuration, although here $r_c/2x_0 \neq 1$.

The trap centre is located on the axis at a distance of $x_0 \approx 125\,\mathrm{mm}$ from the main horizontal coils, which have 160 turns, and provide a theoretical field strength of $2.7\,\mathrm{G\,A^{-1}}$ at the ion. Producing a field of 10 G therefore requires a theoretical current of $\approx 3.7\,\mathrm{A}$. The heat generated by the coils increases with the applied power, with the resistance of the coil given by $R = \rho_c n r_c / r_w^2$. The material used in 3D printed formers is potentially deformed at temperatures above 50°C. A large wire radius r_w, the low resistivity of copper ρ_c, and fewer turns reduce the required power. The horizontal trim coils therefore only have 100 turns each, and reach the maximum tolerable temperature at a current of 2.75 A, producing a theoretical field of 4.6 G. A single vertical trim coil is mounted around the bottom flange[vi], and uses ribbon cable to reduce the number of 'turns'. To do this one end of each wire in the ribbon is connected to the other end of the next wire, such that the current flows in the same direction, and giving effectively 9 turns per winding. The small wire diameter provides a high resistance, and therefore as this method generates a lot of heat it is only suitable for generating small compensation fields. The tolerable coil resistance is limited by the desire to reduce the demand on power supplies. Coil parameters are optimised to provide a large enough field with current below 5 A and required voltage below 30 V.

[vi] As seen in fig. 2.2.10 the top coil is not yet mounted.

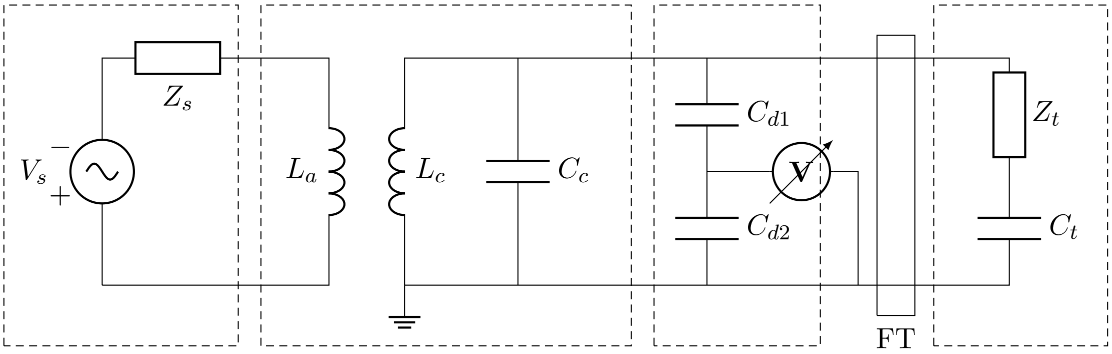

Figure 2.2.11: Effective circuit diagram for rf drive. The voltage source from the amplifier is shown on the left. The second box represents the helical resonator. A capacative divider is connected to the output of the resonator, $C_{d1} = 10\,\mu\mathrm{F}$, $C_{d2} = 100\,\mu\mathrm{F}$, where the voltage accross the trap U_p can be measured. The final box, after the rf feedthrogh, represents the trap.

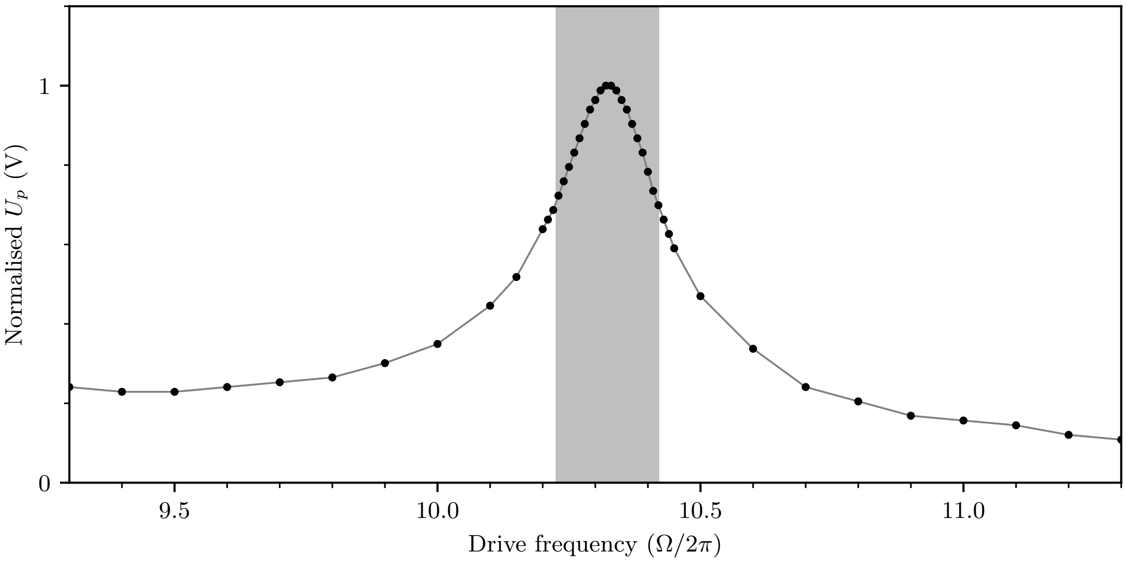

Figure 2.2.12: Amplitude of trap drive, measured across the capacative divider, as a function of drive frequency. The width of the resonance, at $1/\sqrt{2}$ the maximum amplitude, gives a Q factor of approximately 50.

Trap voltage supplies

Stable voltages should be applied to the trap electrodes in order to reduce sources of motional error. These include the amplitude of the rf field applied to the radial electrodes, and the static voltage applied to the axial endcaps. An effect of the rf field is to induce rf pickup in other, supposedly static, electrodes, which are rf grounded.

The noise in radial frequencies ω_r is directly proportional to noise in the amplitude of the rf voltage V_0, following eq. (2.2.10). A high amplitude rf signal, which from fig. 2.2.2 could be up to $\approx 500\,\mathrm{V}$, is generated using a helical resonator. This is a passive component that can be used to filter and amplify an rf source signal, and is comprised of two coils connected to the low amplitude signal and the rf electrodes. The resonator matches the impedance of the source to the trap impedance, enabling a high voltage signal with low noise. The source voltage, helical resonator, and trap, act like an RLC circuit, detailed in fig. 2.2.11, and therefore operates at a specific resonant frequency given by [80]

$$\Omega = \frac{1}{\sqrt{(C_c + C_d + C_t)L_c}}, \tag{2.2.16}$$

which can be measured experimentally[vii]. The amplitude and frequency range of the circuit is characterised by the resonator Q factor at the rf frequency Ω [80]. A higher Q factor means there is less damping in the circuit, increasing the amplitude of the amplified signal. This can be determined from the width of the resonance, $Q = \Omega/\Delta\Omega \approx 50$, shown in fig. 2.2.12.

The endcap electrodes employ a high stability power supply, see table A.1. This is sent through a low pass filter ($R = 200\,\mathrm{k\Omega}$, $C = 0.1\,\mathrm{\mu F}$) which attenuates frequency components in the signal above the cut off, $f_c \approx 8\,\mathrm{Hz}$. Compensation voltages are similarly filtered.

[vii] In order to determine the relative capacitance and inductance of the resonator and trap, the resonant frequency can be measured as a function of the capacitance of the divider, $C_d = C_{d1} + C_{d2}$, with and without the load of the trap.

Chapter 3

Laser Cooling of Trapped Ions

One of the first charged particles investigated in ion traps was the electron. A single electron in a confining potential can be thought of as analogous to the hydrogen atom, leading Dehmelt to describe a trapped electron as the geonium atom; bound to the earth. As with the hydrogen atom, properties of the geonium atom can be measured and calculated to a high degree of precision [58]. One property of the electron is its inherent spin, defined by the vector $\boldsymbol{s}$, which gives a magnetic dipole moment (MDM). An additional moment results from any orbital angular momentum, $\boldsymbol{l}$, such as from an atomic binding or the trapped motion. The total MDM of the electron

$$\boldsymbol{\mu} = \boldsymbol{\mu_s} + \boldsymbol{\mu_l} = -\mu_B(g_s\boldsymbol{s} + g_l\boldsymbol{l}), \tag{3.0.1}$$

is scaled by the Bohr magneton μ_B and the spin and orbital g-factors $g_{s,l}$, which are dimensionless parameters.

With the geonium atom, relative uncertainty in the measurement of the electron's spin magnetic moment was reduced by around three orders of magnitude in 1987 [81], and by a further factor of 15 in a modified Penning trap two decades later [82]. This was achieved by measuring the frequency of the microwave transition that induces spin flips in the electron, which is related to the g-factor. QED calculations with this measured value enable the most precise determination of the fine structure constant α. Additionally, comparison with measurements of the positron spin g-factor probes CPT invariance at a new level. Penning traps have also enabled a similar reduction in uncertainty in the magnetic moment of the proton [83]. As with the positron, analysis of antiprotons [84] shows no violation of the symmetry between matter and antimatter.

After the initial development of ion traps in the 1950s and early 1960s, the interaction with bound particles was restricted to collision studies or via global fields applied to trap electrodes. This limited the extent to which the thermal energy of ensembles could be reduced, broadening interactions and reducing trap lifetimes. With the development of lasers in the 1960s and 70s, laser cooling techniques greatly extended the range of interaction dynamics acheivable, particularly in Paul traps, with near indefinite trapping and observation of a single particle by the late 1970s [85]. Laser systems are well suited to the energy scale of atomic transitions, unlike fundamental particles, and this has resulted in the prevalence of ion based qubits in Paul traps for quantum information processing and simulation. Penning traps on the other hand have typically been used in situations where laser cooling is not required. However greater precision in measurement of the properties of protons and antiprotons will be possible with sympathetically laser cooled ions [86, 87]. There is also the possibility of mapping states of the (anti)proton to the ion for non-destructive detection [88]. This motivates the group's recent study of ground state cooling in the radial modes of a single ion in a Penning trap [17].

In section 3.1 the benefits of ionised calcium are discussed, and the dynamics of the interaction between a laser field and its atomic transitions are introduced in section 3.2. As the atom is also bound to the trap, the radiation field can be tuned to engineer coupling between electronic and motional states, section 3.3, and this coupling between the qubit and an n-level system allows for the exploration of more interesting dynamics. In section 3.4 two complementary methods of laser cooling are discussed for the more simple case of the Paul trap: Doppler cooling, where photons are rapidly scattered to damp the motion of the ion; and sideband cooling, where the motion of the harmonic oscillator is coherently driven to the ground state.

3.1 Singly Ionised Calcium - ^{40}Ca$^+$

Complexity in the energy level structure of an atom is reduced in the case of a single electron bound to a central field [92]. In the alkali metals, such as potassium, and ionised alkaline earth metals such as Ca$^+$, a single valence electron exists outside a closed set of subshells. States of the electronic wavefunction can be described by three quantum numbers: $|n, l, m_l\rangle$. In a hydrogen atom, where the potential is defined by a point charge and is therefore a pure Coulomb potential, the energy levels in the non-relativistic approximation depend only on the principal quantum number n. The orbital angular momentum number, $l \leq n-1$, can take multiple values for $n > 1$, and the degeneracy of these states is lifted by the effect on the potential of the inner electrons in more complex atoms. The lowest lying energy levels of ionised ^{40}Ca$^+$ are shown in fig. 3.1.1.

In the limit of a weak magnetic field of the form $\mathbf{B} = \mathrm{B}_{z'}\boldsymbol{z'}$, where $\boldsymbol{z'}$ is the quantisation axis[i], the spin and orbital angular momentum from eq. (3.0.1) are coupled. The electronic state can then be described by a single total angular momentum quantum number $\boldsymbol{j} = \boldsymbol{s}+\boldsymbol{l}$. The magnetic quantum number, now $|m_j| \leq j$, describes the projection of the angular momentum onto this quantisation axis. Degeneracy in m_j is lifted via the interaction $-\boldsymbol{\mu}\cdot\mathbf{B}$, with the frequency shift of m_j states relative to the field free energy given by

$$\Delta\nu = \frac{\mu_B}{h} g_j m_j \mathrm{B}_{z'}. \tag{3.1.1}$$

The Landé g-factor g_j given in table 3.1.1 combines spin and orbital g-factors. In this regime the electronic state can be defined in terms of angular momentum and magnetic quantum numbers, $|\psi\rangle = |j, m_j\rangle$.

The short lifetime of the excited state in the dipole allowed[ii] $\mathrm{S}_{1/2,m_j} \leftrightarrow \mathrm{P}_{1/2,m_j'}$ transitions facilitates rapid scattering of photons and a consequent damping force. Heavier elements also have accessible d states, where an optical qubit can be realised in two states coupled by $\mathrm{S}_{1/2,m_j} \leftrightarrow \mathrm{D}_{5/2,m_j'}$ quadrupole transitions. As these are dipole forbidden the excited state has a decay time of over 1 s, indicated by the narrow linewidth in table 3.1.2. Additionally the two ground states $\mathrm{S}_{1/2,\pm1/2}$ can form a qubit basis, virtually coupled via a Raman transition with the $\mathrm{P}_{1/2}$ state.

---

[i] $\boldsymbol{z'}$ is used to avoid confusion with the direction of axial motion $\boldsymbol{z}$.

[ii] Dipole selection rules: $\Delta l = \pm1$ and $\Delta m_j = 0, \pm1$.

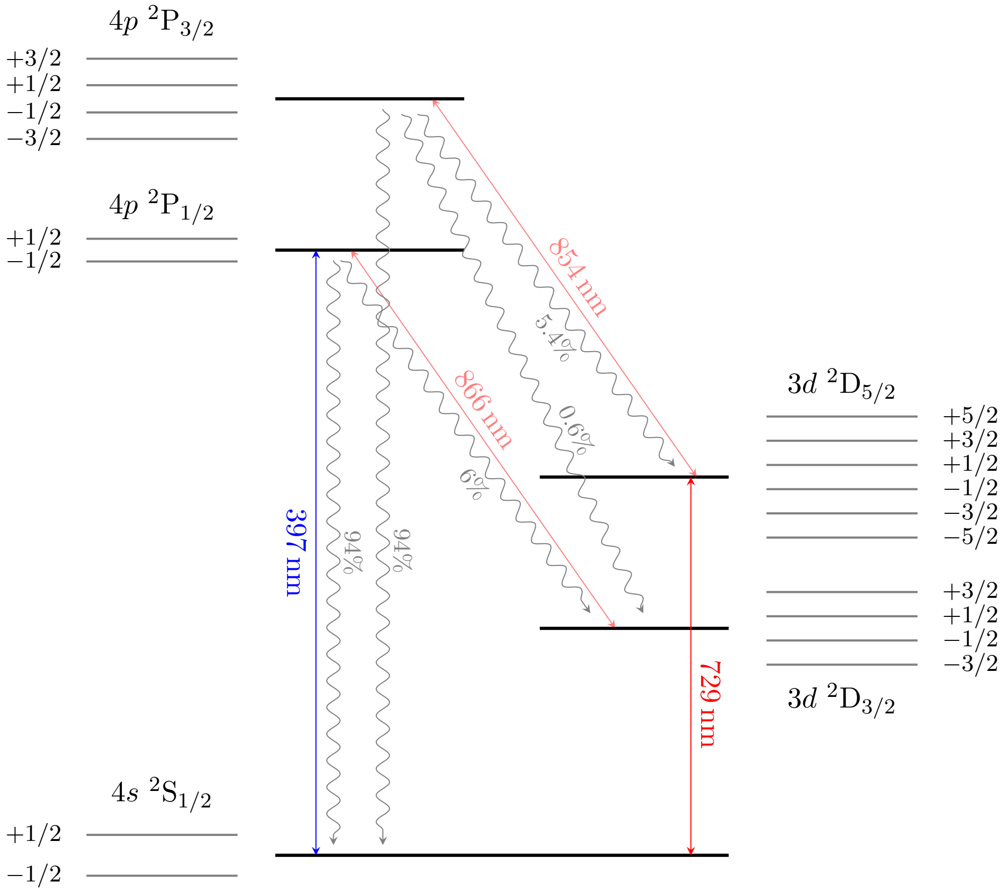

Figure 3.1.1: Laser addressed energy levels of singly ionised calcium, $^{40}\mathrm{Ca}^+$, where the ground state $n = 4$. States $l = 0, 1, 2$ are termed s, p, d, and levels are denoted by $^2L_{j,m_j}$, with terms further described in the text. Laser addressed transitions are highlighted, with more detail in table 3.1.2. Grey arrows show branching ratios from the P states [89]. Splitting of sub-levels with magnetic field is proportional to the g-factor g_j given in table 3.1.1.

Level	$\mathrm{S}_{1/2}$	$\mathrm{P}_{1/2}$	$\mathrm{P}_{3/2}$	$\mathrm{D}_{3/2}$	$\mathrm{D}_{5/2}$
g_j	2	2/3	4/3	4/5	6/5

Table 3.1.1: Landé g-factors for lowest lying energy levels. In a weak quantisation field these are determined by $g_j = 1 + [j(j+1) + s(s+1) - l(l+1)]/2j(j+1)$.

i	Transition	ν_i (THz)	Δl	$\Gamma_i/2\pi$ (MHz)
397	$\mathrm{S}_{1/2} \leftrightarrow \mathrm{P}_{1/2}$	755.22271	1	21.8
729	$\mathrm{S}_{1/2} \leftrightarrow \mathrm{D}_{5/2}$	411.042130	2	0.136×10^{-6}
866	$\mathrm{D}_{3/2} \leftrightarrow \mathrm{P}_{1/2}$	346.00001	1	1.7
854	$\mathrm{D}_{5/2} \leftrightarrow \mathrm{P}_{3/2}$	350.86282	1	1.6

Table 3.1.2: Resonant frequency ν_i and linewidth Γ_i of laser addressed transitions [90, 91]. The 729 transition is dipole forbidden, and this is reflected in its narrow linewidth.

3.2 Atom-Light Interactions

Observations of the interaction between light and matter have resulted in an extensive array of mathematical tools which describe these most fundamental physical interactions. In this section a model will be presented for the experimental realisation of a physical atomic qubit, and for its manipulation by an external laser field. The classical description of a harmonically bound electron in a Kepler orbit about a massive nucleus offers an intuitive insight into the interaction between light and atoms [93]. However in order to describe experimental observations of atomic structure, in 1913 Bohr postulated that there were certain stable orbits, where classical radiation was not emitted, and that when an electron transitioned between orbits it emitted radiation given by their energy difference. This somewhat unsatisfactory situation was resolved by de Broglie, who proposed that matter behaved like a wave, and that constructive interference of the matter wave gave rise to the stationary orbits of Bohr. The condition for a stable orbit is that circumference, defined by radius r, is an integer number of de Broglie wavelengths, $2\pi r = n\lambda_{dB}$, where $\lambda_{dB} = h/p$ is related to the momentum of the particle. The wave equation

$$\mathcal{H}\Psi(t) = i\hbar\frac{d\Psi(t)}{dt} \tag{3.2.1}$$

was presented by Erwin Schrödinger shortly after in 1926 to describe the evolution of the matter wave described by state $\Psi(t)$ and Hamiltonian $\mathcal{H}$.

The Hamiltonian for an atom in an electromagnetic field is comprised of a free term, describing the atomic energy, and an interaction term which describes the perturbation of the eigenfunctions of the free Hamiltonian by the external laser field,

$$\mathcal{H} = \mathcal{H}_A + \mathcal{H}_i(t). \tag{3.2.2}$$

It is often possible to consider matter as composed of a higher and lower energy level, where the excited state can decay back to the ground. The atom is modelled as a two level system, mapping the electronic state onto the spin half operator basis[iii], under the assumption that the states, separated by $\hbar\omega_0$, are long lived, and that no other levels are resonant. This is expressed using the Pauli z-operator, with the ground $|{\downarrow}\rangle$ and excited

---

[iii] Pauli operators: $\sigma_x = |{\downarrow}\rangle\langle{\uparrow}| + |{\uparrow}\rangle\langle{\downarrow}|$, $\sigma_y = i(|{\downarrow}\rangle\langle{\uparrow}| - |{\uparrow}\rangle\langle{\downarrow}|)$, $\sigma_z = |{\uparrow}\rangle\langle{\uparrow}| - |{\downarrow}\rangle\langle{\downarrow}|$.

$|{\uparrow}\rangle$ states the eigenvectors of the Hamiltonian

$$\mathcal{H}_A = \frac{\hbar\omega_0}{2}\sigma_z. \tag{3.2.3}$$

The interaction term

$$\mathcal{H}_i(t) = -q\boldsymbol{r}\cdot\boldsymbol{E}(t), \tag{3.2.4}$$

includes the time dependent contribution from the interaction between the atomic dipole and the oscillating electric field $\boldsymbol{E}(t)$. The electric field is described in terms of the position operator of the valence electron $\boldsymbol{r}$, defined relative to the center of mass of the ion which is static at the energy scale of the electron. An intense laser field, with polarisation vector $\boldsymbol{\epsilon}$, is treated as a classical plane wave defined by amplitude E_0, wavevector $\boldsymbol{k}$, frequency ω, and phase ϕ. This is expressed at the position of the atom,

$$\boldsymbol{E}(t) = \frac{\boldsymbol{\epsilon}E_0}{2}\left[e^{i(\boldsymbol{k}\cdot\boldsymbol{r}-\omega t+\phi)} + e^{-i(\boldsymbol{k}\cdot\boldsymbol{r}-\omega t+\phi)}\right]. \tag{3.2.5}$$

Consequently the interaction Hamiltonian can be written

$$\mathcal{H}_i(t) = -\frac{qE_0}{2}(\boldsymbol{r}\cdot\boldsymbol{\epsilon})e^{i\boldsymbol{k}\cdot\boldsymbol{r}}\left[e^{-i(\omega t-\phi)} + e^{i(\omega t-\phi)}\right]. \tag{3.2.6}$$

When the gradient of the electric field is constant over the spatial extent of the electronic wavefunction, then the dipole approximation is valid, and the spatial term can be Taylor expanded $e^{i\boldsymbol{k}\cdot\boldsymbol{r}} \approx 1 + i\boldsymbol{k}\cdot\boldsymbol{r}$. Consequently dipole transitions, where the zeroth order is taken, are fast compared to the quadrupolar case where there is no dipole moment, and higher order terms are small in the expansion of a small parameter. This expansion can be incorporated into a general term which describes the coupling strength between the two states called the Rabi frequency Ω_0, which is discussed in section 3.2.2.

The interaction Hamiltonian can be converted to matrix form by calculating the matrix elements following

$$\langle{\uparrow}|\,\mathcal{H}_i(t)\,|{\downarrow}\rangle = \frac{\hbar\Omega_0}{2}\left[e^{-i(\omega t-\phi)} + e^{i(\omega t-\phi)}\right]. \tag{3.2.7}$$

A general solution for the interaction term [94] can then be expressed with the operators $\sigma_+ = |\uparrow\rangle\langle\downarrow|$ and $\sigma_- = |\downarrow\rangle\langle\uparrow|$,

$$\mathcal{H}_i(t) = \frac{\hbar\Omega_0}{2}\left[\sigma_+ + \sigma_-\right]\left[e^{-i(\omega t-\phi)} + e^{i(\omega t-\phi)}\right]. \tag{3.2.8}$$

Interaction Picture

It is illustrative to look at the dynamics in the frame of reference of the ion by transformation into the interaction picture. The interaction Hamiltonian, defined by $\mathcal{H}_{int} = e^{i\mathcal{H}_A t/\hbar}\mathcal{H}_i e^{-i\mathcal{H}_A t/\hbar}$, is then

$$\mathcal{H}_{int}(t) = \frac{\hbar\Omega_0}{2}\left[\sigma_+ e^{-i(\delta t-\phi)} + \sigma_- e^{i(\delta t-\phi)}\right], \tag{3.2.9}$$

where $\delta = \omega - \omega_0$ is the detuning of the laser frequency from the atomic resonance. Fast oscillating contributions of the form $e^{i(\omega_0+\omega)t}$ are also neglected in the rotating wave approximation, as they have minimal effect on the time evolution.

Solutions

Evolution of the electronic state in the presence of a resonant field is determined by solving the Schrödinger equation. The atomic wavefunction of a two-level atom can be written

$$|\psi(t)\rangle = c_\downarrow(t)\,|\downarrow\rangle + c_\uparrow(t)\,|\uparrow\rangle\,, \tag{3.2.10}$$

with the state described in terms of the normalised complex amplitudes, $|c_\downarrow|^2 + |c_\uparrow|^2 = 1$, of qubit basis states $|\downarrow\rangle$ and $|\uparrow\rangle$.

Solutions can be expressed in terms of a time evolution propagator $U_{int}(t)$ acting on initial state populations, such that the state in eq. (3.2.10) is equal to $U_{int}(t)(c_\downarrow(0)\,|\downarrow\rangle + c_\uparrow(0)\,|\uparrow\rangle)$. This propagator is derived in refs [71, 94], and is given by

$$U_{int}(t,\delta,\Omega_0,\phi) = \begin{bmatrix} e^{-\frac{it\delta}{2}}\left(\cos\left(\frac{t\Omega}{2}\right) + \frac{i\delta\sin\left(\frac{t\Omega}{2}\right)}{\Omega}\right) & -\frac{\Omega_0}{\Omega} i e^{i(\phi-\frac{t\delta}{2})}\sin\left(\frac{t\Omega}{2}\right) \\ -\frac{\Omega_0}{\Omega} i e^{i(\phi-\frac{t\delta}{2})}\sin\left(\frac{t\Omega}{2}\right) & e^{\frac{it\delta}{2}}\left(\cos\left(\frac{t\Omega}{2}\right) - \frac{i\delta\sin\left(\frac{t\Omega}{2}\right)}{\Omega}\right) \end{bmatrix}, \tag{3.2.11}$$

where $\Omega = \sqrt{\Omega_0^2 + \delta^2}$. From an initial ground state, the probability of excitation results in the familiar oscillations at the modified Rabi frequency Ω, with the amplitude reduced

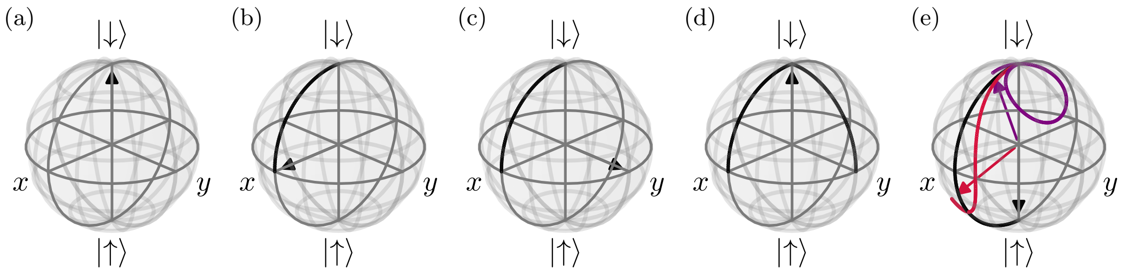

Figure 3.2.1: Bloch sphere representation showing (a) the qubit initialised in the ground state, (b) a $\pi/2$ rotation about the y-axis described by the propagator $U_{int}(\pi/2, 0, 1, 0)$ creates an equal superposition state, (c) the state acquires phase $\phi = \pi/2$, (d) from here a rotation of $\pi/2$ about the x-axis, with the laser phase shifted by $\phi = \pi/2$, $U_{int}(\pi/2, 0, 1, \pi/2)$, brings the population back to the initial state. A detuning from the qubit frequency results in an accumulated phase $\phi = \delta t$, shown in (e) for a π rotation, with no detuning (black) $\delta = \Omega/2$ (red) and $\delta = 2\Omega$ (purple).

by any detuning,

$$|c_{\uparrow}(t)|^2 = |\langle\uparrow| U_{int}(t) |\downarrow\rangle|^2 = \frac{\Omega_0^2}{\Omega^2} \sin^2\left(\frac{\Omega t}{2}\right). \tag{3.2.12}$$

3.2.1 Bloch Sphere

The Bloch sphere provides a clear conceptualisation of the interaction defined by eq. (3.2.11). Here the qubit state is represented by a point on a unit sphere,

$$\psi = \cos\left(\frac{\theta}{2}\right)|\downarrow\rangle + \sin\left(\frac{\theta}{2}\right)e^{i\phi}|\uparrow\rangle, \tag{3.2.13}$$

with spherical coordinates θ and ϕ. The effect of driving the qubit on resonance is a rotation of angle $\Omega_0 t$ about the y-axis, effectively defined by the initial laser phase. The time taken to transfer population from the ground to excited states is therefore π/Ω_0, termed a π-pulse. A detuning from the transition frequency causes the accumulation of phase $\phi = \delta t$, and results in a more complicated trajectory seen in fig. 3.2.1 (e). A projective measurement onto the z-axis gives the reduced amplitude oscillations of eq. (3.2.12).

The state $(|\downarrow\rangle + |\uparrow\rangle)/\sqrt{2}$ is created by a resonant $\pi/2$-pulse. Advancing the phase of a second $\pi/2$-pulse is equivalent to taking a different rotation axis in the horizontal plane. A phase shift of $\phi = \pi$ would bring the population back to ground, $|\downarrow\rangle$. Advancing the phase by $\phi = \pi/2$, a rotation about the x-axis, would leave the superposition state unaffected. This is clarified in fig. 3.2.1 (a) to (d).

j'				$^5\!/_2$			$^1\!/_2$	
m_j'	$-\,^5\!/_2$	$-\,^3\!/_2$	$-\,^1\!/_2$	$+\,^1\!/_2$	$+\,^3\!/_2$	$+\,^5\!/_2$	$-\,^1\!/_2$	$+\,^1\!/_2$
$\Lambda(^1\!/_2,\,-\,^1\!/_2)$	$\sqrt{^1\!/_3}$	$-\sqrt{^4\!/_{15}}$	$\sqrt{^1\!/_5}$	$-\sqrt{^2\!/_{15}}$	$\sqrt{^1\!/_{15}}$	-	$-\sqrt{^1\!/_3}$	$\sqrt{^2\!/_3}$
$\Lambda(^1\!/_2,\,+\,^1\!/_2)$	-	$\sqrt{^1\!/_{15}}$	$-\sqrt{^2\!/_{15}}$	$\sqrt{^1\!/_5}$	$-\sqrt{^4\!/_{15}}$	$\sqrt{^1\!/_3}$	$\sqrt{^2\!/_3}$	$-\sqrt{^1\!/_3}$

Table 3.2.1: Clebsch-Gordan coefficients $\Lambda(j, m_j)$ for $\mathrm{S}_{1/2} \leftrightarrow \mathrm{D}_{5/2}$ and $\mathrm{S}_{1/2} \leftrightarrow \mathrm{P}_{1/2}$ transitions. From ([67],A.A).

3.2.2 Rabi Frequency

The coupling strength Ω_0 is evaluated in refs [67, 90] for dipole (E1) and quadrupole (E2) transitions,

$$|\Omega_0^{(E1)}| = |\frac{qE_0}{\hbar} \langle\downarrow| \boldsymbol{\epsilon} \cdot \boldsymbol{r} |\uparrow\rangle |, \tag{3.2.14}$$

$$|\Omega_0^{(E2)}| = |\frac{qE_0}{2\hbar} \langle\downarrow| (\boldsymbol{k} \cdot \boldsymbol{r})(\boldsymbol{\epsilon} \cdot \boldsymbol{r}) |\uparrow\rangle |. \tag{3.2.15}$$

In the case of the quadrupole transition this is evaluated in ref [90] as

$$\Omega_0 = \frac{qE_0}{2\hbar}\sqrt{\frac{15\Gamma}{c\alpha_0 k^3}}\Lambda(j, m_j, j', m_j')g^{k,\Delta m_j}(\phi, \gamma), \tag{3.2.16}$$

where Γ is the transition linewidth, c the speed of light, and α_0 the fine structure constant. For both types of transition the Rabi frequency Ω_0 is dependent on properties of ground j, m_j and excited j', m_j' states, and is proportional to the Clebsch-Gordan coefficient $\Lambda(j, m_j, j', m_j')$ given in table 3.2.1. The coupling strength is also determined by the direction and polarisation of the laser. The functional form of the geometric term $g^{k,\Delta m_j}(\phi, \gamma)$ is given in ([67],A.B), and is parameterised by:

ϕ - the angle between laser wavevector ($\boldsymbol{k}$) and magnetic field ($\mathbf{B}$)

γ - the angle between polarisation vector ($\boldsymbol{\epsilon}$) and the projection of $\mathbf{B}$ in the plane normal to $\boldsymbol{k}$.

The definitions here assume linear polarisation. Pure circular polarisation is parametrised only by angle ϕ. The interaction strength differs for dipole ($k = 1$) and quadrupole ($k = 2$) transitions, shown in figs. 3.2.2 and 3.2.3 respectively.

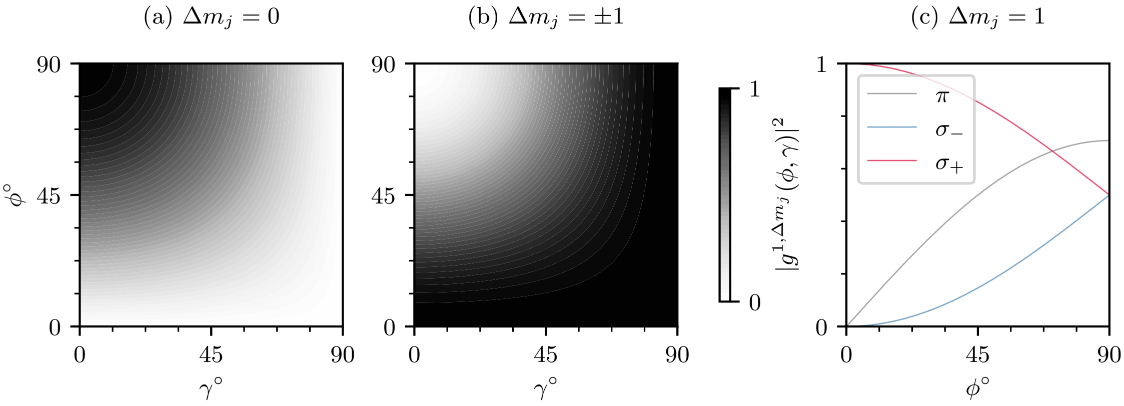

Figure 3.2.2: Dipole transition coupling strengths $|g^{1,|\Delta m_j|}(\phi,\gamma)|^2$ with linear polarisation for π-transitions (a) and σ-transitions (b). (c) The strength of σ_+-transitions, $\Delta m_j = 1$. At $\phi = 0$, right handed circularly polarised light (σ_+ in legend) counter-propagating with the quantisation axis couples only to σ_+-transitions.

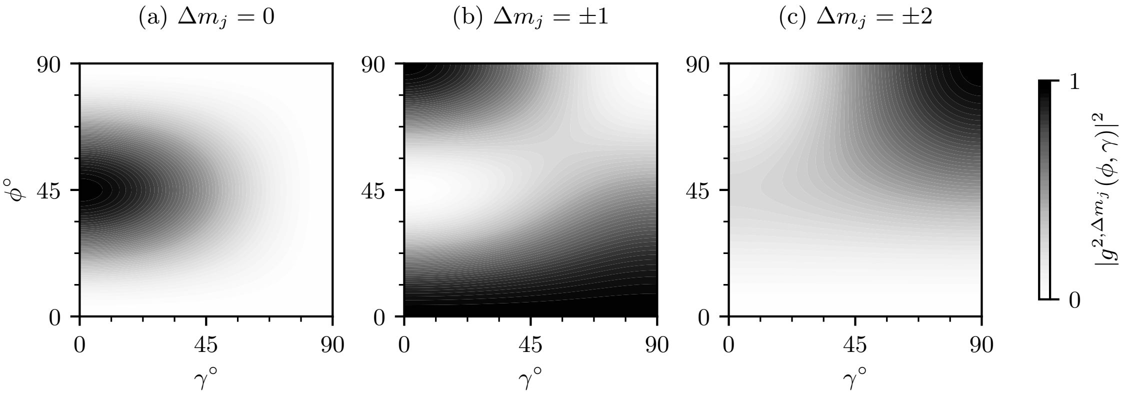

Figure 3.2.3: Quadrupole transition strength as a function of interaction geometry $|g^{2,|\Delta m_j|}(\phi,\gamma)|^2$ for linearly polarised light for (a) π-transitions, (b) σ-transitions, and (c) δ-transitions.

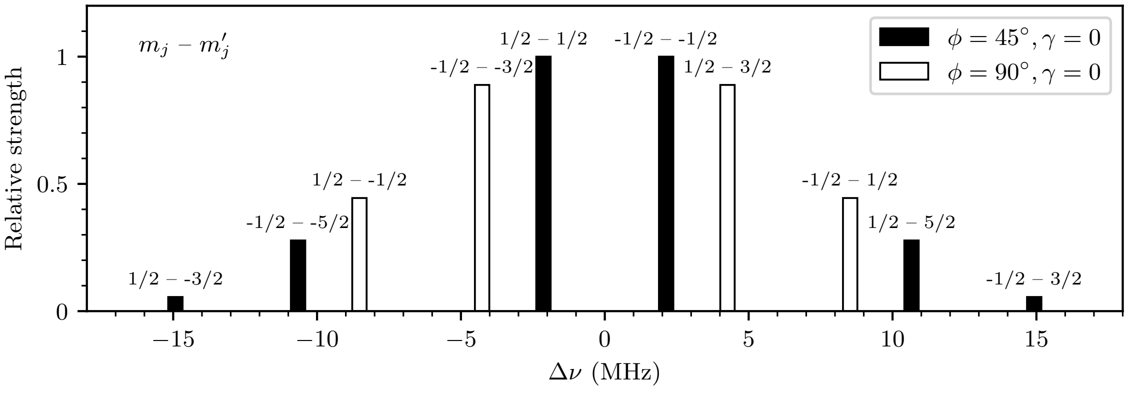

Figure 3.2.4: $S_{1/2} \leftrightarrow D_{5/2}$ quadrupole transitions with the magnitude of the quantisation field $B_{z'} = 0.39\,\text{mT}$. For the two geometric configurations indicated in the legend, it is only possible to couple to σ-transitions (white) or π and δ (black). The two $\Delta m_j = 0$ transitions are not only stronger than others for the same laser power, but are least sensitive to noise in the magnetic field.

m_j	m'_j	Δm_j		$\Delta\nu_t$ (MHz/G)
$-1/2$	$-5/2$	-2	δ_-	-2.799
	$-3/2$	-1	σ_-	-1.120
	$-1/2$	0	π	0.560
	$1/2$	1	σ_+	2.239
	$3/2$	2	δ_+	3.919
$1/2$	$-3/2$	-2	δ_-	-3.919
	$-1/2$	-1	σ_-	-2.239
	$1/2$	0	π	-0.560
	$3/2$	1	σ_+	1.120
	$5/2$	2	δ_+	2.799

Table 3.2.2: Splitting of $S_{1/2,m_j} \leftrightarrow D_{5/2,m'_j}$ transitions with magnetic field strength, given in units of MHz per Gauss, where 1 G = 10 mT.

Available Quadrupole Transitions

Quadrupole selection rules allow transitions where the change in magnetic quantum number $\Delta m_j = 0, \pm 1, \pm 2$, resulting in 5 available transitions from each of the two ground states. These are termed $\pi, \sigma_\pm$, and $\delta_\pm$ transitions respectively. The transitions are suppressed to a greater or lesser extent by the geometry of the interaction and the Clebsch-Gordan coefficient. The strength of the different transitions can be seen for two configurations of the laser field in fig. 3.2.4, both have a vertically polarised laser, which couples only to σ-transitions where the laser is perpendicular to the quantisation axis, and predominantly to π-transitions with the laser at 45°. The change in frequency of a particular transition from the field free value is proportional to the magnetic field, and is shown in table 3.2.2.

3.3 Laser Interaction with a Trapped Ion

The description of the interaction is further developed by incorporating the motion of the ion in the trap, as in ref [94]. If the ion is oscillating along the projection of the laser wavevector, the laser field in the reference frame of the ion will be modulated at the trap frequency. This gives rise to sidebands analogous to radio frequency modulation, from which the term carrier is borrowed to describe the principal transition, about which the sidebands are symmetrically arranged.

The free Hamiltonian is modified to include the energy of the motion, a single mode of harmonic oscillation at frequency ω_z. The Hamiltonian for a quantum harmonic oscillator in one dimension is

$$\mathcal{H}_M = \frac{\hat{p}^2}{2M} + \frac{M\omega_z^2\hat{z}^2}{2}, \tag{3.3.1}$$

where the momentum and position operators can be written in terms of creation $\hat{a}^\dagger$ and annihilation $\hat{a}$ operators,

$$\hat{z} = \sqrt{\frac{\hbar}{2M\omega_z}}(\hat{a}+\hat{a}^\dagger), \qquad \hat{p} = i\sqrt{\frac{\hbar M\omega_z}{2}}(\hat{a}^\dagger - \hat{a}). \tag{3.3.2}$$

Consequently the free and interaction Hamiltonians are given by

$$\mathcal{H}_A = \frac{\hbar\omega_0}{2}\sigma_z + \hbar\omega_z\left[\hat{a}^\dagger\hat{a} + \frac{1}{2}\right], \tag{3.3.3}$$

$$\mathcal{H}_i(t) = \frac{\hbar\Omega_0}{2}[\sigma_+ + \sigma_-]\left[e^{-i(\omega t - k_z\hat{z}-\phi)} + e^{i(\omega t - k_z\hat{z}-\phi)}\right]. \tag{3.3.4}$$

The axial projection of the wavevector $k_z = k\cos\theta_z$, where θ_z is the angle between k and the motional z-axis. This gives a phase modulation term dependent on the position operator $\hat{z}$, but the interaction term is otherwise the same as in eq. (3.2.8).

The Hamiltonian in the interaction picture is now

$$\mathcal{H}'_{int}(t) = \frac{\hbar\Omega_0}{2}\left[\sigma_+ e^{-i(\delta t - \eta(\tilde{a}+\tilde{a}^\dagger)-\phi)} + \sigma_- e^{i(\delta t - \eta(\tilde{a}+\tilde{a}^\dagger)-\phi)}\right]. \tag{3.3.5}$$

The position operator is replaced with creation and annihilation operators, modified in the interaction picture to $\tilde{a} = e^{-i\omega_z t}\hat{a}$. In eq. (3.3.5) the coupling between different motional levels and the qubit is given by the tensor product of $\sigma_\pm$ and $e^{\hat{a}^{(\dagger)}}$ terms. As previously, we can make a Taylor expansion of the exponential to give terms whose relative strengths are characterised by the coupling between electronic and motional states. The relative strengths of these interactions are characterised by the Lamb–Dicke parameter,

$$\eta = k_z z_0, \qquad \text{where} \qquad z_0 = \sqrt{\frac{\hbar}{2M\omega_z}}$$

is the spatial extent of the ground state wave function along the z-axis. This is a fixed parameter for a given angle θ_z and trap frequency. More specifically the Lamb–Dicke parameter quantifies the relative coupling strength between the qubit and motional states. As this parameter is reduced, the chance of a change in the motional state during decay from the excited qubit state is decreased.

A general state can now be written in terms of the qubit and harmonic oscillator state, n,

$$|\psi\rangle = \sum_{n=0}^{\infty} c_{\downarrow,n} |\downarrow, n\rangle + c_{\uparrow,n} |\uparrow, n\rangle . \tag{3.3.6}$$

The Rabi frequency is modified [90] to include motional coupling between states $|n\rangle$ and $|n+m\rangle$,

$$\Omega_{n,n+m} = \Omega_0 |\langle n+m| e^{i\eta(a+a^\dagger)} |n\rangle|. \tag{3.3.7}$$

The derivation of these terms can be found in ref [90], and are given by

$$\Omega_{n,n+m} = \Omega_0 e^{-\frac{1}{2}\eta^2} \eta^{|m|} \sqrt{\frac{n_<!}{n_>!}} L_{n_<}^{|m|}(\eta^2), \tag{3.3.8}$$

with $n_<(n_>)$ indicating the lesser (greater) of n and $n+m$. $L_n^m(x)$ is the generalised Laguerre polynomial.

3.3.1 The Lamb–Dicke Regime

In the Lamb-Dicke regime the extent of the ions wavefunction experiences the same phase in the laser field. The condition for this regime is defined by

$$\eta\sqrt{2\bar{n}+1} \ll 1. \tag{3.3.9}$$

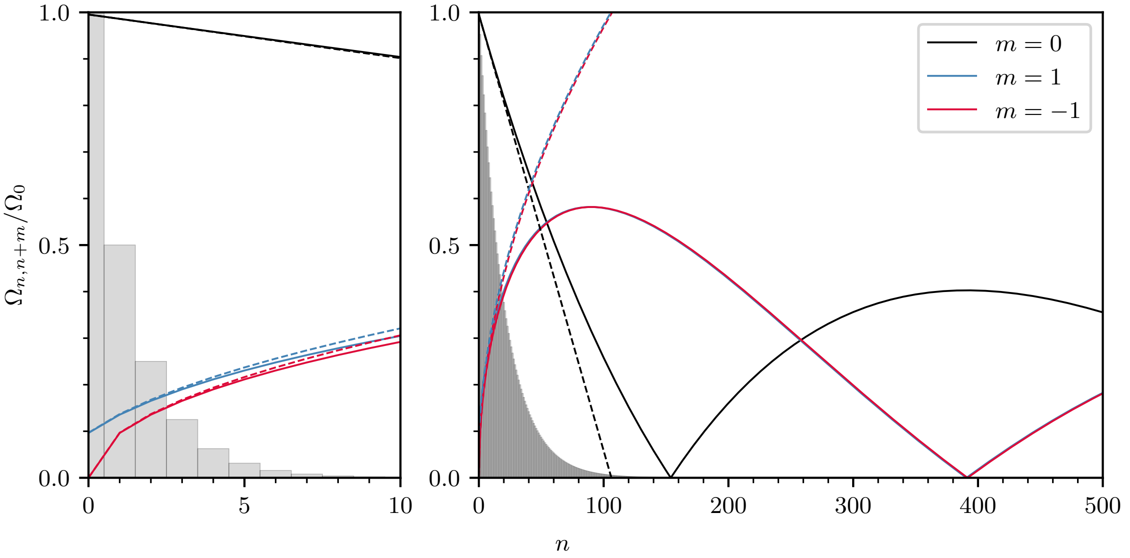

Figure 3.3.1: Normalised coupling strengths for carrier (black) and first order red and blue sidebands with $\eta = 0.1$. The LD approx is also shown (dashed) and well approximates the sideband strength for lower oscillator states. Scaled Boltzmann distributions, $P'(n) = 1/P(0) \times P(n)$, are shown for mean occupations $\bar{n} = 1$ (left) and 20 (right).

This allows the expansion of eq. (3.3.7) to be truncated, simplifying the equations for modified Rabi frequencies for the first red sideband, carrier, and first blue sideband:

$$\Omega_{n,n-1} = \Omega_0 \eta \sqrt{n}, \tag{3.3.10}$$

$$\Omega_{n,n} = \Omega_0 \left[1 - \frac{1}{2}\eta^2(2n+1)\right], \tag{3.3.11}$$

$$\Omega_{n,n+1} = \Omega_0 \eta \sqrt{n+1}. \tag{3.3.12}$$

The coupling strength of carrier and first order sideband transitions can be seen in fig. 3.3.1 for this regime, and the strength calculated in eq. (3.3.8). The motion after cooling is discussed in the following section, however it is enough to say here that the LD approximation holds for $\eta < 0.1$ if the motion is in the lowest few harmonic oscillator states. Most quantum information experiments are conducted in the LD regime, as modelling is greatly simplified, and cooling requirements are not overly stringent, especially at high trap frequencies.

First Order Pulses

In the experiments presented in chapter 5, the motional and internal states are manipulated with only carrier, red, and blue sideband pulses. These first order pulses are the only transitions with significant coupling strength in the LD regime, and can be defined with respect to the propagator U_{int} from eq. (3.2.11),

$$\mathcal{U}_r(A,\phi) = U_{int}(A/\Omega_{n,n-1}, 0, \Omega_{n,n-1}, \phi), \tag{3.3.13}$$

$$\mathcal{U}_c(A,\phi) = U_{int}(A/\Omega_{0,0}, 0, \Omega_0, \phi), \tag{3.3.14}$$

$$\mathcal{U}_b(A,\phi) = U_{int}(A/\Omega_{n,n+1}, 0, \Omega_{n,n+1}, \phi), \tag{3.3.15}$$

where it is assumed that the laser is tuned to the transition resonance ($\delta = 0$). The parameter A is the pulse area, defined such that $\mathcal{U}_c(\pi, 0)$ fully excites the qubit from the ground state, taking time $\tau = \pi/(2\Omega_{0,0})$, and the operations $\mathcal{U}_r(\pi, 0)$ and $\mathcal{U}_b(\pi, 0)$ drive transitions from $|\downarrow, n\rangle$ to the states $|\uparrow, n-1\rangle$ and $|\uparrow, n+1\rangle$ respectively.

3.4 Laser Cooling

Whether investigating superposition states in the qubit-motional basis or implementing two-qubit gates, experiments usually begin with an ion prepared in the ground state $|\psi(0)\rangle = |\downarrow, 0\rangle$. Particles are however initially captured with very high kinetic energy, up to $\approx 1/10$th of the trap depth, and fast reduction in the amplitude of the motion is necessary to localise and confine the ions. This is achieved through Doppler cooling on a suitable dipole transition. Photons from the laser field are rapidly scattered by the ion, and the laser frequency can be tuned such that the transition is resonant when the ion is moving towards the source to provide a damping force. Laser cooling was proposed for trapped ions by Dehmelt and Wineland in 1975 [95], and demonstrated shortly after. As a result of the bound motion in the trap a mode can be cooled from a single direction, unlike in applications with neutral atoms where counter-propagating beams are required. Additionally, if the cooling laser projects onto all three trap axes then all modes can be damped by a single laser.

The fast scattering rate required for Doppler cooling necessitates operating in the weak binding regime, where the transition linewidth $\Gamma \gg \omega_i$, the trap frequency. Here motional sidebands are unresolved, and many motional levels can be populated following decay of the excited state [92]. Doppler cooling is formalised in section 3.4.1, however the lowest motional energy obtained is still described classically. Sub-Doppler cooling is required to observe quantisation of the oscillator, one method being resolved sideband cooling on the narrow linewidth quadrupole transition in the strong binding regime, where $\Gamma \ll \omega_i$, and the motional sidebands are resolved. By tuning the quadrupole laser frequency to the red sideband the population can be driven to a lower motional state, and, as decay is predominantly on the carrier, repeating this process drives the ion to the ground state of the harmonic oscillator. The pulsed sideband cooling procedure described in section 3.4.2 is found to obtain the best approximation to the desired initial state $|\psi(0)\rangle = |\downarrow, 0\rangle$.

The motion in a Penning trap can also be cooled by a single laser beam [60], however in order to reach a sufficiently low temperature in the radial modes to enable sideband cooling, a second beam is used in ref [17]. The purpose of laser cooling is to localise the ion at the trap centre and to reduce Doppler broadening, enabling more sensitive measurement. Reduction in the kinetic energy of a mode is therefore a reasonable definition for cooling.

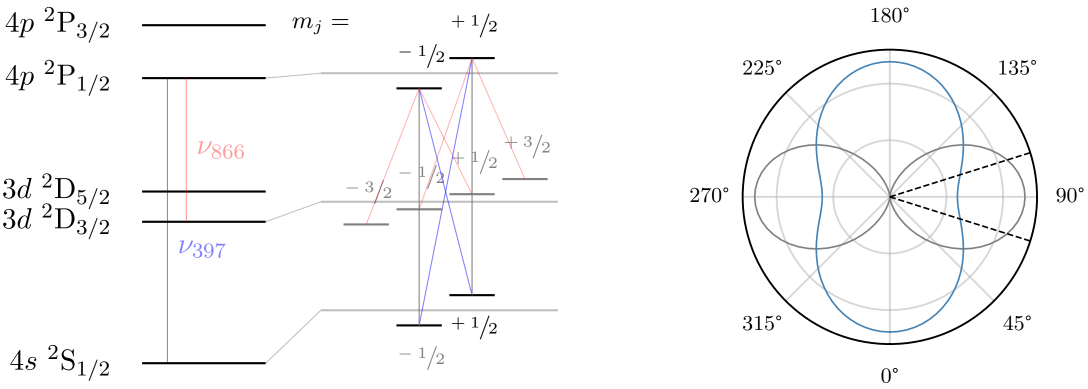

Figure 3.4.1: (Left) energy levels used in Doppler cooling. The laser at 397 nm can drive either the σ or π-transitions. Repumping all of the $D_{3/2}$ states requires σ-transitions however. (Right) spatial emission pattern for decay on π-transitions (grey) and σ-transitions (blue) [67]. Angle defined in relation to quantisation axis $\boldsymbol{z'}$, about which the emission pattern has rotational symmetry. The imaging system is perpendicular to $\boldsymbol{z'}$, with numerical aperture 0.3 shown by the dashed line.

This means that energy must be added to the magnetron mode in the Penning trap, as a red detuned laser will drive the motion to larger orbits. Before laser cooling was shown, external axialisation or rotating wall fields were used with buffer gas cooling to reduce the extent of the motion [96]. Laser cooling with an axialisation field enables Doppler cooling of the radial modes in smaller crystals and single ions. In order to lower the temperature to a regime where sideband cooling is possible, a further technique is used. The gradient of the beam profile gives an additional degree of freedom, and is positioned such that more photons are scattered when the magnetron orbit is moving away from the laser, and energy can be added to the mode. The competing requirements are analysed in detail in ref [71], but are not discussed further here.

3.4.1 Doppler Cooling

Doppler cooling is performed on the $S_{1/2} \leftrightarrow P_{1/2}$ dipole transition, with the relevant energy levels for $^{40}\mathrm{Ca}^+$ shown in fig. 3.4.1. While the Lorentzian lineshape can be obtained from a classical damped harmonic oscillator, the optical Bloch equations for a two level system solve the dynamics in terms of a density operator ρ, and can be used to obtain steady state solutions for the damping of the dipole interaction [92]. This gives the upper state population

$$\rho_{\uparrow\uparrow} = \frac{\Omega_0^2/4}{(\delta - \boldsymbol{k}\cdot\boldsymbol{v})^2 + \Omega_0^2/2 + \Gamma^2/4}, \tag{3.4.1}$$

as a function of the laser detuning δ, the interaction strength Ω_0, and the transition linewidth Γ. The lineshape is plotted in fig. 3.4.2 for a range of interaction strengths, and defines a practical definition of the coupling. Additionally the laser detuning as seen by the ion is modified by its velocity $\boldsymbol{v}$ in the direction of the laser wavevector $\boldsymbol{k}$.

During excitation of the transition, momentum $\hbar\boldsymbol{k}$ is imparted to the ion. As seen in fig. 3.4.1 spontaneous emission is approximately isotropic, resulting in no average momentum transfer over many events. A pressure force is therefore applied in the direction of the interaction laser $\boldsymbol{k}$, given by the rate of change of momentum. This will damp the motion if the laser detuning δ is negative, such that the probability of excitation is higher when the ion is counter-propagating with the laser. The scattering rate is calculated from the excited state population and decay rate, giving a force $\boldsymbol{F} = \rho_{\uparrow\uparrow}\Gamma\hbar\boldsymbol{k}$. Momentum kicks from spontaneous decay define a theoretical limit to the Doppler temperature, given as a function of laser detuning [92],

$$k_B T = \frac{\hbar\Gamma}{4}\left[\frac{1 + (2\delta/\Gamma)^2}{-2\delta/\Gamma}\right]. \tag{3.4.2}$$

The Doppler limit, $k_B T_{min} = \hbar\Gamma/2$, is obtained for detuning $\delta = -\Gamma/2$, where the laser is red detuned by half the transition linewidth, or at the maximum gradient.

Thermal Distribution

The motional state of the ion after Doppler cooling is approximated by a thermal distribution, which gives the probability of being in state n for mean occupation $\bar{n}$,

$$P(n) = \frac{\bar{n}^n}{(\bar{n}+1)^{n+1}}. \tag{3.4.3}$$

The Doppler limit can be rewritten in terms of the average motional state, $\bar{n}_{min} = \Gamma/2\omega_i$. Examples of thermal distributions were shown in fig. 3.3.1, alongside the strength of first order sidebands. To facilitate sideband cooling, the velocity must be reduced such that individual sidebands can be addressed. A further consideration is the minimum in the coupling strength of the sideband, which is at lower n for a higher Lamb–Dicke parameter. An insignificant portion of the population must lie above this point otherwise the population is trapped, and requires a more complicated procedure where higher order sidebands are addressed, which have minima at higher n.

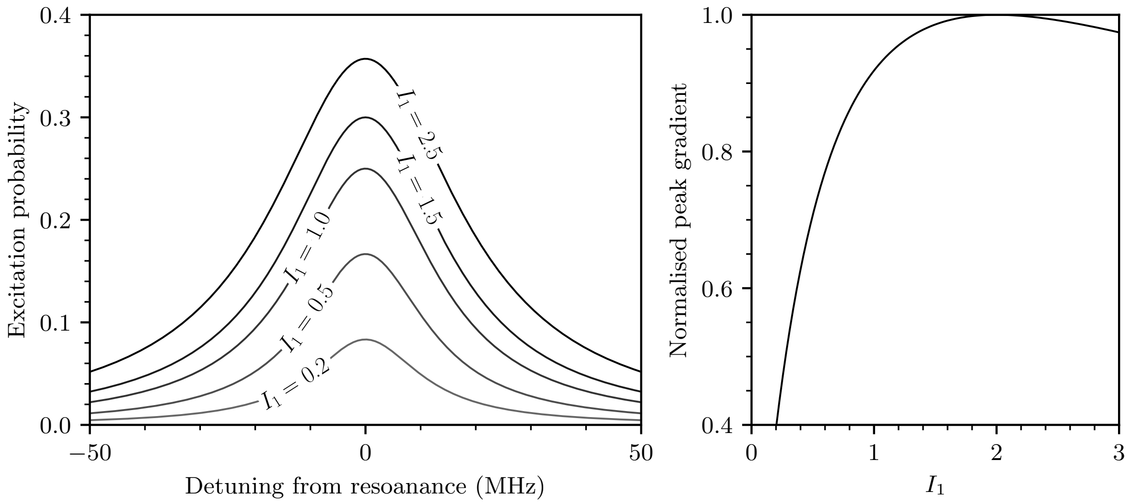

Figure 3.4.2: (Left) Lorentzian lineshape of dipole transition, with a natural linewidth $\Gamma/2\pi = 22\,\mathrm{MHz}$, shown for several values of the saturation parameter defined in eq. (3.4.4). (Right) the maximum gradient of the lineshape is shown as a function of the saturation parameter.

Line Broadening Mechanisms

The saturation intensity characterises the interaction strength Ω_0 relative to the width of the transition Γ, and is defined in ref [92] as

$$I_1 = \frac{I}{I_{sat}} = \frac{2\Omega_0^2}{\Gamma^2}. \tag{3.4.4}$$

Power broadening increases both the linewidth and the excited state population, as seen in fig. 3.4.2 (left). The cooling rate is maximised when the gradient of the lineshape is maximised, at $I_1 \approx 2$ in fig. 3.4.2 (right). However the heating due to scattering events, and therefore the Doppler limited temperature, increases with the laser power. A balance between the optimum cooling rate and final temperature is typically found at a saturation intensity $I_1 \approx 1$.

If the velocity of the ion $\boldsymbol{v}$ is assumed to follow a Gaussian distribution, then the lineshape is ultimately given by a Voigt profile, which tends to a Lorentzian as the temperature is reduced. Additionally the $\mathrm{S}_{1/2} \leftrightarrow \mathrm{P}_{1/2}$ transition is only an effective two level system if decay to the $\mathrm{D}_{3/2}$ level is returned to the cooling cycle by optical pumping, which broadens the interaction further. Another factor is the quantisation field, which separates the transitions between different sub levels through the Zeeman splitting of the states involved, giving 8 levels to consider in total. This splitting can be significant when compared to the natural transition linewidth, and affects σ-transitions to a greater extent than π. Finally,

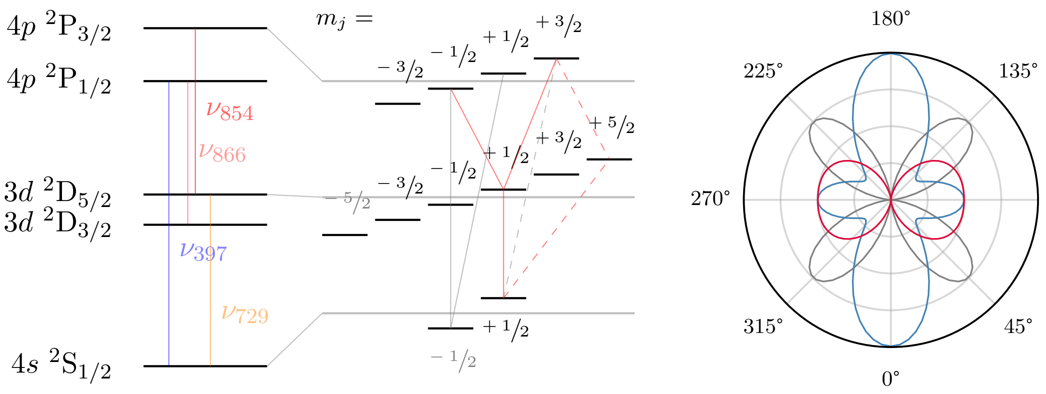

Figure 3.4.3: Low lying energy levels of $^{40}\text{Ca}^+$ with transitions addressed in sideband cooling detailed (left). Cooling on the quadrupole π-transition means that the 854nm quench pulse can excite multiple $P_{3/2}$ levels, and the ion can decay to either ground state. If the quenching drives σ_+-transition, or if the red sideband of the quadrupole δ-transition is used, the ion will decay to a single ground state with higher probability. In reality this is complicated by decay back to $D_{5/2}$ levels, and so a state preparation pulse is required. For completeness, spatial emission patterns are shown (right) for decay on π-transitions (grey), σ-transitions (blue), and δ-transitions (red) [67]. Angle defined in relation to quantisation axis ($\boldsymbol{z'}$).

excess micromotion, discussed in section 2.2.1, can significantly heat the ion, causing the broadening mechanism described in [77]. These effects are discussed further when measuring the resonance in section 4.3.5.

3.4.2 Pulsed Sideband Cooling

Motional sidebands are resolved in the strong binding regime, and consequently a narrow linewidth laser can target a specific transition. Tuning the laser to drive $|{\downarrow}, n\rangle \rightarrow |{\uparrow}, n+m\rangle$ will then add m phonons to the motional state. An iterative sequence of pulses of this form are applied to reduce the motional state to ground, as shown in fig. 3.4.4. After Doppler cooling the ion is prepared in the ground qubit state. The first red sideband ($m = -1$) is then driven to the excited state whilst reducing the motional level n by 1. The red sideband strength is determined following eq. (3.3.8), and it is therefore possible to calculate the time required to complete a π-pulse as a function of n,

$$\tau_n = \frac{\pi}{\Omega_{n,n-1}}. \tag{3.4.5}$$

As the decay time of the qubit is long by definition, the excited state is quenched by pumping back into the ground manifold via the $P_{3/2}$ level, and then into the ground state of the qubit with a state preparation pulse to leave the ion in $|{\downarrow}, n-1\rangle$. The relevant energy levels are shown in fig. 3.4.3.

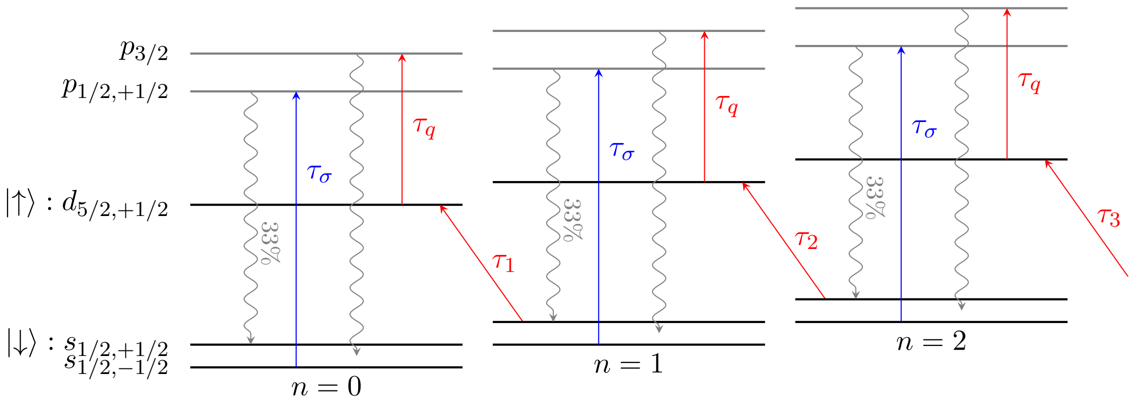

Figure 3.4.4: Sideband cooling pulse sequence from right to left. The qubit is excited by a π-pulse on the red sideband, driving the transition $|\downarrow, n\rangle \rightarrow |\uparrow, n-1\rangle$. The quench pulse, duration τ_q, returns the ion to one of the two $\mathrm{S}_{1/2}$ ground states. The σ-transition is then driven for time τ_σ to pump the population into $|\downarrow\rangle$. The motion can be excited during any of these decays, limiting the final occupation of the motional ground state.

Limits of SB cooling

For a given thermal distribution the expected population above a maximum state n_{max} can be calculated. Clearing the population below this level requires at least n_{max} pulses. For a thermal distribution characterised by $\bar{n} = 20$, the probability of finding the ion with $n_{max} > 200$ is less than 1×10^{-4}. This value is chosen to be small compared to other error contributions.

The deshelving and state preparation pulses drive dipole transitions, which are in the weak binding regime, and dominated by spontaneous decay. A range of motional states can therefore be populated when any of these transitions are driven. After sideband cooling the population is predominantly in the lowest two harmonic oscillator states, and can be characterised by a thermal distribution with $\bar{n} < 1$.

Another limitation on the average motional state is that the last π pulse does not fully excite the qubit if the coupling is not well characterised. This can be determined accurately, and the number of pulses calculated empirically. Optimisation of the quench pulses is shown in section 4.4.2, and the final temperature is obtained from spectroscopy in fig. 4.4.5.

Chapter 4

Implementation

The models developed in the previous chapter are representative of an incredibly improbable configuration of the universe, in which a two-level atom bound to a small region in space interacts with a uniform intensity monochromatic light field. Under such conditions it was shown how it is possible to prepare a trapped ion in the ground state of its motion, and to manipulate both the electronic and motional states coherently. The first step in establishing these conditions is achieved on reaching the ultra high vacuum regime, in which it becomes possible to ignore the effects of collision with background gases. The model also incorporated an idealised harmonic motion, in turn an approximation to the effect of the rf potential. The frequency of laser emission must also be stabilised so that the required dynamics can be achieved. In order to scan parameters, laser fields require a varying degree of control over intensity, frequency, and phase. Experiments on the ion enable fine tuning of both trapping and magnetic fields, such that they deviate minimally from the theoretical description.

In characterising the Paul trap it is first necessary to describe the requisite control systems. These are broadly categorised as optical systems, section 4.1, and experimental control, section 4.2. Optical systems transform the raw emission of continuous wave lasers into the controllable interaction required. The imaging system collects fluorescence emitted by the ion, allowing state detection in addition to diagnostics. Sophisticated experimental control infrastructure is required for the coordination of a large number of inputs and outputs on a fast time scale, and this section describes how an experiment is built up from the numerous interactions.

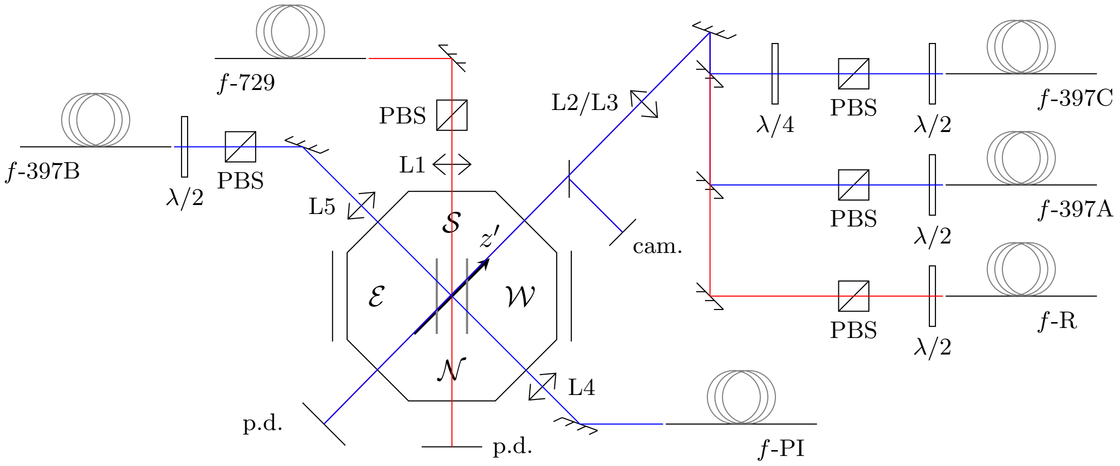

Figure 4.1.1: Interaction geometry between lasers, trap, and the quantisation axis of the ion (z'). Shown from the point of view of the imaging system, with the trap z axis aligned to north-south, the rf feedthrough east, and the pumps and pressure gauge west. Sources of the emission for Doppler cooling lasers: Red 854 and 866, and 397, are detailed in fig. 4.1.2, photo-ionisation (PI) lasers in fig. 4.3.1, and the spectroscopy 729 laser in fig. 4.1.3. Laser polarisations and beam sizes at the ion are detailed in table 4.1.1, and are imposed after the fibre emission by polarising beam splitters (PBS), waveplates, and lenses (L1-5). Beams are monitored with photodiodes connected to the control system, and the trap centre imaged with a camera.

Characterisation of the trap in section 4.3 outlines useful techniques for measuring and optimising experimental parameters. The stability of these parameters can vary to a large extent, and therefore differ in how often they need to be optimised. It is then finally possible to examine the optical qubit in section 4.4. Evolution of the electronic state under continuous driving is shown, and characterised by the previously developed models. Spectroscopy on the quadrupole transition is used to determine the temperature of the ion after both Doppler and sideband cooling, and shows the ion can be prepared in the state $|{\downarrow}, 0\rangle$ with high probability.

4.1 Optical Systems

The interaction geometry between lasers, trap, and the quantisation axis of the ion is illustrated schematically in fig. 4.1.1. The Doppler cooling beams project onto all axes of the motion, whereas the quadrupole laser projects only onto the axial mode. The beams are fibre coupled to clean their profile, reducing scattering through the trap and ensuring constant intensity across the extent of the ion. The laser systems preceding the fibres are detailed in sections 4.1.1 and 4.1.2, and are designed to facilitate fast experimental and slower diagnostic requirements. Acousto-optic modulators (AOMs) enable effectively instantaneous changes in laser power, including switching, a limited range of frequency,

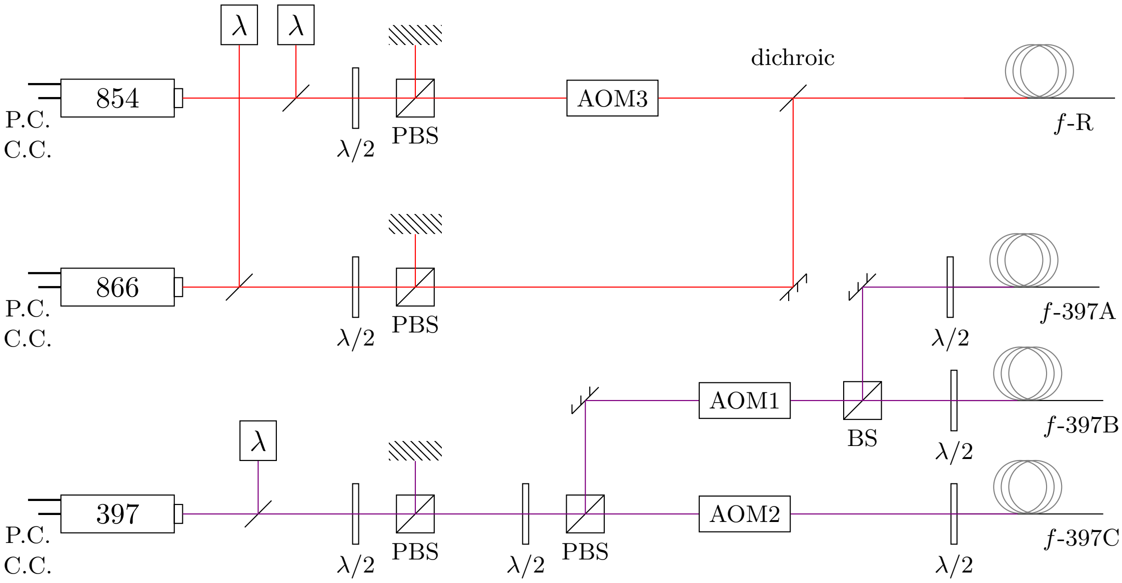

Figure 4.1.2: Laser optical systems used to address dipole transitions, with part numbers in table A.1. The laser emission frequency is determined by the current (C.C.) and piezo (P.C.) controllers. Diagnostics monitor the laser frequency with a wavemeter λ. Two linearly polarised Doppler cooling beams at 397 nm are controlled by acousto-optic modulator AOM1, and the circularly polarised state preparation via AOM2. The 854 nm laser is controlled by AOM3, and is combined with the 866 nm laser on a dichroic mirror.

and relative phase. Slower control of laser frequencies is possible through feedback to the laser current and voltage supplies, with far greater range. Similarly for imaging, section 4.1.3, an electron multiplying (EMCCD) camera is used to determine the presence of the required number of well Doppler cooled ions, but for faster experimental state detection a photo-multiplier tube (PMT) is used.

4.1.1 Dipole Lasers

External cavity diode lasers (ECDLs) address dipole transitions. The emission frequencies are set through the current provided to the diode (C.C.) and the voltage applied to the

Beam	Transitions	$\phi(°)$	$\gamma(°)$	Spot size (μm)
397A	σ	0	any	70
397B	π	90	0	
397C	σ_+ / σ_-	0	-	
R.866	σ	0	any	
R.854	σ	0	any	
729	π , δ	45	0	

Table 4.1.1: Laser field polarisations and the transitions driven, where π, σ, and δ indicate a change in the magnetic number $|\Delta m_j| = 0, 1,$ and 2 respectively, and the subscript ± indicates the sign. This is informed by selection rules, the energy level structure of fig. 3.1.1, and the interaction geometry in figs. 3.2.2 and 3.2.3. The 397 laser is split into three components whose functions are discussed in section 4.1.1.

piezo (P.C.), which changes the external cavity length. The wavelength meter monitors laser frequencies, which can be stabilised at the desired position with a dedicated program feeding back to the piezo voltage of each laser controller. This is described in section 4.2.2. This restricts the laser linewidths at 1-2 MHz on the timescale of experiments, which is significantly lower than the width of dipole transitions. As the tuning range of AOMs 1-3 is also smaller compared with the transition linewidth, the program is required to scan laser frequencies over the full extent of the transition. The laser power requirements discussed in section 3.4 are set using half waveplate and polarising beam splitter combinations, and AOMs are used to turn the interaction off and on, with different powers during Doppler cooling and measurement.

Optical systems are detailed in fig. 4.1.2. The transition at 397 nm can be addressed by either of two linearly polarised beams, A and B, which drive σ and π transitions respectively. Broadening of the lineshape with magnetic field is minimised for coupling to π transitions, and therefore achieves a lower Doppler temperature. However both angles enable compensation of the micromotion in section 4.3.4. The circularly polarised beam C is used in state preparation, and must be aligned with the quantisation axis. This is discussed in section 4.4.2. The Doppler cooling cycle is closed by repumping at 866 nm, which necessitates driving the σ-transitions. The 854 nm transition is addressed to deshelve the excited qubit state after sideband cooling pulses and state readout. This has the same geometrical considerations as the 866, however the laser must be extinguished during qubit manipulation. The ability to turn off the 866 would offer limited experimental advantage here, as it does not couple to the qubit, and is not detected by the imaging system.

The lasers controlled by AOMs must be switched off at certain times in the experimental sequence. AOMs are arranged in a double pass configuration, and suppress the laser power by a factor of 10^4. Any residual leakage will ultimately manifest as qubit errors. The rise time of AOMs can be found in the references of table A.1, but are insignificant on the time scale of experimental pulses. During state detection the requirements of Doppler cooling can be relaxed, and more photons are counted in a given period by increasing the power or by tuning the laser closer to resonance.

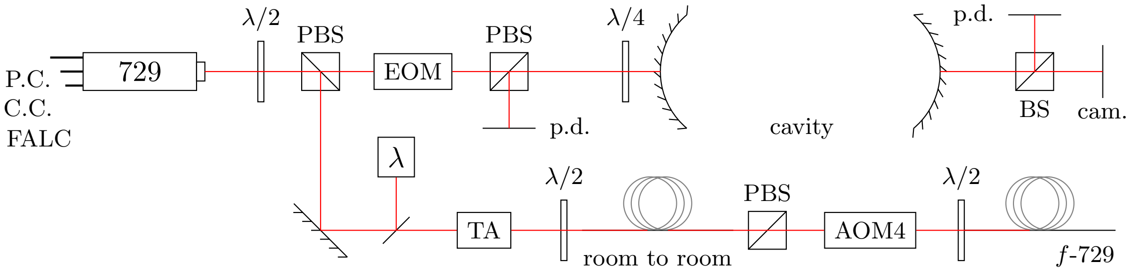

Figure 4.1.3: Spectroscopy laser optical schematic. A locking signal is picked-off by the first polarising beam splitter (PBS). The electro-optic modulator (EOM) adds sidebands at 25 MHz, and the modulated light is transmitted through the second PBS. The reflection from the cavity passes through the quarter waveplate twice, and the rotated polarisation is refelcted onto the photodiode (p.d.). The cavity transmission is monitored by a camera, to see which cavity mode is coupled to, and a photodiode. The absolute frequency is determined using the wavemeter. The main beam is amplified with a tapered amplifier (TA) and coupled to a 5 m optical fibre between rooms, which is insulated from vibration.

4.1.2 Quadrupole Laser

The qubit interaction model assumed an infinitely narrow linewidth transition between the two levels of the atom. In reality the transition linewidth is dependent on magnetic field noise, through the induced Zeeman splitting, and the linewidth of the laser on the timescale of interactions. This will determine the coherence time of the system, a concept which will be developed in chapter 5. The optical system outlined in fig. 4.1.3 has evolved over many years. The cavity system, held under vacuum for thermal stability, is discussed in ref [68], whereas the ECDL, locking electronics, and full characterisation of the laser can be found in ref [97].

The emission is stabilised by locking to the cavity with the Pound-Drever-Hall (PDH) technique [98]. Transmission through the initial polarising beam splitter is phase modulated by an electro-optic modulator (EOM) which produces sidebands at the drive frequency, and with opposite phase. When the laser is matched to a cavity mode, the carrier is reflected in phase with the incoming beam, whereas the sidebands, which are far from the cavity resonance, are reflected with minimal phase shift. Any drift of the carrier away from resonance will induce a phase shift in the reflection, and therefore produce two beat notes with the sidebands. The signal from the photo-diode is mixed with the modulation frequency, and sinusoidal terms filtered, in order to recover an error signal. This signal gives an indication of the laser linewidth, and is shown in fig. 4.1.4.

The quadrupole laser requires greater power than dipole lasers, on the order of 10 mW, and this is provided by the tapered amplifier (TA). The two stages of fibre coupling after

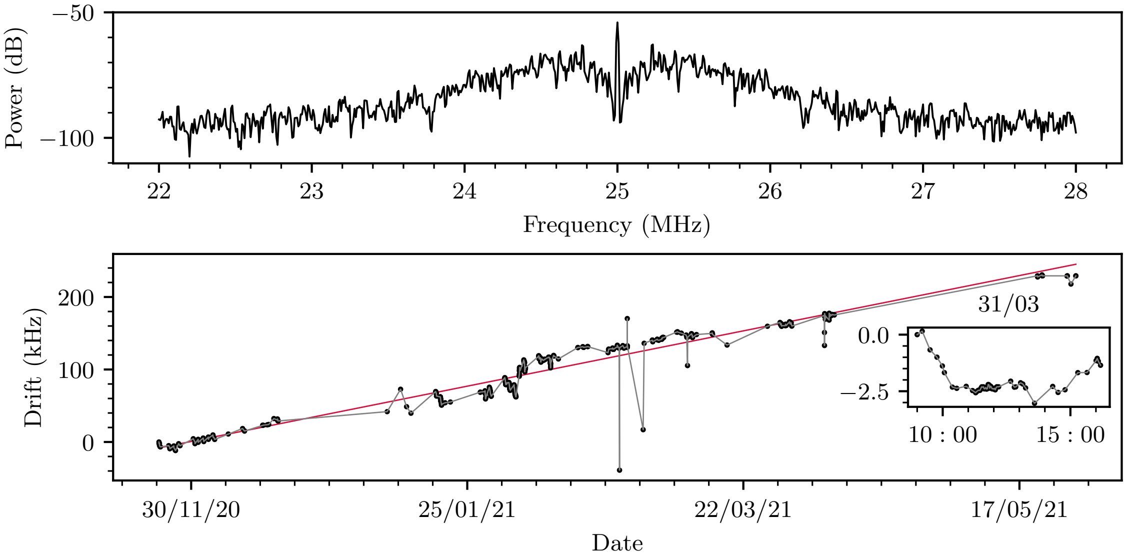

Figure 4.1.4: Power spectral density of laser locking signal (top) with characteristic servo-bumps around 400 kHz of the central feature. Long term drift[i] of quadrupole carrier transition (bottom) is measured at 1.36 kHz per day. A previous measurement in the Penning trap [99] gave a rate of 1.45 kHz per day, attributed to creep in both the cavity length and the superconducting magnet. As the magnetic field drift is small in this trap, see section 4.3.3, this measurement appears consistent. Further, the short term drift is correlated with the room temperature, see inset, with the frequency dropping as the room heats before a period of stability.

this add noise, typically in the polarisation, which is converted into power noise with a polarising beam splitter. The power at the ion is monitored by the photo-diode shown in fig. 4.1.1, and does not require active stabilisation. Of greater concern is the observed drift in the carrier transition of the atomic resonance, which is plotted in fig. 4.1.4 (bottom). The average drift rate of 1.36 kHz per day is due to long term drift in the cavity length, however despite its isolation from the environment the cavity is sensitive to the room temperature, and larger fluctuations are observed throughout the day.

Control over the frequency of the laser at the ion is possible through AOM4, with a tuning range in the first order diffracted beam of ±50 MHz. The rf signal is synthesised by the control system, and it is therefore possible to set the amount of phase added to the laser field at the start of a pulse. Multiple frequency components can be induced in the laser field by mixing two rf outputs of the control system. This enables the driving of multiple sidebands simultaneously, with control over the power of each interaction. Universal control of the laser field is possible as the AOM can be driven by an arbitrary waveform generator (AWG), enabling any frequency and temporal variation.

---

[i] Carrier calibration routine and logging set up by CSL. Also used in figs. 4.3.3 and 4.3.4.

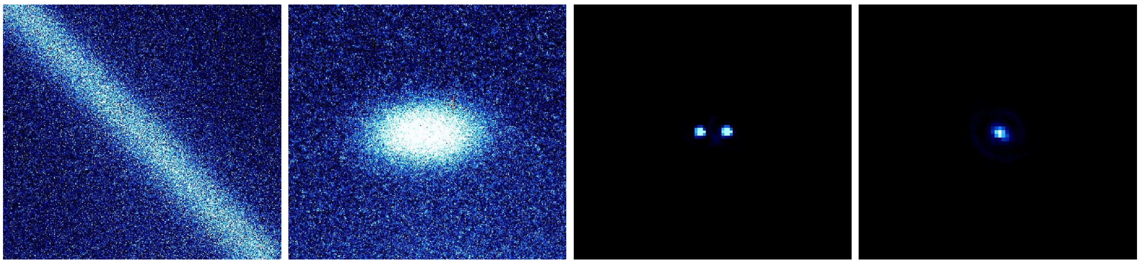

Figure 4.1.5: EMCCD images in the rf trap. From left to right showing the fluorescence of neutral calcium along the beam path of the 423 nm laser; the first cloud of ions seen in the trap; a linear chain of two ions; and a single ion.

4.1.3 Imaging System

The imaging system must direct a sufficient portion of the fluorescence emitted by an ion to either a PMT or EMCCD camera, culminating in the compact design outlined in ref [100]. The camera pixel size is 16 µm, and therefore to resolve ions separated by only a few µm the system must image the trap centre with sufficient magnification. Images taken with the camera are seen in fig. 4.1.5 showing fluorescence from the photo-ionisation lasers, a small cloud of ions, two ions, and a single ion. For experiments with a single ion however, there is no advantage to using the camera for state detection as the ion is either bright or dark. Fluorescence measurements are therefore made using the PMT, which is easier to interface and has a faster readout rate.

The critical quantity is the number of photons that can be counted in a given collection period. Under continuous Doppler cooling the photon emission of the ion can be assumed isotropic, and the collectable solid angle is restricted by the top recessed viewport to 1 sr. In practice this is limited by the collected angle of the imaging system at 22.85°, giving a collection efficieny $\eta_c = 0.04$ [100]. The viewport has only one anti-reflection coated surface, and therefore a transmission efficiency of $\eta_v = 0.96$ A notch filter blocks all but light in the range of $377 - 424$ nm with transmission efficiency $\eta_f = 0.95$, enabling detection of Doppler and photo-ionisation fluorescence whilst limiting background scatter. The imaging lens is an achromatic doublet, with $\eta_d = 0.95^3$. There are also two coated lenses, which lead to losses given by $\eta_l = 0.99^4$. Finally the quantum efficiency of the PMT limits the number of counts, $\eta_q = 0.2$, giving a total efficiency, $\eta_{tot} \approx 0.5\%$. This implies a collection rate of $\eta_{tot}\Gamma_{397}/2 \approx 5 \times 10^5$ photons s^{-1}. This is determined experimentally at $\approx 5 \times 10^4$ photons s^{-1}, with the resolution of bright and dark distributions discussed further in section 4.4.1.

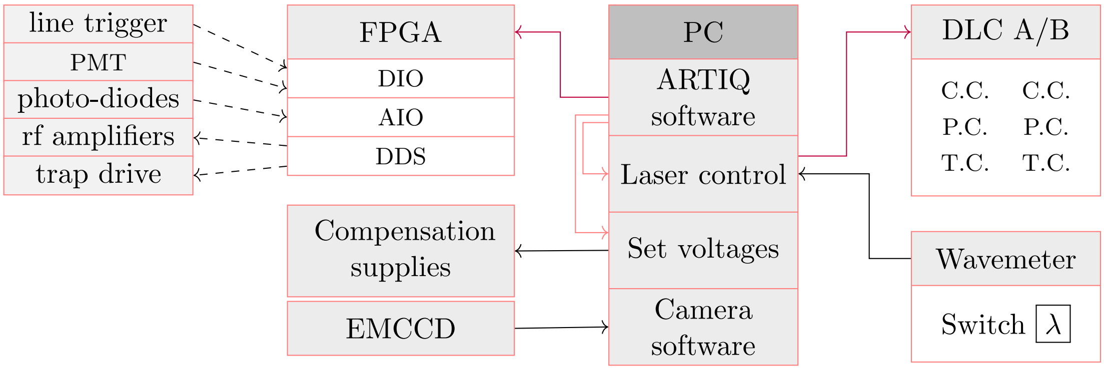

Figure 4.2.1: Experiments run on the main PC. ARTIQ software controls the FPGA which coordinates digital and analogue inputs and outputs (DIO/AIO), and rf voltages (DDS). The ARTIQ software also communicates with laser control and dc voltage power supplies, shown by the red arrows. Connections over the local network are shown in purple, devices connected by USB in black, and coaxial cables dashed. Inputs to the optical switch, λ, are shown in optical system figures.

4.2 Experimental Control

A typical experimental sequence includes stages of cooling, state preparation, coherent manipulation, and measurement. As measurement of the qubit state is probabilistic, a single data point is derived from multiple shots, and a trace is obtained by taking data over a range in the control parameter. The control system must therefore loop over the specified number of shots at each value of the control parameter with timing resolution greater than required interaction times. For example, to construct a trace of qubit excitation as a function of interaction time, the length of the spectroscopy pulse is incrementally increased, with 100 shots at each point in time giving good statistics for estimation of the excitation probability.

An overview of the experimental control system is shown in fig. 4.2.1. The experimental PC runs dedicated ARTIQ (advanced real-time infrastructure for quantum information experiments) control software. This can program an FPGA, discussed in section 4.2.1, for nanosecond timing precision during each data shot. Additionally, the ARTIQ software can control other programs running on the experimental PC, including control of the laser frequencies through feedback to the laser controller over the experimental network, discussed in section 4.2.2, and dc voltage supplies connected via USB.

4.2.1 ARTIQ

A new control system has been developed for this project, and uses the ARTIQ software developed by the ion trapping group at NIST with M-Labs. This has been adopted by a growing number of atomic physics groups as experiments increasingly require coordination of multiple signals and more complicated control fields. The software includes libraries for describing experiments, and time-critical code is compiled and run on customised hardware. The modular nature of the system allows new sub-systems to be easily incorporated. Additionally it provides a graphical user interface for scheduling experiments, monitoring diagnostics, the storage of parameters and results, and live data visualisation.

The hardware detailed in table A.1 is developed at the University of Warsaw and manufactured by Sinara. The FPGA is connected to the main experimental computer via ethernet, limiting the speed with which it can be programmed to the order of 1 s. Code running on the FPGA can coordinate the fast timing of inputs and outputs on up to 12 connected modules with a clock speed of 125 kHz. These include digital inputs, for the line trigger and PMTs, and analogue inputs for monitoring photo-diodes. The DDS boards synthesise rf frequencies, with precise control over amplitude, frequency, and phase. These rf signals are amplified and used to drive AOMs and the trapping field.

It is illustrative to consider the requirements of a single shot, taking the example of sideband cooling followed by manipulation of the electronic state shown in table 4.2.1. To minimise fluctuations in the magnetic field over the mains cycle, experiments are started by a line trigger, which limits the speed at which single shots can be taken to 50 Hz. In this time the ion is first monitored over a period of Doppler cooling for ≈ 5 ms, followed by a stage of optical pumping into the desired ground state. The sideband cooling sequence consistst of a series of variable length red sideband pulses, defined in eq. (3.4.5), followed by deshelving and state preparation. The ground state cooled ion can then be manipulated by the probe, which is immediately followed by a period of photon counting.

					×200			
	Wait	T_{DC}	T_{OP}	τ_n	T_{DS}	T_{SP}	Probe	T_C
LT	▨							
rf.397A	▨	▨						▨
rf.397C			▨			▨		
rf.854	▨	▨	▨		▨	▨		▨
rf.729				▨			▨	
PMT		▨						▨

Table 4.2.1: Control sequence for a single data shot. After the experiment is triggered (LT), the ion is Doppler cooled (DC) and then optically pumped (OP) into the ground state. The pulsed sideband cooling sequence (between double lines) consists red sideband pulses, deshelving (DS), and state preparation (SP). Following this the state of the ion can be probed and measured by photon counting (C).

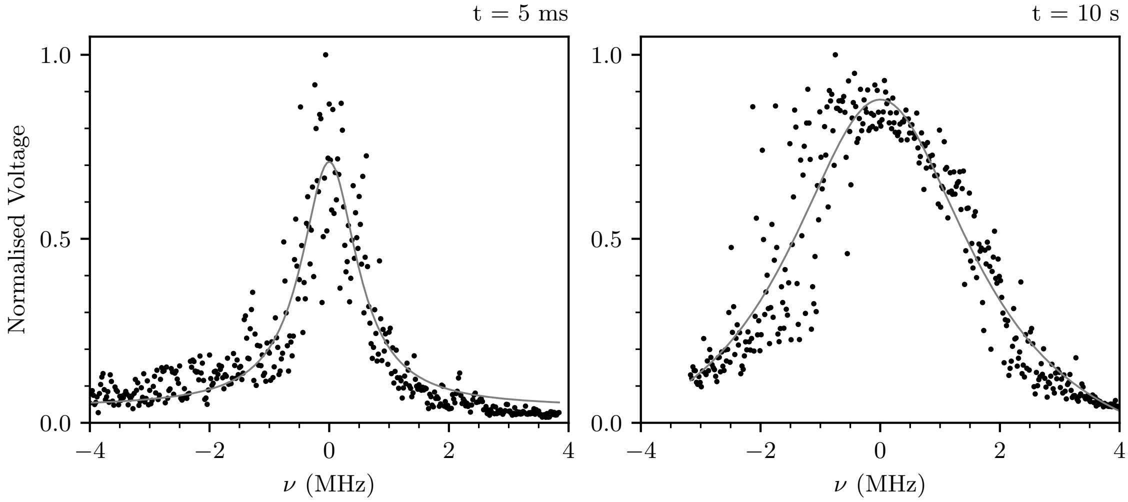

Figure 4.2.2: Beat note measurement between two different blue lasers locked to the same point with the wavemeter software. The signal is measured by a photo-diode, with voltages obtained from a spectrum analyser. For the two timescales shown the signal has a linewidth of 1.0(3) MHz over 5 ms and 3.7(1) MHz in 10 s. The errors represent one standard deviation in 100 and 10 measurements respectively.

4.2.2 Wavemeter Laser Lock

Stabilisation of laser frequencies is hugely simplified by modern laser controllers, which are connected to the local network. Laser frequencies are monitored by a wavemeter with a relative stability better than 1 MHz. A dedicated program modifies the voltage applied to the piezo in order to stabilise these frequencies. As the optical switch cycles through the multiple channels, the sampling rate of the wavemeter limits the frequency with which the error signal can be updated. The five monitored lasers require an exposure time of a few ms, with a 20 ms delay between each channel to limit optical leakage. This gives a sampling rate for each laser in the region of 10 Hz, and the performance of the lock is shown by a beat note measurement in fig. 4.2.2.

The set point of each lock can be modified by experimental scripts, allowing resonance scans of the Doppler transition lines, which enables optimisation of laser frequencies. The wavemeter is subject to a repeatable drift throughout the day, and is calibrated to a helium neon laser (HeNe), described in detail in ref [68]. The software enables this calibration, and it can therefore be automated. This does not account for drift or sudden changes in the HeNe frequency, which may necessitate recalibration of the transition frequencies.

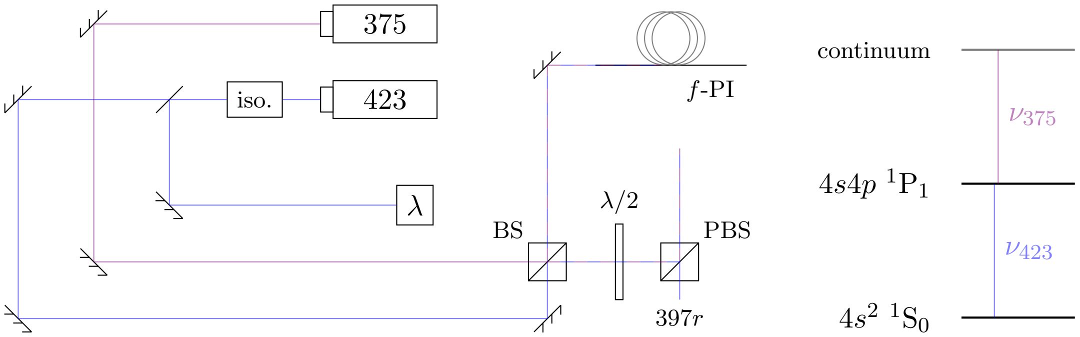

Figure 4.3.1: Photoionisation laser schematic (left) and addressed neutral ^{40}Ca energy levels (right). Diode lasers components are detailed in table A.1, and only the 423 laser is grating stabilised. The optical isolator (iso.) protects the diode from back reflected light. The combined beams are coupled to a fibre and sent to the rf trap. Another path combines the PI beams with the 397 radial beam of the Penning trap, which couple to orthogonal fibre modes. [$\nu_{423} = 709.078\,24$ THz; $\nu_{375} > 770$ THz].

4.3 Paul Trap Characterisation

In this section properties of the trap and basic interactions with a single ion are characterised. This begins with photo-ionisation in section 4.3.1, where a single ion can be loaded and monitored under continuous Doppler cooling. The following sections outline the procedures which are used to tune trap parameters in order to maximise the quality of the optical qubit. This first involves calibration of the trapping frequencies with applied voltages in section 4.3.2, and the splitting of transitions with magnetic field in section 4.3.3. The magnetic field direction is optimised by minimisation of the signal from the circularly polarised 397C, and the compensation of the electric fields is discussed in section 4.3.4. Doppler cooling transition resonances are shown in section 4.3.5, which enables optimisation of powers and frequencies, and the length of the period T_{DC}.

4.3.1 Ionisation

Several schemes exist for the ionisation of neutral calcium. Bombardment with high energy laser pulses, from say a doubled Nd:YAG, can liberate a single electron via a three photon process, or an electron gun can knock an electron free. These processes will however indiscriminately ionise anything in their path. A more selective method involves exciting an electron to the $^1P_1$ state on the dipole transition shown in fig. 4.3.1 (right). The electron can subsequently be excited to the continuum by photons with frequency greater than 770 THz. Further, this process is shown to be isotope selective from the resonance measurement in fig. 4.3.2, where it can be seen that the observed linewidth of the resonance is much narrower than the isotope shift. The configuration of the optical system used in

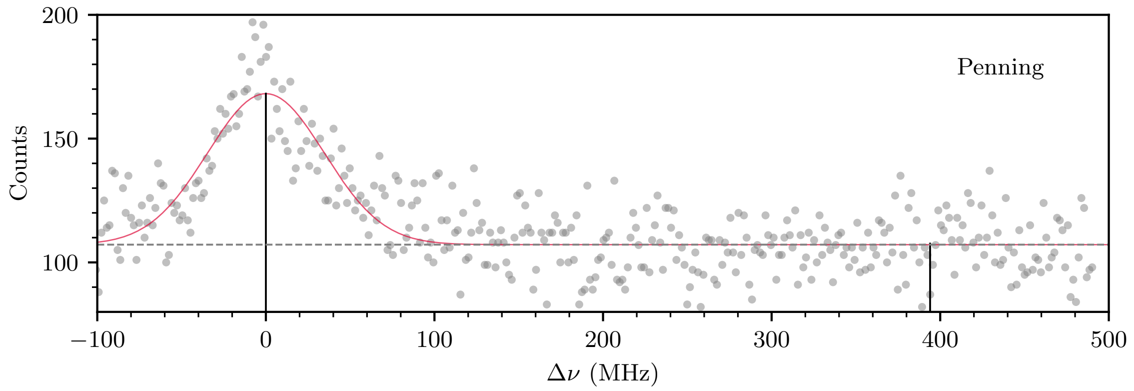

Figure 4.3.2: 423 nm resonance spectrum in the Penning trap. In the magnetic field of the Penning trap the π transition remains at the unshifted resonance, and the polarisation angle γ is important. The natural linewidth of the $S_0 \leftrightarrow P_1$ transition is approximately 35 MHz. The resonance, with FWHM $\approx$ 80 MHz from the Gaussian fit (red) is therefore dominated by Doppler broadening, as the laser linewidth is less than 10 MHz. The frequency shift of the next stable isotope ^{42}Ca is indicated at $\Delta\nu$ = 394 MHz. The natural abundance, present in ovens, is 97% ^{40}Ca. Neutral fluorescence in the rf trap is seen in fig. 4.1.5.

photo-ionisation (PI) is detailed in fig. 4.3.1 (left).

The rf trap uses an oven design [101] which was shown in fig. 2.2.6. This minimises excess deposition of calcium on the electrodes, which can cause heating and shift the location of field minima. The highly directional output also limits Doppler broadening of the neutral resonance with the 423 nm laser, which propagates perpendicular to the atomic flux. This defines a geometric factor for the interaction of $\phi \approx 90°$, and horizontal (vertical) linear polarisation will therefore drive π (σ) transitions to the $^1P_1$ energy level. In the weak quantisation field of the rf trap the splitting of these states is small however in comparison with the transition linewidth, and any linear polarisation can be used.

4.3.2 Trap Fields

The axial and radial trap frequencies are measured as a function of applied dc voltage or rf amplitude in fig. 4.3.3. The axial trap frequency is determined from frequency spectroscopy on the ion, outlined in section 4.4.4, and is accurate at the sub kHz level. With no projection of the 729 laser along the two directions of radial motion, the frequencies are measured by application of an rf 'tickle' voltage to compensation electrode C_x. When the frequency of this voltage is resonant with the ions' motion in the radial direction, vibrational excitation is seen on the imaging camera. This method cannot resolve the two radial modes, which are distinct due to deviation in the field from the idealised model, but is sufficient to characterise the motion.

There are two competing requirements on the radial confinement: Doppler cooling achieves

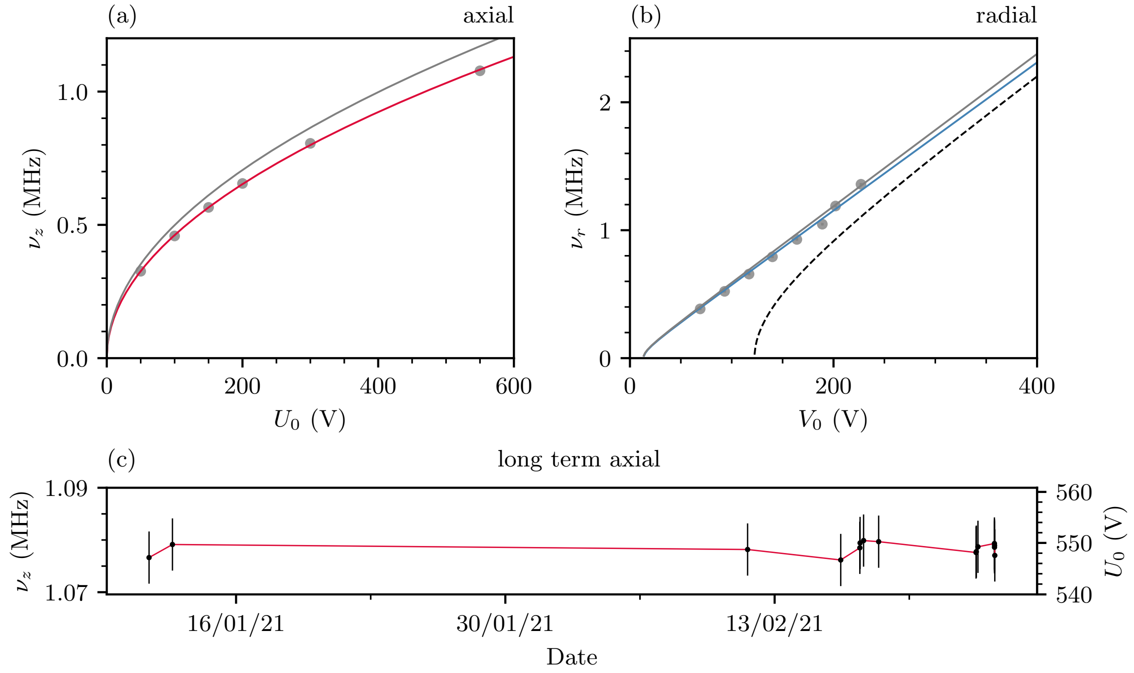

Figure 4.3.3: (a) Axial trap frequency ν_z as a function of applied endcap potential U_0. Measurement (data, red fitted line) gives $\kappa_z = 0.132$, whereas the behaviour predicted by simulation (grey) implied $\bar{\kappa}_z = 0.155$. (b) Radial frequencies at axial frequency $\nu_z = 156\,\text{kHz}$. Fitting to the measurement (data, blue fitted line) gives $\kappa_r = 0.97$, however due to the difficulty in measuring V_0 this cannot be distinguished from 1. The radial simulation (grey) gave $\bar{\kappa}_x = 0.95$ and $\bar{\kappa}_y = 0.92$. The black dahsed line shows the scaling of the radial frequency at $\nu_z = 1\,\text{MHz}$. (c) Long term axial trap frequency stability. No drift is observed at this resolution, and measurements on the qubit in chapter 5 give more insight into the shorter term stability.

a lower average motional state at higher trap frequency, which motivates maximising the rf voltage, however for a fixed drive frequency Ω, defined in eq. (2.2.7), increasing the rf voltage V_0 increases the stability parameter q_u, making radial confinement less stable. From fig. 2.2.2, for $\Omega/(2\pi) = 10\,\text{MHz}$, the stability threshold of 0.4 is reached at 350 V, and a radial frequency of 2 MHz. At higher axial frequencies the radial frequency can be significantly reduced by the deconfining axial field following eq. (2.2.10), which can be rewritten

$$\omega_u = \sqrt{\bar{\omega}_u^2 - \frac{1}{2}\omega_z^2}, \qquad \bar{\omega}_u = \frac{\Omega q_u}{2\sqrt{2}}. \tag{4.3.1}$$

The black dashed line in fig. 4.3.3 (b) shows the expected radial frequency scaling at $\nu_z = 1\,\text{MHz}$, where the highest stable radial frequency is reduced to 1.8 MHz.

The long term stability of the axial trapping frequency for a fixed voltage U_0 is measured over several months in fig. 4.3.3. This measurement is made by calculating the frequency difference between first order motional sidebands, and shows no long term drift of the trap frequency due to the power supply or changing properties of the field.

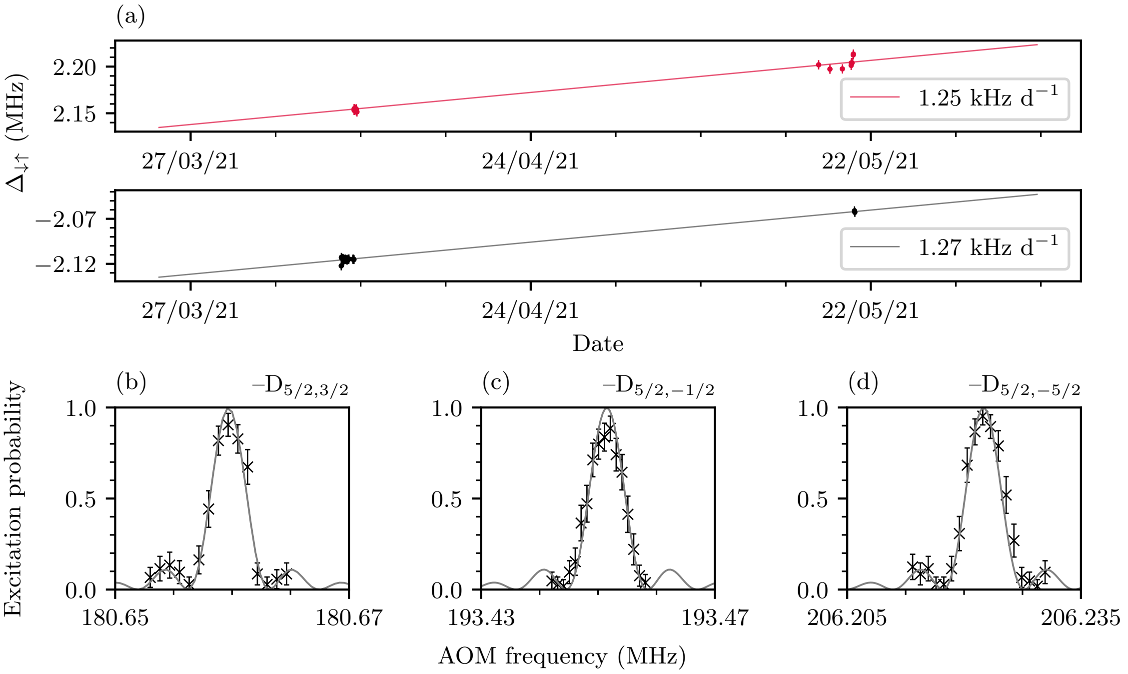

Figure 4.3.4: (a) Long term magnetic field strength from measurement of the two quadrupole π transitions. Shown relative to the unshifted AOM frequency $\Delta_{\downarrow\uparrow} = 195.504\,\mathrm{MHz}$. The difference in the linear drift of the transitions is less than 25 Hz per day, corresponding to a change in the magnetic field of 2 nT, and change in coil current of less than 10 µA. (b-d) Spectra of quadrupole transitions from the ground state $\mathrm{S}_{1/2,-1/2}$ as a function of the AOM frequency. This implies a magnetic field of 0.38 mT for an applied main coil current of 1.3 A. The AOM is configured to take the -1st order, and reduces the laser frequency, hence the inverted sign from fig. 3.2.4.

4.3.3 Quantisation Field

In the configuration of the quadrupole interaction shown in fig. 4.1.1, the two π-transitions are strongly driven, with distant δ-transitions driven more weakly, as seen in black in fig. 3.2.4. Drift in the quantisation field is seen by repeated measurement of the two π-transitions in fig. 4.3.4 (a). The magnitude of the quantisation field is proportional to the frequency difference between the transitions through their Zeeman splitting. A linear drift in the transition difference of 25 Hz per day is small compared to the observed frequency drift of the spectroscopy laser, seen here and in fig. 4.1.4. This corresponds to a drift in the magnetic field strength of 2 nT per day. Shorter term stability of the magnetic field is determined through experiments on the optical qubit in chapter 5.

The ion is initialised in a specific ground state by optical pumping, and with no coupling to radial modes, and most optical transitions suppressed by the interaction geometry, many sources of off-resonant excitation are eliminated. From the $\mathrm{S}_{1/2,-1/2}$ ground state three transitions can be driven, and are shown in fig. 4.3.4 (b-d). This enables calibration of the quantisation field strength at $0.29\,\mathrm{mT\,A^{-1}}$ applied to the main coil.

4.3.4 Micromotion Compensation

The rf field applied to radial electrodes produces a three-dimensional minimum in an effective trapping field. This is strongly confining in the radial dimensions, and only very weakly in the axial. The centre of the static dc potential must be aligned with this null point in all dimensions using compensation electrodes to eliminate excess micromotion. Excess micromotion broadens the Doppler transition linewidth, as seen in fig. 4.3.6, which enables coarse compensation in the direction of the Doppler cooling laser. Excess micromotion also leads to modulation of the qubit carrier transition, giving rise to sidebands at the trap drive in the frequency spectrum. This is a more sensitive method of probing the micromotion, and therefore field misalignment, as a function of the compensation voltages. However in the configuration shown in fig. 4.1.1 the spectroscopy laser projects onto the axial mode, and therefore has limited sensitivity to the radial micromotion.

The radial field is compensated with the cross correlation technique [77]. In the reference frame of the ion, the frequency of the cooling laser is Doppler shifted at the micromotion frequency Ω. The observed fluorescence signal therefore fluctuates, over the period of the rf drive, as the laser detuning effectively moves across the transition line. The variation in scattering rate is dependent on the amplitude of the micromotion in the direction of the laser wavevector. Consequently a single beam can only minimise micromotion in a single direction. With a second beam in the horizontal plane, as shown in fig. 4.1.1, it is possible to minimise all but vertical micromotion. Residual vertical micromotion is less concerning as all interactions are in the horizontal plane.

The control system has a clock speed of $\approx 12 \times \Omega$, and it is therefore possible to bin photons by their arrival time relative to the drive. This is seen in fig. 4.3.5 in the case that the ion is (a) poorly and (b) well compensated. Each 397 laser will then see minima in the standard deviation of this signal at a particular value of the vertical compensation voltage V_y, shown in (c). The combination of radial voltages that minimises micromotion for both beams can then be determined in (d), giving the point at which there is no micromotion in the horizontal plane. The axial micromotion is then minimised by measurement of the rf sideband strength as a function of the axial differential voltage V_z in (e). This process can be iterated in an attempt to reduce all excess micromotion, however as all lasers are in the horizontal plane this is not completely possible.

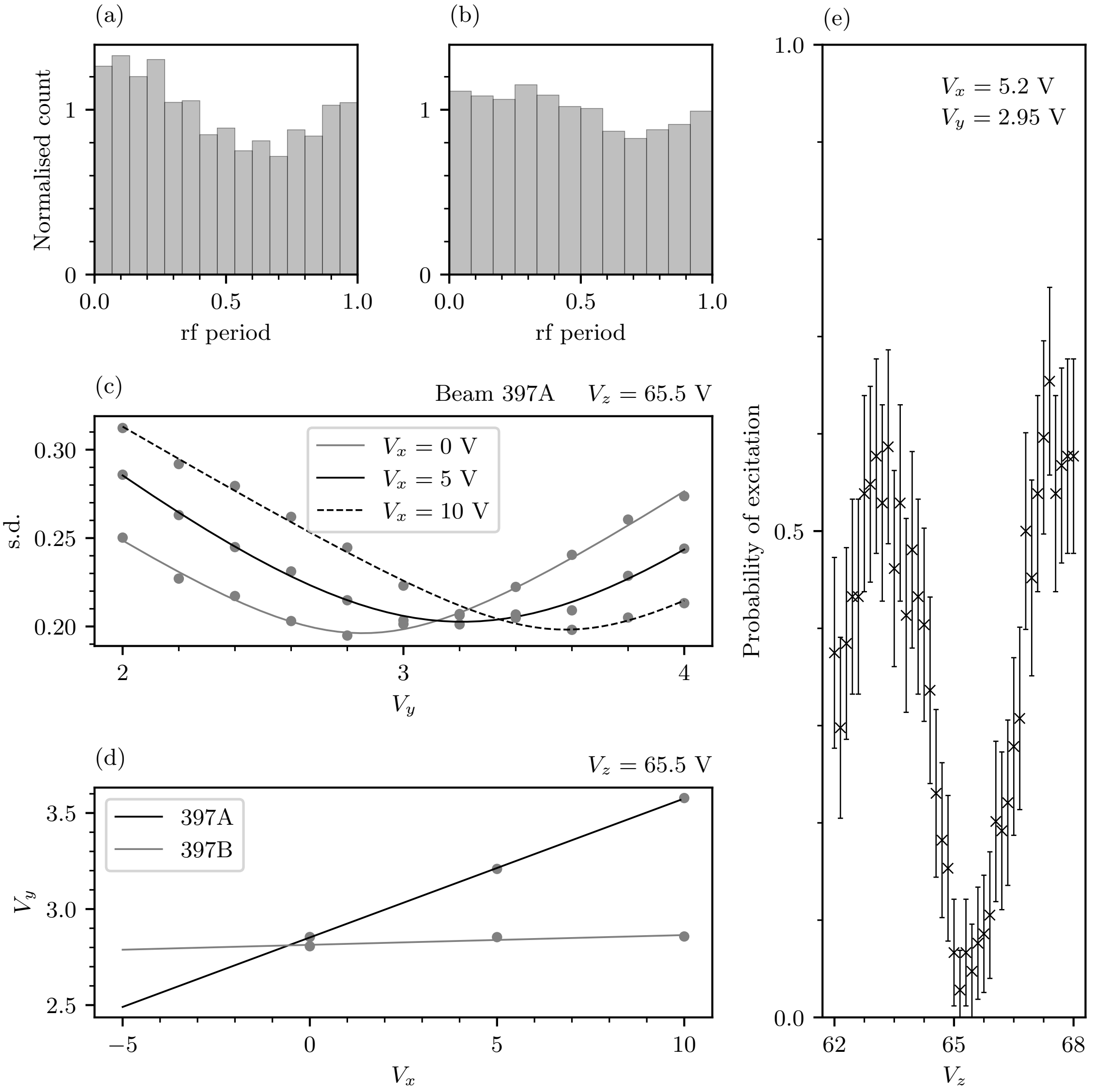

Figure 4.3.5: Micromotion compensation techniques. Normalised photon counts, binned by their arrival time relative to the rf period for (a) a poorly and (b) a well compensated ion in the direction of one laser. (c) Standard deviation of bins as a function of vertical compensation voltage V_y, where minima imply the minimal projection of micromotion in the direction of the laser, $397A$. These minima are dependent on other compensation voltages as well as the projection of the micromotion onto the laser. (d) standard deviation minima are shown in two dimensions for two interrogation directions in the radial plane. This leaves vertical micromotion undetectable, caused by a horizontal offset of the rf and dc fields. (e) Excess micromotion in the axial direction is determined by monitoring the first order micromotion sideband strength as a function of the axial compensation voltage. These methods are developed and implemented by Jacopo Mosca Toba.

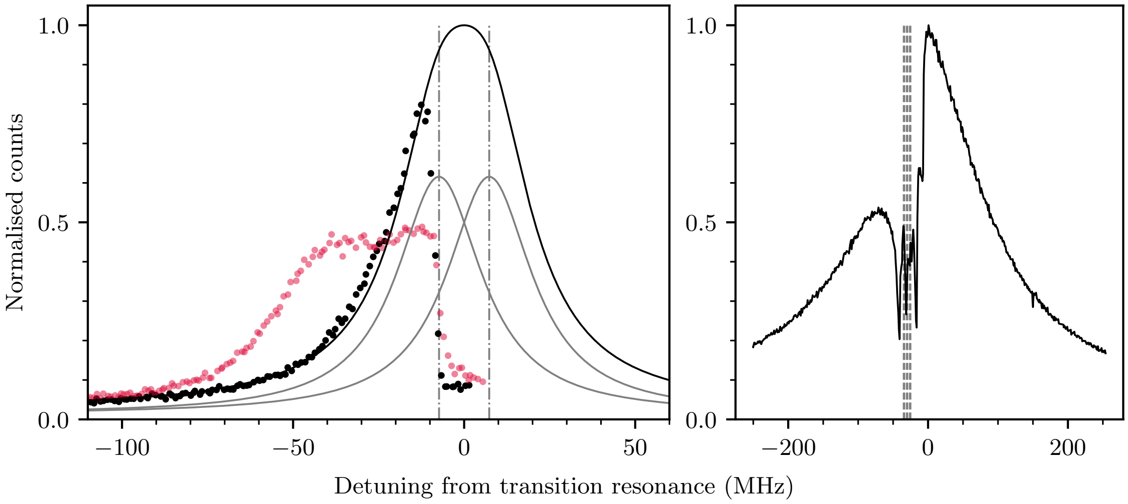

Figure 4.3.6: Resonance scan of the $S_{1/2} \leftrightarrow P_{1/2}$ transition (left), with data before (red) and after (black) compensation of the micromotion. The fit (black) is made to a sum of two Lorentzian functions separated by the splitting of the σ-transitions at $B_{z'} = 0.38\,\mathrm{mT}$ (grey). This shows that the laser heats the motion when positively detuned from the lowest frequency transition, limiting the achievable Doppler temperature. The $D_{3/2} \leftrightarrow P_{1/2}$ transition is also shown (right), with dark resonances clearly visible.

4.3.5 Doppler Transition Resonances

The Doppler cooling 397 nm dipole transition is seen as a function of laser detuning from the resonance in fig. 4.3.6 (left), with broadening from excess micromotion also shown. The micromotion minimised lineshape is fitted with a sum of two Lorentzian functions, separated by the σ-transition Zeeman splitting of 14.6 MHz, shown by the dashed lines. This splitting is comparable to the transition linewidth, and consequently photons are preferentially scattered on the lower energy transition. This model does not incorporate Gaussian velocity broadening, however the amount of information that can be extracted from this method is limited. The motion after Doppler cooling is better characterised by spectroscopy of the motional sidebands such as in fig. 4.4.4.

Repumping decay to $D_{3/2}$ level broadens the effective lineshape further. The 866 nm resonance is shown in fig. 4.3.6 (right), with dark resonances exhibited when both lasers are detuned by the same amount, and so form a three level system with the $S_{1/2}$ and $D_{3/2}$ states coupled via $P_{1/2}$. This coherently pumps the population into the dark state, and is avoided by positively detuning the repump laser. After a Doppler cooling time $T_{DC} = 5\,\mathrm{ms}$ the motion of the ion is maximally cooled, with the motion typically more energetic than the idealised approximation of the Doppler limit.

4.4 An Optical Qubit

The optical qubit is mapped onto specific states in the $S_{1/2}$ and $D_{5/2}$ energy levels, and the spectroscopy laser is tuned to the frequency difference between states to drive carrier transitions. The estimation of the qubit excitation probability and determination of errors in the statistical measurement process is discussed in section 4.4.1. With measurements of the qubit state, the time taken to optically pump into the ground state (OP and SP) and to remove the ion from the excited state (DS) are determined in section 4.4.2. Time evolution of the qubit under continuous driving is characterised by the coupling strength, or Rabi frequency, and the relative amplitude of motional sidebands is determined by the average motional state occupied by the ion. In section 4.4.3 the effective Rabi frequencies of carrier and first order transitions are measured, and this enables an estimation of the harmonic oscillator state. The temperature of the ion is also obtained from frequency spectra, section 4.4.4, which shows that the state $|\downarrow, 0\rangle$ can be prepared with 98(2)% probability.

4.4.1 Measurement

Measurement reduces a quantum system to one of the basis states of the measurement observable. With a single measurement it is therefore not possible to determine the probability amplitudes of the system states. The state of the optical qubit is determined by electron shelving [11]; under Doppler cooling the ground state $|\downarrow\rangle$ couples to the $P_{1/2}$ level and the ion emits fluorescence, whereas the excited state $|\uparrow\rangle$ does not, and the ion remains dark. From this measurement the ion is characterised as either bright or dark, corresponding to the system now being in the ground or excited qubit states, and is a measurement of the σ_z-observable, with the probability of measuring a state given by the square of its probability amplitude. Repeated measurement of an identically prepared system is required to determine the probability amplitudes, where the total number of trials $n = n_B + n_D$, is comprised of a number of bright, n_B, and dark, n_D, results. From this it is possible to determine the probability that the qubit was excited, with a binomial confidence interval giving an estimate of the error.

The normal approximation gives the probability of excitation as

$$P(\uparrow) = \frac{n_D}{n} \pm \frac{z}{n}\sqrt{\frac{n_B n_D}{n}}, \tag{4.4.1}$$

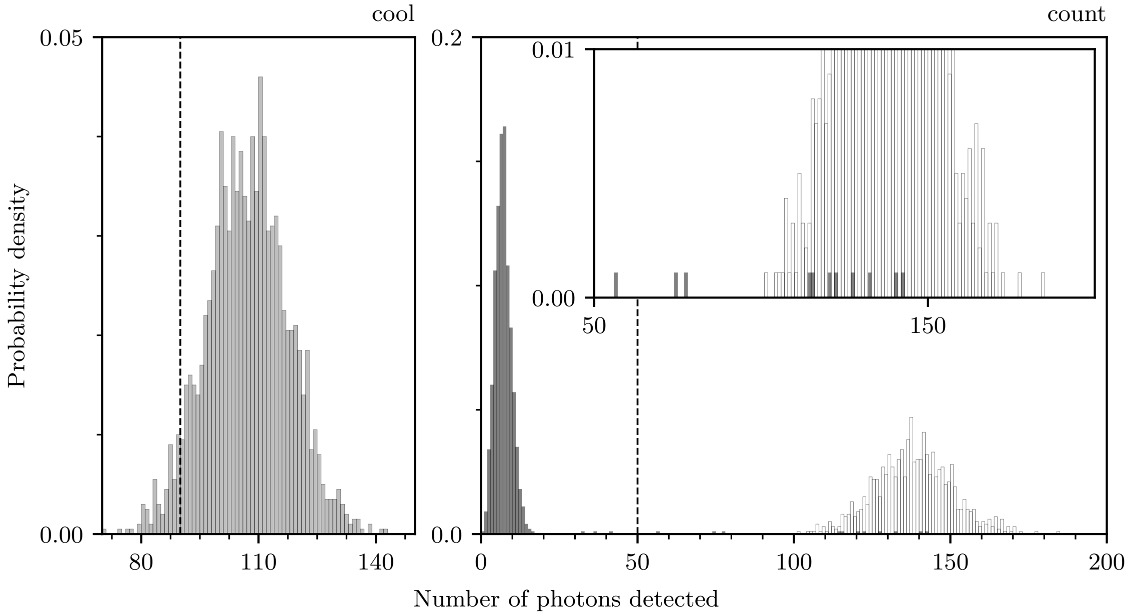

Figure 4.4.1: Counts during 5 ms Doppler cooling period (left). Counts during 5 ms state detection period (right), with bright (white) and dark (black) distributions taken independently with 1000 shots each.

where $z = 1.96$ for a confidence level of 95%. The error in this case would represent the interval we expect the true value to lie within with a 2-σ confidence bound. However this is unreasonable when the probability approaches 0 or 1. For example the ion may not be shelved in any shot, and would therefore have a probability of excitation and error of 0.

Wilson argues that the proper form of probable inference is to ask for what range of bounds would the measured value be expected to fall within [102, 103]. The Wilson score interval gives the probability of excitation as

$$P(\uparrow) = \frac{n_D + \frac{1}{2}z^2}{n + z^2} \pm \frac{z}{n + z^2}\sqrt{\frac{n_B n_D}{n} + \frac{z^4}{4}}. \tag{4.4.2}$$

The probability is modified from the standard case as the law of succession gives the probability of success in the $(n + 1)$st trial. The confidence interval can be asymmetric about the mean value, allowing valid non-zero errors when the mean is close to 0 or 1. This function, shown in appendix D.3, is used to determine the excitation probability and error bars in all data plots of the qubit excitation probability.

In fig. 4.4.1 (left) the photon counts during initial Doppler cooling are shown. A cooling threshold is set to ensure that the ion is well localised before sideband cooling is initiated. Photon counts for time $T_C = 5\,\mathrm{ms}$ with the ion prepared in the bright and dark states measured independently with 1000 shots are shown in fig. 4.4.1, showing a clear threshold

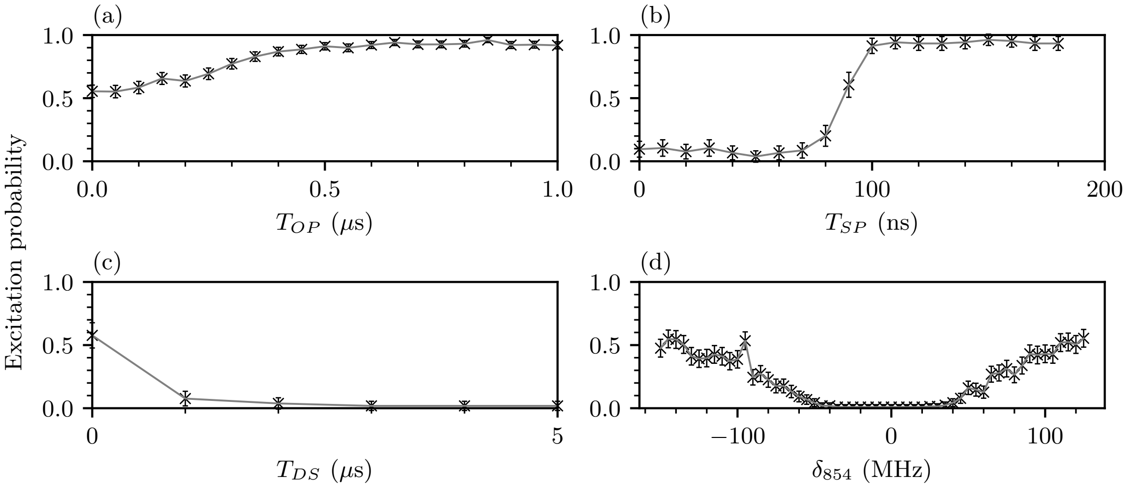

Figure 4.4.2: Excitation probability after driving the carrier transition following (a) Doppler cooling and scanning the optical pumping time; (b) sideband cooling, whilst scanning the length of the state preparation pulses after deshelving; (c) Doppler cooling, followed by a variable length deshelving pulse; and (d) Doppler cooling and deshelving the ion as a function of the detuning from the 854 nm transition.

between the distributions for each basis state. The bright distribution is taken directly after sideband cooling. The dark distribution is determined by shelving the ion with a π-pulse on the carrier. This gives a false bright rate of 1.1%, with an error margin of $1/\sqrt{1000} \approx 3\%$ for this number of shots. There are no counts below the threshold for the bright distribution as a result of the cooling threshold.

4.4.2 State Preparation and Deshelving

After Doppler cooling the electron is equally likely to be in either of the ground $S_{1/2}$ states, limiting the probability of exciting the qubit to 50%. This is shown after Doppler cooling and with zero optical pumping time in fig. 4.4.2 (a). The probability is maximised by $T_{OP} = 1\,\mu\text{s}$, however does not reach 1 as the motion is thermal. Preparation of the qubit ground state $|\downarrow\rangle$ requires optical pumping into one of the $S_{1/2}$ sub-levels using the circularly polarised $397C$ laser. In the interaction configuration shown in fig. 4.1.1, $\sigma_{+(-)}$ $S_{1/2} \leftrightarrow P_{1/2}$ transitions are driven by $\sigma_{+(-)}$ circularly polarised radiation. The final fidelity of the ground state preparation is limited by misalignment of the laser wavevector with the quantisation axis, and any ellipticity in the polarisation, both of which enable excitation of the unwanted σ-transition. A different optical pumping time is used during state preparation sideband cooling pulses, and the excitation probability after sideband cooling is shown in fig. 4.4.2 (b) while this parameter is varied. This shows that the ion will decay to the other ground state from $P_{3/2}$ and be shelved from the cooling cycle with insufficient state preparation time after deshelving pulses.

The 854 nm laser drives σ-transitions, and can therefore clear all levels in the $D_{5/2}$ manifold. It must also drive population that has decayed back from $P_{3/2} \rightarrow D_{5/2}$. The time required to return the electron from the exited state to the Doppler cooling cycle is shown in fig. 4.4.2 (c), where a variable length deshelving pulse is shown after exciting the qubit. After only 5 µs the electron decays to the $S_{1/2}$ manifold. From here it is prepared in the qubit ground state by the previously discussed state preparation pulse. The optimal frequency for the 854 nm laser is also determined by exciting the qubit while scanning the frequency, shown in fig. 4.4.2 (d). The electron is not deshelved if the pulse is not resonant with the $D_{5/2} \leftrightarrow P_{3/2}$ transition.

4.4.3 Rabi Oscillations

Evolution of the qubit state from the prepared ground state is determined in section 3.3, where for $m = 0$ eq. (3.3.8) describes the carrier, $m = -1$ the first red and $m = 1$ the first blue sideband. The dynamics are given by an incoherent sum over the evolution of each Fock state in a thermal distribution characterised by $\bar{n}$, and weighted by the probability of occupation following eq. (3.4.3):

$$|c_{\uparrow}(t)|^2 = \sum_{n=0}^{n_{max}} \frac{\bar{n}^n}{(\bar{n}+1)^{n+1}} \sin^2\left(\frac{\Omega_{n,n+m}}{2}t\right). \tag{4.4.3}$$

The motional state of the ion after both Doppler and sideband cooling can be characterised by a thermal distribution, where only the lowest two states are significantly populated after sideband cooling. Measured values of the excitation probability of the carrier and first order sidebands as a function of interaction time are fitted to eq. (4.4.3) in fig. 4.4.3. The damping of oscillations is increased with the higher motional temperature after Doppler cooling (top 3 plots), and high visibly is observed after preparing the ground motional state following sideband cooling (bottom 3 plots). Values for $\bar{n}$ and the Rabi frequency $\Omega_{0,0}$ are obtained by fitting to all 3 sidebands with the same model, giving $\bar{n} \approx 30$ after Doppler cooling and $\bar{n} = 0.09(1)$ after sideband cooling. This does not take into account off-resonant excitation, most notably of the carrier transition when driving first order sidebands, and does not account for detuning from the resonances.

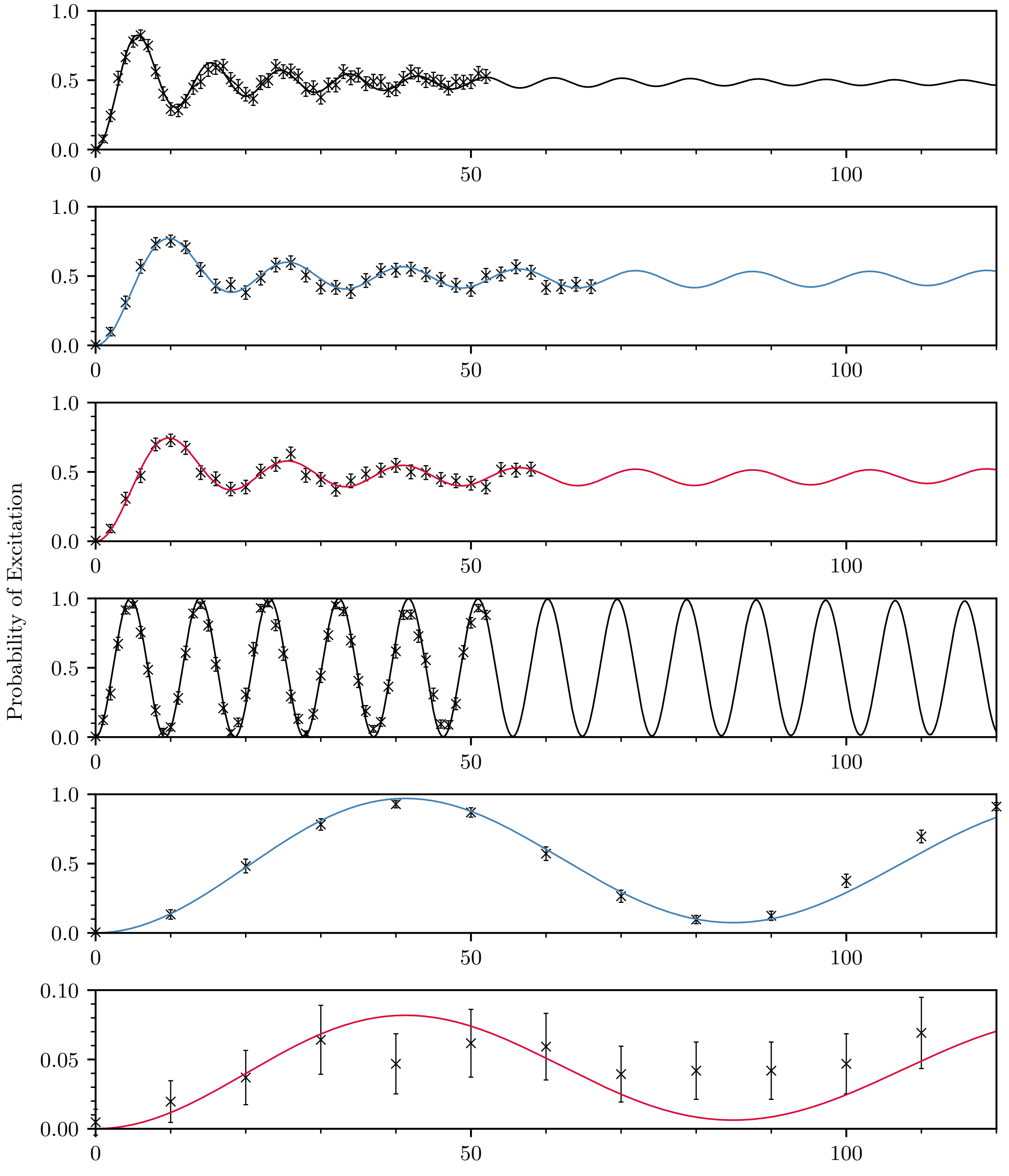

Figure 4.4.3: Rabi flops on the carrier and first order sidebands after Doppler (top three plots) and sideband (bottom three plots) cooling. The trap frequency is $\nu_z = 805\,\mathrm{kHz}$. The fit to all 3 sidebands after Doppler cooling gives $\bar{n} = 28.8(12)$ and $\Omega_0/2\pi = 110.0(6)\,\mathrm{kHz}$, and after sideband cooling $\bar{n} = 0.09(1)$ and $\Omega_0/2\pi = 109.0(1)\,\mathrm{kHz}$. The error in the fit is the covariance in parameter estimation, and gives an indicatation of the relative uncertainty.

4.4.4 Frequency Spectra

The probability of excitation was given as a function of the detuning δ from a particular sideband in eq. (3.2.12). To produce a model axial frequency spectrum, sidebands are positioned relative to the carrier by defining $\delta_m = \delta - m\omega_z$. Building on eq. (4.4.3), the probability of excitation as a function of detuning from the carrier and the probe time t is then given by

$$|c_{\uparrow}(t,\delta)|^2 = \sum_{m=-1}^{1} \sum_{n=0}^{n_{max}} \frac{\bar{n}^n}{(\bar{n}+1)^{n+1}} \frac{\Omega^2_{n,n+m}}{\Omega^2_{n,n+m}+\delta^2_m} \sin^2\left[\frac{\sqrt{\Omega^2_{n,n+m}+\delta^2_m}}{2}t\right]. \tag{4.4.4}$$

The observed background offset y_0 is accounted for by defining the excitation probability,

$$p_{ex} = [1-y_0] \times [|c_{\uparrow}(t,\delta)|^2 + y_0]. \tag{4.4.5}$$

This function is used to fit frequency spectra, with the ground state carrier Rabi frequency Ω_0, trap frequency ω_z, $\bar{n}$, and y_0 left as free parameters. Multiple datasets can be fitted using the same model with the script in appendix D.1, which allows wide range low resolution scans and high resolution scans of the features to be used in obtainig the best estimation of the free parameters. To increase the speed of the fit, the time taken to create the model was reduced by pre calculating sideband and carrier Rabi frequencies as a function of the motional state from $n = 0$ to $n_{max} = 250$ in the interaction class. Calculating the factorial terms in the definition of Ω_0 in eq. (3.3.8) is also time consuming, and the time taken to create the model was further reduced by the conditional statements from line 103 in appendix D.2 for low order sideband strengths.

A frequency spectrum of the axial mode is shown after Doppler cooling in fig. 4.4.4, which presents a low resolution scan of the carrier and first order sidebands, in addition to higher resolution scans of these features. Fitting gives an average thermal occupation of $\bar{n} = 20(1)$. The Doppler limit at a trap frequency of 805 kHz is characterised by $\bar{n} \approx 15$. The same method is used to obtain frequency spectra after sideband cooling, shown in fig. 4.4.5. The fitted model for the sideband cooled data gives $\bar{n} = 0.02(1)$, implying that 2 % of the population is outside the state $|\downarrow, 0\rangle$. As the strength of sidebands exhibit more variation closer to the ground state, the estimated sideband cooled temperature has a lower margin of error than the Doppler cooled fit.

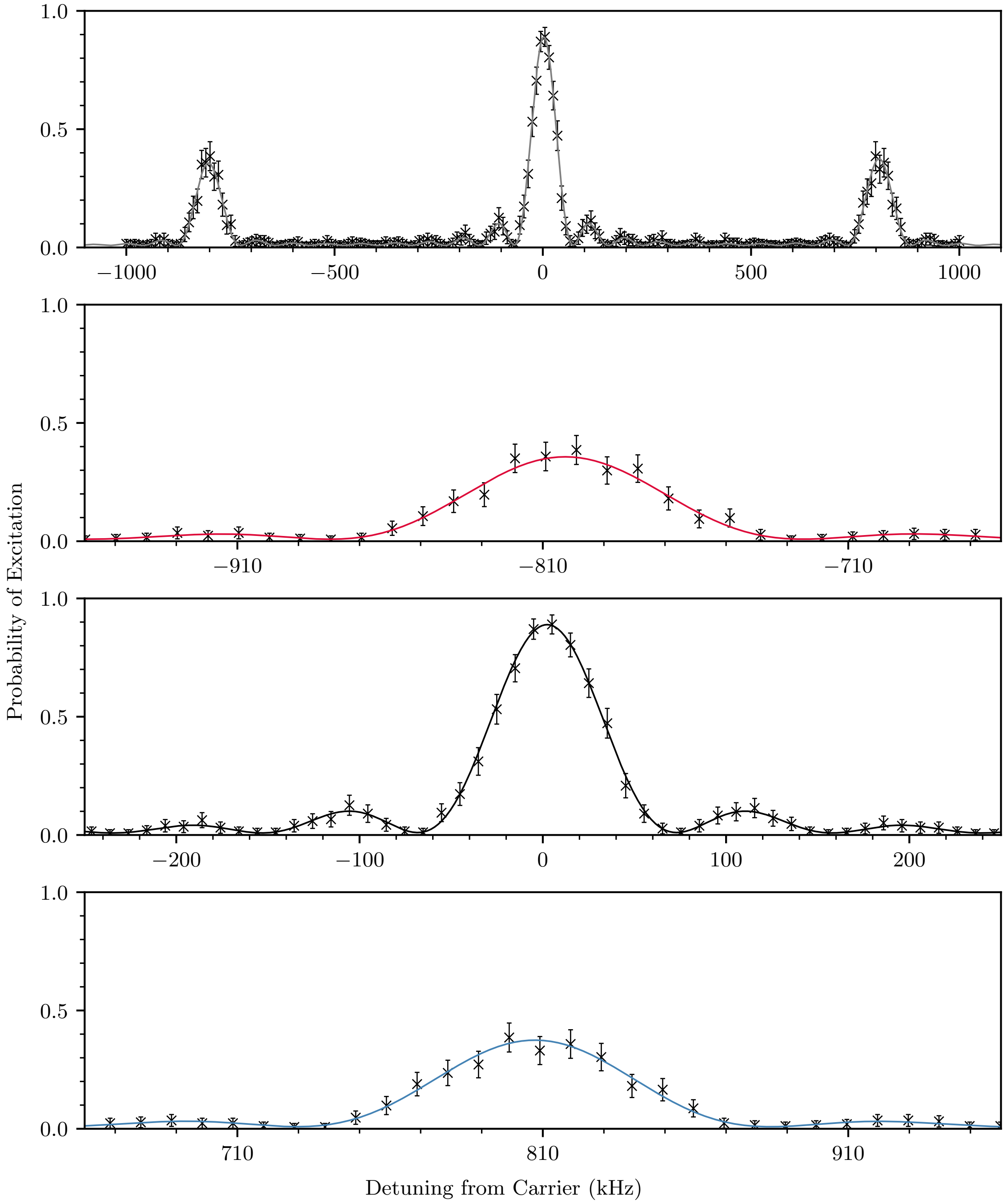

Figure 4.4.4: Doppler cooled axial frequency spectrum of first order sidebands at $\omega_z/2\pi \approx 810\,\mathrm{kHz}$. Excitation probability and errors of data are determined following eq. (4.4.2), with 250 shots per point. The fit is based on eq. (4.4.4), with free parameters: background excitation 0.008(2), $\bar{n} = 19.5(16)$, $\Omega_0/2\pi = 43.9(13)\,\mathrm{kHz}$, $\nu_z = 805.0(15)\,\mathrm{kHz}$. The probe time of 12.5 µs is chosen to maximise excitation of the carrier.

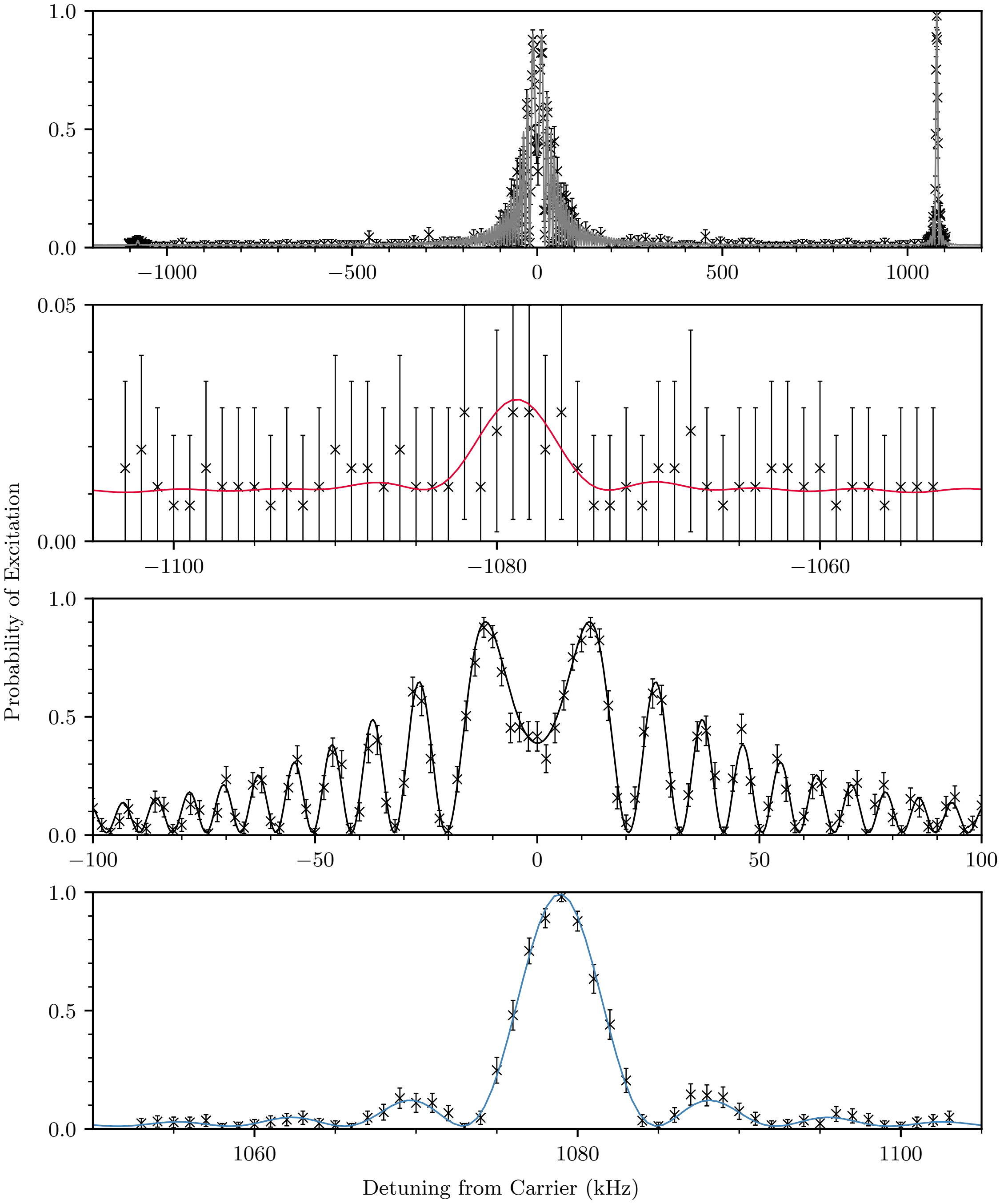

Figure 4.4.5: Sideband cooled axial frequency spectrum at $\omega_z/2\pi = 1.08\,\text{MHz}$. Plotted points are the result of 250 repetitions at each value of the detuning. The fit uses the same model as in fig. 4.4.4, with free parameters: background excitation 0.010(1), $\bar{n} = 0.02(1)$, $\Omega_0/2\pi = 36.10(3)\,\text{kHz}$, $\nu_z = 1078.8(1)\,\text{kHz}$. The probe time of 145 µs is chosen to fully excite the ion on the blue sideband.

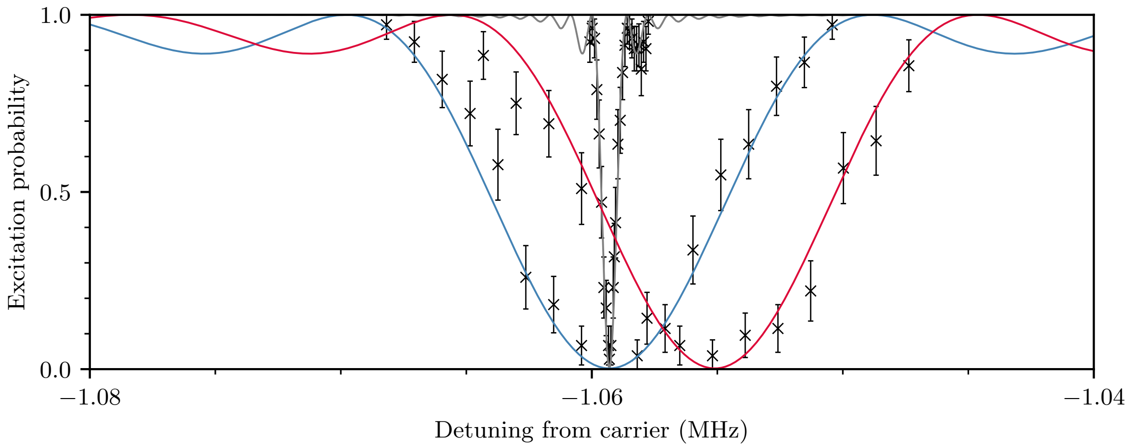

Figure 4.4.6: Stark shift compensation of the red sideband, probed from the state $|\uparrow, 0\rangle$. At low power, $\Omega_0/2\pi = 5\,\text{kHz}$ (grey), the trap frequency is measured as 1.06 MHz. At high power, $\Omega_0/2\pi = 70\,\text{kHz}$ (red), the red sideband is shifted by 4.2 kHz. Compensated red sideband at high power (blue).

4.4.5 Stark Shift Compensation

The presence of the high intensity spectroscopy laser field induces a shift in the carrier frequency through the AC Stark effect. If the radiation is tuned far from the transition, the shift in energy levels can be approximated by frequency

$$\Delta_S = -\frac{\Omega_0^2}{2\delta}, \tag{4.4.6}$$

where δ is the detuning from the carrier. This does not affect operations on the carrier, however when driving first order sidebands it can cause a measurable effect, as seen by the red sideband spectra at different Rabi frequencies in fig. 4.4.6. As there is no red sideband from the ground state, the state $|\uparrow, 0\rangle$ is prepared by a π-pulse on the carrier in order to measure the Stark shift. At high power, $\Omega_0 = (2\pi)70\,\text{kHz}$, the measured shift is $\Delta_S = (2\pi)4.2\,\text{kHz}$ for a detuning $\delta = \omega_z = (2\pi)1.06\,\text{MHz}$.

To compensate for this effect a second frequency component is used to induce the opposite shift in the energy levels. The detuning and amplitude of this second tone must satisfy

$$\frac{\Omega_0^2}{2\delta_A} = -\frac{(\Omega_0')^2}{2\delta_B}, \tag{4.4.7}$$

where the detuning of the tones must have opposite signs. To avoid resonance with other transitions, in this case the blue sideband, the detuning of the compensation pulse when driving the red sideband is set to $\delta_B = -1.5\delta_A$. The required Rabi frequency Ω_0' is determined experimentally.

Chapter 5

Quantum Coherence

In the Young–Feynman double slit experiment, single electrons are repeatedly sent through a pair of slits, where their cumulative detection leads to an interference pattern on the screen behind [104, 105]. This highlights a defining feature of quantum mechanics: that coherence is observed between alternative paths of a particle, or that a single particle can be de-localised. Coherence between paths is shown by the interference of their state probability amplitudes $\psi_1(\phi_1)$ and $\psi_2(\phi_2)$. The probability of detecting an electron as a function of the phase difference between paths, $\phi = \phi_1 - \phi_2$, is determined by the square modulus of the sum of the individual amplitudes,

$$P(\phi) = |\psi_1 + \psi_2|^2 = |\psi_1|^2 + |\psi_2|^2 + 2|\psi_1||\psi_2| \cos(\phi). \tag{5.0.1}$$

If one of the slits is blocked, or some information obtained about which path the electron has taken, then the interference term disappears, and the classical case is recovered [106].

Coherent superpositions between the basis states of a quantum system account for the majority of areas in which classical and quantum physics give diverging predictions, for example the two photon interference shown by the Hong–Ou–Mandel effect [107], or the interference between mesoscopic molecules [108]. They also underpin the algorithmic advantage that can be achieved by quantum computation and simulation [109, 110]. The distinction between quantum and classical coherence, however, is difficult to define. It is possible to create superpositions between the classical coherent states of light, which exhibit interference, and it can be hard to determine the presence of quantum coherence over the distinctly classical coherence exhibited by vibrational motion in classical mechanics [111]. One distinction is that the properties of a classical system can be measured to completely define the state, whereas measurement of a quantum system is destructive, and a result is determined statistically from many realisations of an experiment. This complicates the task of distinguishing coherent superpositions in quantum systems from probabilistic mixtures, and requires similar tools to entanglement theory. We therefore limit the definition of quantum coherence to coherence between the states of a quantum system.

The emergence of quantum information science over the past few decades has resulted in the desire to describe quantum physical phenomena as a resource which can be used to achieve tasks that would not be possible in the realm of classical physics [112–115]. Methods for quantifying the level of coherence present in finite d dimensioned quantum systems typically involve reconstructing the full density matrix to perform state tomography [116–118]. These suffer from the growing number of precise measurements that must be performed as the system scales, and explore little of the concept of higher-order coherence, where $d > 2$. This is analogous to multipartite entanglement [113], where the number of coherently superposed amplitudes is the quantity of interest, and is itself defined as a resource [119]. Statistical properties of an interference pattern can contain information about the underlying quantum state [120]. They are also generated by simple projective measurements which vary a single parameter. In section 5.2 an interference pattern based coherence metric [121] is implemented to verify the number of coherently superposed amplitudes in the axial mode of a single trapped ion. While ref [121] shows the robustness of the certifier to false positives, it does not extend the proof to the case where the projective measurement is made on a coupled basis, such as the case in our trapped ion system. In ref [122] we show that the metric is still valid when the interference pattern is derived from a mapping onto a coupled basis, enabling insight into noisy quantum systems not accessible by direct measurement.

Preserving coherence in quantum systems requires techniques to minimise experimental noise. Unwanted coupling to the environment can lead to the loss of phase information between basis states, causing a superposition to decay into a classical mixture [123]. Decoherence of the motional modes is a significant limitation in quantum logic applications with trapped ions, and the duration over which the states remain sufficiently coherent must be much longer than typical operation times if manipulation is to be realised with high fidelity. In a trapped ion system the qubit and motional states are subject to different sources of noise, and these are characterised in section 5.1. The classification of decoherence in higher order superpositions in noisy systems further motivates the development of a mechanism for certifying multilevel coherence.

5.1 Decoherence

The probability of qubit excitation in eq. (3.2.12) was given as a function of the detuning δ and the pulse area of the interaction, defined by the effective Rabi frequency $\Omega = \sqrt{\Omega_0^2 + \delta^2}$ and pulse time t. In eq. (4.4.3) this was modified to account for the dependence of the Rabi frequency on the occupied motional state n, which showed that the visibility of oscillations is more quickly washed out when more motional states are occupied. However when only the ground motional state is occupied this formalism would imply that, on resonance, the interaction gives full visibility oscillations for all time.

We have so far assumed that the experiment is a closed system, and that the dynamics are described by unitary transformations. In reality the environment can interact with our system of interest, and reduce the visibility of Rabi oscillations. Imperfect calibration of carrier and trap frequencies and sideband coupling strengths will mean the desired qubit rotation is not achieved. These parameters also drift with changing environmental conditions over the course of an experiment, which tends to reduce the visibility of interference fringes. Environmental coupling also causes decoherence between prepared quantum states in trapped ions, and these mechanisms are well established [40, 71]:

- Qubit (Optical) Decoherence
  - Fluctuation in the magnetic field strength on the timescale of the interaction broadens the qubit linewidth through Zeeman splitting.
  - Similarly the short term frequency stability of the laser will broaden the effective linewidth of the interaction.
  - The excited state spontaneously decays with a lifetime of $\approx 1\,\mathrm{s}$.
- Motional Decoherence

- Sufficiently fast noise in the strength of the trapping potential, and therefore trap frequency, reduces the purity of prepared Fock states.

Ramsey Spectroscopy

One method to probe the coherence of the qubit is to drive continuous Rabi oscillations from the ground state and model the decay in visibility. However the contrast is sensitive to imperfect calibration, intensity fluctuations in the laser, and contributions from any occupied higher motional states. Ramsey spectroscopy, proposed by Norman Ramsey in the 1960s [124], is not sensitive to these features. In one method of Ramsey interferometry [70], the qubit is initially prepared in an equal superposition of the two basis states by a carrier $\pi/2$ pulse, defined in eq. (3.3.14), to give

$$|\psi_1\rangle = \mathcal{U}_c(\pi/2,0)\,|{\downarrow}\rangle = \frac{1}{\sqrt{2}}[|{\downarrow}\rangle + |{\uparrow}\rangle]. \tag{5.1.1}$$

After a second $\pi/2$ pulse with phase ϕ relative to the first pulse, the states acquire a phase $e^{\pm i\phi}$. Measuring the excitation probability as a function of ϕ then produces an oscillatory pattern which follows

$$p(\phi) = |\,\langle{\uparrow}|\,\mathcal{U}_c(\pi/2,\phi)\;|\psi_1\rangle\,|^2. \tag{5.1.2}$$

$$= \frac{1}{2}\left[1 + \cos(\phi)\right]. \tag{5.1.3}$$

The visibility of the interference pattern over one period in the phase, A, is a function of a wait time T_w, where the superposition is left to freely evolve between carrier pulses. The visibility is reduced by optical decoherence, which is modelled by the modifying eq. (5.1.3) to give

$$p(\phi) = \frac{1}{2}\left[1 + A(T_w)\cos(\phi)\right]. \tag{5.1.4}$$

With no means of measuring in the motional basis, the coherence of motional state superpositions must be inferred from measurement of the qubit. As the coupling strength from each motional level is well known, and is simplified in the Lamb–Dicke regime, the state amplitudes can be determined from Rabi type oscillations on the sidebands. However despite being a coherent process this method offers no information about the phase relationship between amplitudes. Fortunately motional coherence can also be probed through

Ramsey experiments. From the superposition state $|\psi_1\rangle$, an equal superposition of the lowest two oscillator states is created by moving the excited state population on the first red sideband into the first motional state,

$$|\psi_2\rangle = \mathcal{U}_r(\pi, 0)\,|\psi_1\rangle = \frac{1}{\sqrt{2}}[|{\downarrow}, 0\rangle + |{\downarrow}, 1\rangle], \tag{5.1.5}$$

which is possible due to the lack of red sideband from $|{\downarrow}, 0\rangle$. The superposition is then mapped back onto the qubit after the wait time T_w, with the interference pattern given by

$$\begin{aligned} p(\phi) &= |\,\langle{\uparrow}|\mathcal{U}_c(\pi/2, \phi)\,\mathcal{U}_r(\pi, 0)\;|\psi_2\rangle\,|^2 \qquad (5.1.6)\\ &= \frac{1}{2}\left[1 + B(T_w)\cos(\phi)\right]. \qquad (5.1.7) \end{aligned}$$

As with the qubit Ramsey experiment, the fidelity of pulses will affect the initial amplitude of $B(T_w)$, but decay of the observed visibility depends on the form of the underlying noise spectrum.

5.1.1 Optical Decoherence

Decoherence of a prepared quantum state results from the weak coupling to any fluctuations in the environment. A qubit is often mapped onto two energy levels, and in physical systems the excited state can 'relax' back to the ground state, similar to a classical bit flip error. This corresponds to all points on the Bloch sphere contracting towards the north pole, figure 8.14 in [22]. As the decay time on the quadrupole transition is long, this effect is relatively weak, and we can limit the discussion to low frequency dephasing between the basis states. Rather than driving transitions between the states, low frequency noise ($\ll \omega_{\downarrow\uparrow}$, the qubit splitting) leads to phase flip errors. This corresponds to the x and y axes of the Bloch sphere contracting towards the z-axis, which is unaffected, as seen in figure 8.9 of [22]. This is seen through the density matrix representation, which for the pure state $|\psi_1\rangle$ is given by the outer product

$$\rho = |\psi_1\rangle\,\langle\psi_1| = \frac{1}{2}\begin{bmatrix} 1 & 1 \\ 1 & 1 \end{bmatrix}. \tag{5.1.8}$$

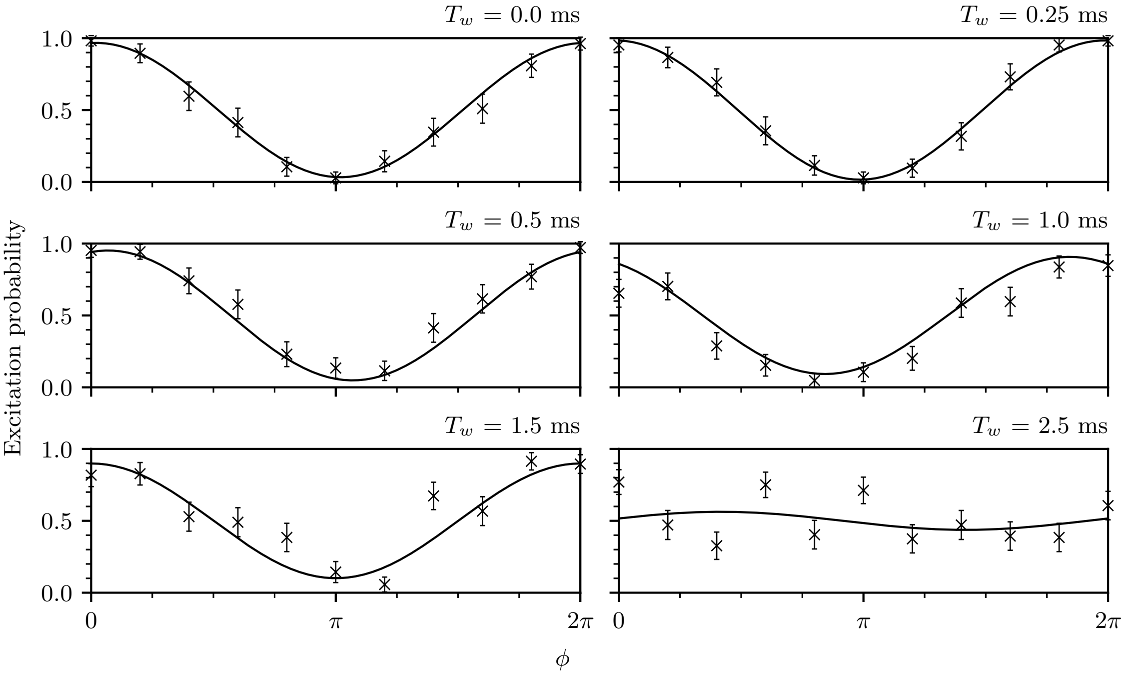

Figure 5.1.1: Optical Ramsey interference measurements on the π-transition. Shown for a range of wait times inserted between the two pulses. The interference pattern is obtained by varying the phase ϕ of the second pulse.

This state tends towards an equally weighted mixed state under dephasing, which reduces the off-diagonal elements to zero until no correlations remain. The state can then be described by vectors pointing only to the north and south poles on the Bloch sphere.

A typical interaction time is in the region of 10 to 100 µs, and to give an error contribution of 1% the system requires a coherence time on the order of 1 to 10 ms. The lifetime of the excited qubit state places an upper limit on the optical coherence time. However this state is long lived, and effectively stable, so the optical coherence time is governed by the linewidth of the qubit driving laser, and the noise in the splitting of m_j energy levels due to fluctuations in the quantisation field. The contribution from both magnetic and laser field noise can be deduced as the quadrupole transitions have different sensitivity to the magnetic field strength, whereas the laser linewidth is constant. The main transition used in our experiment is the $\mathrm{S}_{1/2,-1/2} \leftrightarrow \mathrm{D}_{5/2,-1/2}$ π-transition, which is least sensitive to magnetic field noise following eq. (3.1.1). From this ground state, and in the geometrical configuration of fig. 4.1.1, the two δ-transitions from $\mathrm{S}_{1/2,-1/2}$ can be driven. These transitions are respectively 5 and 7 times more sensitive than the π-transition to the magnetic field strength.

Ramsey fringes are plotted in fig. 5.1.1 for a range of wait times T_w in an optical Ramsey experiment. The fitted model to eq. (5.1.4) gives the amplitude A, which is reduced for longer wait times between Ramsey pulses. The form of the decay in fringe visibility as a function of the wait time in Ramsey experiments will depend on the underlying sources of noise present. If there are many sources of noise then we can initially assume that Gaussian statistics will describe the process. If the noise is limited to variation in the laser and transition frequencies, this will affect the phase through eq. (5.1.3). If this noise is fast compared to the wait time, then Gaussian white noise in the frequency will lead to an exponential decay of A,

$$A(T_w) = A_0 e^{-T_w/\tau_2}, \tag{5.1.9}$$

where A_0 is the amplitude at $T_w = 0$, and τ_2 is the characteristic time scale. If the timescale of the noise is longer than the wait time, then the functional form of the decay will be determined by the underlying noise distribution [71]. A Gaussian model,

$$A(T_w) = A_0 e^{-T_w^2/\tau_2^2}, \tag{5.1.10}$$

would therefore describe the loss of coherence observed. The Gaussian model would imply that the coherence time is limited by noise on a longer timescale than the wait time, and is observed in other rf traps [40].

Ramsey experiments on the π and δ-transitions in fig. 5.1.2 show the data is well modelled by a Gaussian decay, with $R^2 = 0.89$, as opposed to $R^2 = 0.66$ for the exponential model. The Gaussian fit gives a characteristic coherence time of $\tau_2 = 2.5(2)$ ms on the π-transition. The implied qubit linewidth from the decay times are also shown in fig. 5.1.2, and increase linearly with the relative sensitivity of the transition to the magnetic field as expected [125]. This shows that noise in the magnetic field magnitude at the ion is the predominant source of noise, and not the short term linewidth of the interaction laser, which has an implied linewidth of ≈ 18 Hz. Further information about the underlying noise distributions can be obtained by using dynamical decoupling schemes.

Spin Echo

Frequency noise leads to phase noise in Ramsey experiments. This can be depicted by the Bloch vector spreading across the equator of the sphere shown in fig. 5.1.3 (b) during

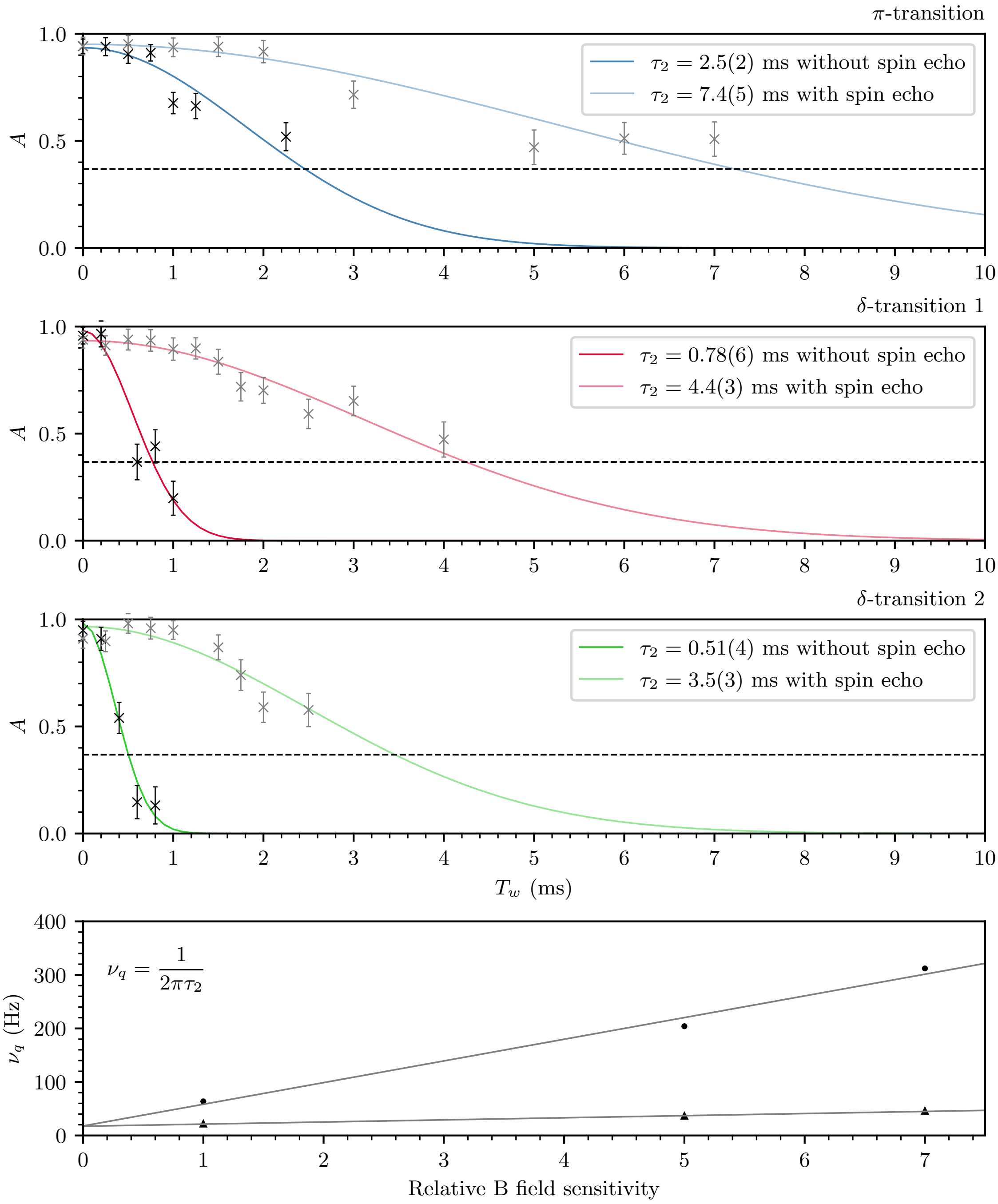

Figure 5.1.2: Ramsey optical coherence measurement, determined by extracting the visibility A of Ramsey phase scans as a function of wait time T_w, where the qubit superposition is left to freely evolve. The ground state is $\mathrm{S}_{1/2,-1/2}$, and the excited states are $\mathrm{D}_{5/2,-1/2}$ (π-transition), $\mathrm{D}_{5/2,-5/2}$ (δ-transition 1), and $\mathrm{D}_{5/2,3/2}$ (δ-transition 2). The δ-transitions are 5 and 7 times more sensitive to the magnitude of the magnetic field than the π-transition respectively. The bottom plot shows the qubit linewidth as a function of the relative sensitivity to the quantisation field, with (triangles) and without (points) spin echo. Respectively the fits have a gradient of 4 and 40 Hz per relative sensitivity to the quantisation field, and cross the y-axis at 17.3 and 17.8 Hz. This is the implied linewidth of the interaction laser, as the most significant contribution to the optical qubit linewidth in the absence of magnetic field noise. Data taken by Jacopo Mosca Toba.

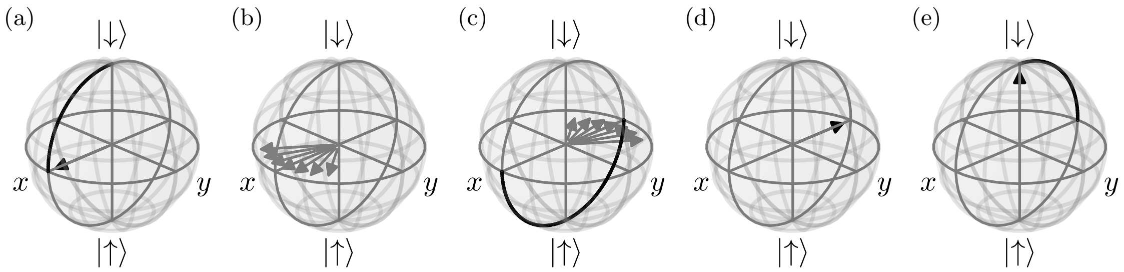

Figure 5.1.3: Bloch sphere representation of the spin echo pulse sequence. An equal superposition is prepared in the qubit (a) where the state can decohere during the wait time (b). A π-pulse in the middle of the wait time (c) then leads to the state vector recohering (d), which the final pulse returns to the ground state (e).

the wait time between Ramsey pulses. Low frequency noise can be damped by using spin echo pulses, carrier π-pulses inserted in the middle of the wait time to exchange the qubit excited and ground state populations, as seen in fig. 5.1.3 (c). The phase acquired for a fixed detuning error before the spin echo pulse is cancelled out by the opposite phase during the second half of the wait time. An constant drift in experimental parameters is also cancelled out during the total wait time, and the coherence time is significantly extended as seen in fig. 5.1.2.

Mains Noise

Electronic apparatus generates magnetic fields which fluctuate with the mains period, and can be detected by the ion through an oscillation of the carrier frequency. In table 4.2.1 each experiment is triggered by the mains cycle at 50 Hz, and the circuit which delivers the trigger is described in appendix C. However in longer Ramsey experiments the wait time becomes comparable to the mains period of 20 ms, leading to a consistent phase accumulation as the second pulse becomes increasingly off-resonant. However as seen in fig. 5.1.2 magnetic field noise is greatly reduced by a single spin echo pulse, implying that noise induced in the qubit splitting is most likely caused by the low frequency mains period. Without reduction in the strength of the coupling to this external fluctuation, the idealised model of the electronic qubit breaks down rapidly. The validity is reduced further by calibration and measurement errors, which reduce the contrast of oscillations with t wait time $T_w = 0$.

5.1.2 Motional Decoherence

Other fluctuations in the environment cause an equivalent decay in the coherence of pure motional states into classically described mixed states. The harmonic trapping potential defines the axial frequency ω_z, however imperfections in this field and fast fluctuations in the voltage at the axial electrodes can lead to decoherence of prepared motional states. In the motional Ramsey experiment a period of free evolution is varied after separating the motional state of the ion into an equal superposition of the ground and first harmonic oscillator states. From the initial state $|\psi(0)\rangle = |\downarrow, 0\rangle$, an equal superposition of the qubit is created by a $\pi/2$-pulse on the carrier. As the remaining population in the ground state has no red sideband, a π-pulse on this transition transfers the excited state population into the first harmonic oscillator state. As only the qubit state can be measured, the motional superposition is then mapped back onto the initial state in order to maximise the visibility of Ramsey oscillations. The interference pattern is described by probability amplitude of the excited qubit state following these sideband operations,

$$p(\phi) = |\,\langle\uparrow|\,\mathcal{U}_c(\pi/2,\phi)\,\mathcal{U}_r(\pi,0)\,\mathcal{T}(T_w)\,\mathcal{U}_r(\pi,0)\,\mathcal{U}_c(\pi/2,0)\,|\psi(0)\rangle\,|^2. \tag{5.1.11}$$

During the wait time T_w the qubit state is completely decoupled from the motion, and as operations on the qubit are the same at all wait times, decay of the visibility is a result of the effective linewidth of the transition between motional states. The motional coherence is typically long compared to qubit coherence time.

5.1.3 Heating Rate

Where the motional coherence time was equivalent to that of the qubit, the heating of the motional state by the environment is equivalent to the qubit error induced by spontaneous decay of the excited $\mathrm{D}_{5/2}$ state. The amount of motional heating present is measured by evaluating the relative strength of the red ($i = -1$) and blue ($i = +1$) sidebands, $R_{sb} = p_{-1}/p_{+1}$, where

$$p_i = \sum_{n=0}^{200} \frac{\bar{n}^n}{(\bar{n}+1)^{n+1}} \sin^2\left[\frac{\Omega_{n,n+i}}{\Omega_{0,1}}\frac{\pi}{2}\right]. \tag{5.1.12}$$

This parameter varies significantly when the motional state is reduced into the LD regime, as seen in fig. 3.3.1. Knowing the LD parameter, the ratio of sideband strengths plotted

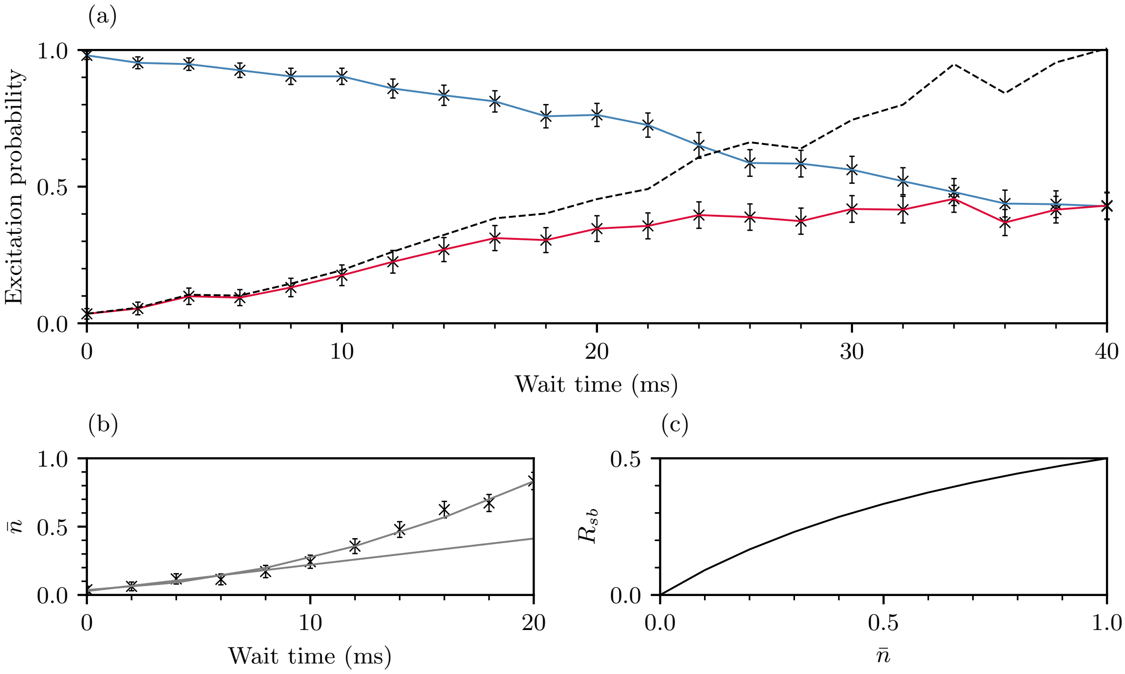

Figure 5.1.4: Heating rate measurement. (a) The strength of the red (red) and blue (blue) sidebands as a function of the wait time inserted between sideband cooling and measurement. The dashed line shows the ratio R_{sb}. (b) The implied average motional state $\bar{n}$, determined by the model defined in eq. (4.4.3). The grey lines show a linear and quadratic fit. (c) The conversion between the ratio of sideband strengths R_{sb}, shown dashed in (a), and the impled $\bar{n}$. Data from Chungsun Lee.

in fig. 5.1.4 (a) can be directly converted into an average motional state $\bar{n}$ in (b). The conversion, shown in fig. 5.1.4 (c) is determined from eq. (5.1.12), where the probe is defined such that the qubit is fully excited on the blue sideband when the ion is in the motional ground state. When $\bar{n} < 0.1$, the value is simply given by the ratio of red and blue sideband strengths R_{sb}. At $\bar{n} = 1$, for the parameters used here, the red sideband is half the strength of the blue.

The average motional state shown in fig. 5.1.4 (b) as a function of the wait time is well modelled by the quadratic fit, $R^2 = 0.99$. The liner fit over the first 10 ms, with $R^2 = 0.94$, gives a heating rate of 19 quanta s^{-1}. However this method is sensitive to drift in the spectroscopy laser frequency and power, and therefore calibration of the sideband peaks and Rabi frequency. A better estimation of the average motional state is obtained from full frequency spectroscopy over multiple sidebands, however as this takes 10s of minutes per scan, parameter drift is more significant. While the method of probing the peaks could be improved by taking more points around the peak, it allows for many measurements to be taken in a much shorter time in fig. 5.1.4. This may allow better characterisation of the sources of motional heating, and enable increased isolation from external noise.

5.2 Multilevel Coherence

Multilevel coherence is exhibited by a superposition of more than two basis state vectors. The level of coherence is defined with respect to the basis states, implying a state can be made arbitrarily coherent by the choice of the basis. In reality the relevant basis for coherence is the basis in which a measurement is made, and in a harmonically bound ion this is the Fock states of the motion $|n\rangle$. A pure state in this basis $|\psi\rangle = \sum_n \chi_n |n\rangle$ is then k-coherent if there are k non-zero amplitudes χ_n. In a physical system, with experimental errors and sources of decoherence, no prepared state will be pure. The level of coherence in a mixed state ρ is defined by the minimum number of k-coherent elements with non-zero probability q_i in the decomposition $\rho = \sum_i q_i |\psi_i\rangle \langle\psi_i|$. This is similar to definitions of multipartite entanglement for mixed states [113, 126].

A good coherence metric will produce a single value that determines the degree of multilevel coherence present in the tested state. It will create a discrete hierarchy if the maximum value achievable by the metric increases with each level of k-coherence. Measuring a value above a certain threshold will then unambiguously show that the tested state is at least k-coherent. The certifier must be robust against any conceivable imperfection in the implementation, such that the value obtained can never rise above a threshold it should not. This robustness in the certifier is a priority, and it may therefore fail to determine the presence of higher order coherence. In other words the metric will be able to certify the existence of multilevel coherence, but not prove its absence.

In the following section, and in ref [122], a method for certifying multilevel coherence in the motional Fock states of a trapped ion is demonstrated. In a 3-coherent state such as $(|\downarrow, 0\rangle + |\downarrow, 1\rangle + |\downarrow, 2\rangle)/\sqrt{3}$, interference between the three oscillator states is analogous to a triple slit style experiment. To create this state, and others, a method for generating any motional superposition is presented in section 5.2.1. A certifier satisfying the requirements previously outlined is then defined in section 5.2.2, which determines the level of coherence from statistical properties of an interference pattern. These interference patterns are presented in section 5.2.3, which discusses optimisation of the results. The reason higher order than 3-coherence could not be shown, and consequences for the utility of this certifier, are discussed in section 5.2.4.

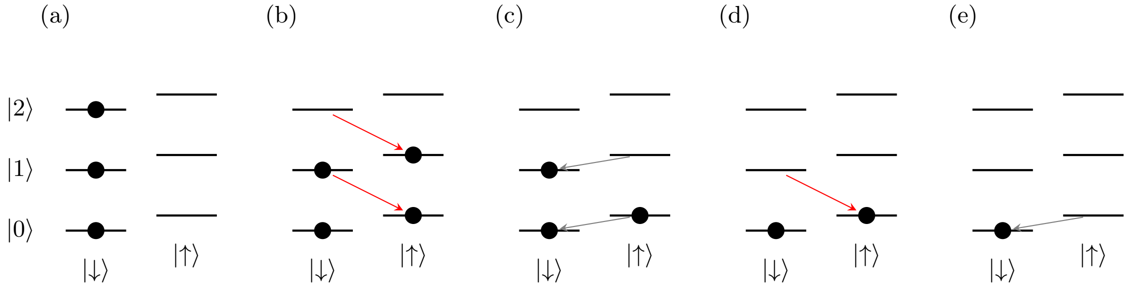

Figure 5.2.1: Determination of state preparation sequence for $(|0\rangle + |1\rangle + |2\rangle)/\sqrt{3}$. (a) Beginning in the desired state. (b) The population in the highest motional state $|2\rangle$ is first transferred to a lower state on the red sideband. (c) The population in the highest motional state, now $|1\rangle$, is then combined into the ground state of the qubit; alternatively the population can be combined into the excited qubit state. (d) The process in (b) is then repeated, with the motional level reduced to the ground state. (e) Finally the population is combined into the ground qubit state to give $|\downarrow, 0\rangle$, which is prepared by sideband cooling.

5.2.1 State Creation

It has already been seen that a superposition in the lowest two motional states can be constructed from the ground state, by first creating an equal superposition in the qubit and then transferring the excited population into the first motional state. The creation of higher order superpositions is possible with the same first order sideband pulses [127]. The pulse sequence required to create an arbitrary motional superposition from the initial ground state $|\downarrow, 0\rangle$ is determined by starting with the desired superposition state. An example is shown for creating the state $(|0\rangle + |1\rangle + |2\rangle)/\sqrt{3}$ in fig. 5.2.1. The first step (b) transfers all the population in the highest motional state into the excited state of the level below with a red sideband pulse. This also affects the population in lower motional states, which is tracked. In step 2 (c) the population in the highest motional state is combined into the ground or excited qubit states. These steps are repeated (d and e) until the population is swept into the ground state of the motion and qubit. The adjoint of this sequence of pulses, defined by the sideband, pulse rotation, and phase relative to the initial pulse, produces the creation sequence.

In theory there are an infinite number of pulse sequences that would create the desired superposition. The sequence of shortest duration is desirable as this is least sensitive to decoherence of the qubit states. Also considered is that where the time difference is minimal, reducing the number of sidebands used reduces the potential for calibration errors. The creation sequences used for a range of states to certify were found by Jake Lishman [102], and are shown on the left of table 5.2.1.

5.2.2 Certification

A coherence certifier is more useful if it can be performed with easily achievable operations. Ramsey experiments can be implemented with simple carrier and first order sideband pulses, and enable the construction of interference patterns by varying a single parameter in the driving field. Additionally the measurement is a projective measurement onto one of the qubit states. The interference patterns used here to certify higher order coherence are an extension to the Ramsey experiment [121], where the mixed state ρ to be tested undergoes a period of free evolution before being mapped back onto the measurement basis. As the free evolution dynamics are periodic, they can be given as a function of the phase of the period, $\mathcal{U}_f(\phi)$. The probability of measuring the excited state can then be written as

$$p(\phi) = \langle\uparrow| \mathcal{U}_m \mathcal{U}_f(\phi)\, \rho \mathcal{U}_f^\dagger(\phi) \mathcal{U}_m^\dagger |\uparrow\rangle\,, \tag{5.2.1}$$

where $\mathcal{U}_m$ is the mapping between the coherent basis of investigation and the coherent measurement basis. In the two state motional Ramsey experiments presented earlier this operation was the inverse of the creation sequence.

The certifier C is defined in ref [121], and gives a single value from a ratio of normalised moments of the interference pattern.

$$C = \frac{M_3}{M_1^2}, \qquad \text{where} \qquad M_n = \frac{1}{2\pi}\int_0^{2\pi} p(\phi)^n d\phi. \tag{5.2.2}$$

Obtaining a value of C greater than 1 shows 2-coherence, greater than 1.25 is required for 3-coherence, and 1.86 for certifying 4-coherence. In a trapped ion system the coherent motional basis of the target state is coupled to the qubit measurement basis, however the treatment of ref [121] is only valid when the measurement maps the tested state onto one of the coherent basis states. The proof is extended in ref [122] to show that the certifier is also valid when the interference pattern is derived from a mapping onto a coupled measurement basis.

Mapping

The mapping converts a measurement of the motional basis into a projective measurement on the qubit. Free-evolution of the state can then be used to construct an interference pattern. Whilst any mapping is valid, an optimal sequence will increase the chance of a

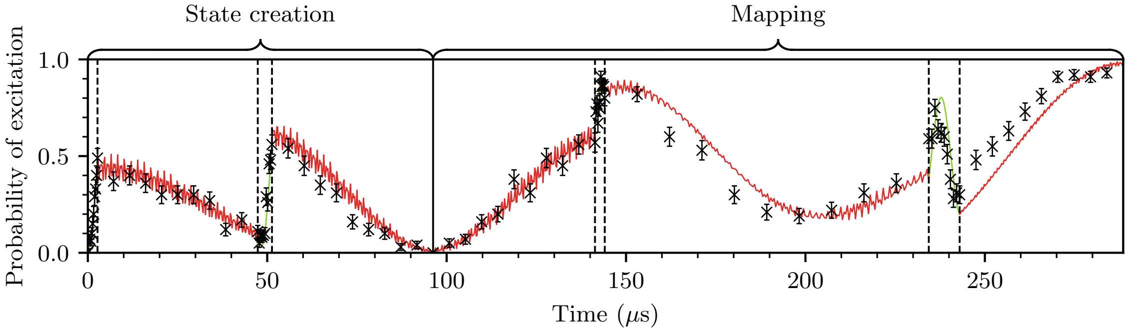

Figure 5.2.2: Evolution of the qubit state over the course of creation and measurement mapping of the motional superposition $(|0\rangle + |1\rangle + |2\rangle)/\sqrt{3}$. The data (black crosses) are compared to a model of the expected behaviour (coloured line). The model is developed using the QuTiP Python library by Simon Webster. As seen in table 5.2.1 this sequence uses only carrier (green) and red (red) sidebands.

positive result by maximising the contrast of the interference pattern. This is achieved by mapping the target motional superposition state onto one of the qubit states, say $|\uparrow\rangle$, and all orthogonal states to $|\downarrow\rangle$. In the two state Ramsey experiments presented earlier a mapping sequence that was the inverse of the creation operation satisfied this, however this is not the case for higher order superpositions. If the target state has a maximum occupied phonon state m, then there are $2m + 2$ states in the system basis that must be considered when constructing the mapping, and consequently the adjoint of the creation sequence does not necessarily result in full contrast patterns.

For the example of the three state superposition, the mapping should formally satisfy

$$\mathcal{U}_m(|\downarrow, 0\rangle + |\downarrow, 1\rangle + |\downarrow, 2\rangle) \propto |\uparrow, \lambda_1\rangle\,, \tag{5.2.3}$$

$$\mathcal{U}_m(|\downarrow, 0\rangle - 2\,|\downarrow, 1\rangle + |\downarrow, 2\rangle) \propto |\downarrow, \lambda_2\rangle\,, \tag{5.2.4}$$

$$\mathcal{U}_m(|\downarrow, 0\rangle - |\downarrow, 2\rangle) \propto |\downarrow, \lambda_3\rangle\,, \tag{5.2.5}$$

where the motional states λ_i can be chosen arbitrarily, as they do not affect the measurement, and the orthogonal states on the left hand side are only required to form a basis with the target state. In practice there are many sequences which can satisfy these conditions, and as with the creation sequence the projection is optimised for shortest duration. The mapping sequences for the example states are shown on the right of table 5.2.1.

Qubit State Evolution

The qubit state can be measured at any point during the course of the creation and mapping pulse sequences of the 3-coherent state $(|0\rangle + |1\rangle + |2\rangle)/\sqrt{3}$, and these measurements are compared with a simulation of the expected behaviour in fig. 5.2.2. The figure shows the pulse duration in terms of time, rather than pulse rotation, which highlights the fact that the sequence is dominated by the longer sideband pulses. Furthermore two high frequency components can be seen in the model when driving the red sideband. These are due to off-resonant excitation of the carrier from both the sideband and compensation pulses. In this experiment the target state should be mapped back onto the excited qubit state, but experimental errors stop the qubit state from being fully excited on completion of the operation.

With full control over the frequency and phase of each laser pulse, free-evolution can be implemented as a phase offset applied to the mapping pulses, as it was in the original Ramsey experiments. The carrier remains unshifted and the phase of the red and blue sidebands advanced by $-\phi$ and $+\phi$ respectively. The free-evolution dynamics $\mathcal{U}_f(\phi)$ are given by varying the phase over this free-evolution period. As each point in the pattern takes the same time, the method has the advantage that each point will be subject to the same decoherence processes. This is optimal for determining the initial presence of multi-level coherence.

The populations in the basis motional states after the creation sequence can be determined by measuring the qubit excitation probability while driving the blue sideband. The time scan can be modelled by a sum of the Rabi oscillations at frequency $\Omega_{n,n+1}$, weighted by the population χ_n of the m states considered. The model also includes the expected decay in visibility due to decoherence, with $\tau_2 = 2.5\,\mathrm{ms}$,

$$|c_\uparrow(t)|^2 = e^{-t^2/\tau_2^2} \sum_{n=0}^{m} \chi_n \frac{\Omega_{n,n+1}^2}{\Omega_{n,n+1}^2 + \delta_b^2} \sin^2 \left[\frac{\sqrt{\Omega_{n,n+1}^2 + \delta_b^2}}{2} t \right] . \tag{5.2.6}$$

The results of driving the blue sideband on resonance and the fitted state populations are shown in fig. 5.2.3. The fitted amplitudes confirm the created state has population in the expected states, and we can be confident in reducing the number of states considered in the mapping to the occupied ground states of the superposition. However the measurement gives no information about the phase relationship between the states, and the same results would be obtained from an incoherent mixture of the same basis state amplitudes.

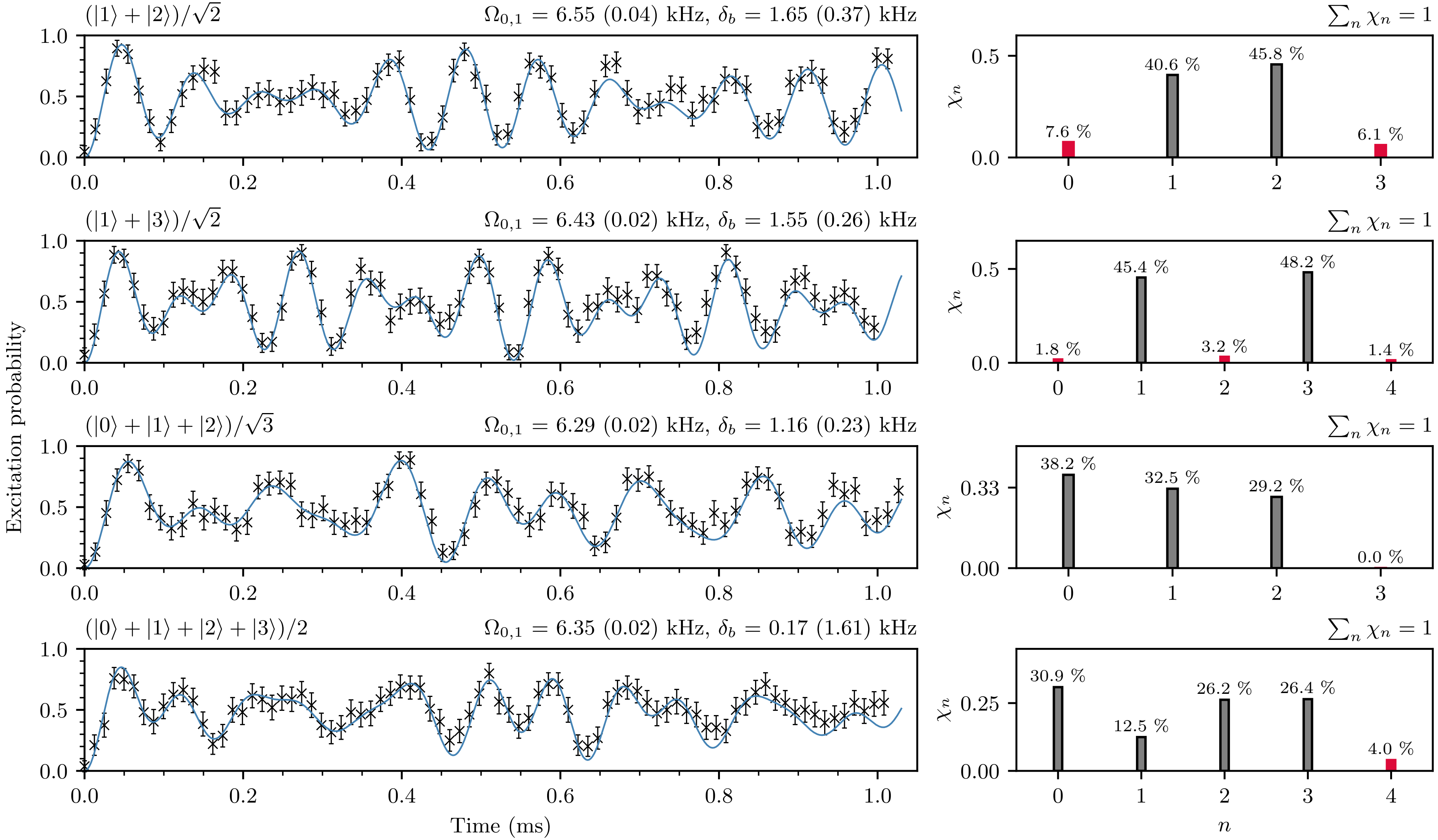

Figure 5.2.3: Qubit excitation probability while driving the blue sideband immediately after creation of the motional superpositions indicated. Data shown by black crosses. Free parameters from the fit (blue) to eq. (5.2.6) are the blue sideband Rabi frequency from the ground state $\Omega_{0,1}$, the detuning from the blue sideband δ_b, and the state amplitudes χ_n. The coherence time is fixed at $\tau_2 = 2.5\,\text{ms}$. This gives an estimate of the population in each of the oscillator states considered, shown right with undesired states in red, but there are many fitted parameters and the error ($\approx 3\%$ for state amplitudes) is only a measure of the covariance in the fit.

$(|1\rangle + |2\rangle)/\sqrt{2}$

	Creation				Mapping				
Transition	carrier	red	carrier	red	red	carrier	red	carrier	red
Pulse length	0.60	0.80	0.74	0.71	0.71	0.44	1.41	0.54	1.41
Phase offset/π	0	1.50	0	1.50	$0 - \phi$	1.34	$1.17 - \phi$	1.13	$1.59 - \phi$

$(|1\rangle + |3\rangle)/\sqrt{2}$

	Creation				Mapping						
Transition	carrier	red	blue	red	red	carrier	red	carrier	red	carrier	red
Pulse length	0.50	0.31	0.23	0.29	0.29	0.51	0.16	0.50	0.58	0.50	0.22
Phase offset/π	0	0	1.00	0	$0 - \phi$	0.52	$0 - \phi$	-0.48	$1.16 - \phi$	0.49	$1.81 - \phi$

$(|0\rangle + |1\rangle + |2\rangle)/\sqrt{3}$

	Creation				Mapping				
Transition	carrier	red	carrier	red	red	carrier	red	carrier	red
Pulse length	0.50	0.70	0.73	0.71	0.71	0.50	1.42	1.59	0.72
Phase offset/π	0	1.50	1.00	0.50	$0 - \phi$	0.71	$1.71 - \phi$	0.10	$1.49 - \phi$

$(|0\rangle + |1\rangle + |2\rangle + |3\rangle)/2$

	Creation						Mapping								
Transition	carrier	red	carrier	red	carrier	red	red	carrier	blue	carrier	red	carrier	red	carrier	red
Pulse length	0.51	0.55	0.96	0.57	0.84	0.58	2.88	1.47	1.15	3.02	2.31	4.69	2.31	0.72	0.58
Phase offset/π	0	1.50	1.00	0.50	0	1.50	$0 - \phi$	1.84	$1.59 + \phi$	1.47	$0.44 - \phi$	2.79	$1.68 - \phi$	1.87	$0.76 - \phi$

Table 5.2.1: Coherence state creation and certification pulse sequences for the superposition states indicated. The pulse length is defined as a fraction of a π-pulse on the ground state transitions, and the phase offset is given relative to the previous pulse. The free-evolution phase shift ϕ is applied between the creation and mapping pulses. The sequences were found by Jake Lishman.

5.2.3 Results

The 2-coherent states $(|1\rangle + |2\rangle)/\sqrt{2}$ and $(|1\rangle + |3\rangle)/\sqrt{2}$ were initially used to demonstrate the procedure of creating and certifying the coherence of arbitrary motional superpositions. These are the lowest excitation two element superpositions for which an inversion of the creation sequence does not produce full visibility interference patterns; states orthogonal to the target are not mapped onto the excited qubit state by the mapping which takes the target back to the ground state. The mapping sequences derived using the method discussed in section 5.2.2 are shown in table 5.2.1, and produce the full visibility interference patterns seen in fig. 5.2.4. Values of $C = 1.090(12)$ and $1.090(13)$ are obtained respectively from the certifier defined in eq. (5.2.2), above the 2-coherent threshold of 1, but, reassuringly, below the 3-coherent threshold that no 2-coherent state can achieve. While any oscillatory behaviour in an interference pattern implies coherence between at least two states, the certifier would not be able meet the 2-coherent threshold if the mapping was simply an inversion of the creation sequence for the 2-coherent states considered. This is expected as the certifier prioritises not returning a false positive over missing the presence of higher order coherence.

The main result of this work is the certification of 3-coherence in the lowest harmonic oscillator states of the ion using the single interference pattern shown in fig. 5.2.4. This gives a certifier value of $C = 1.54(2)$, well above the threshold of 1.25, and unequivocally showing the state as 3-coherent in the motional basis. As seen in fig. 5.2.3, the populations in the lowest oscillator states immediately after state creation are 38(3)%, 33(3)% and 29(3)% from the fit to eq. (5.2.6), implying the state creation sequence was imperfectly realised. Imperfections in the experimental sequence reduce the certifier value from the maximum theoretically achievable value of $C = 1.77$ [121]. The grey lines in fig. 5.2.4 show a numerical simulation which includes the off-resonant excitation of the carrier from sideband and Stark shift compensation pulses, which were described in section 4.4.5. These effects reduce the maximum value of the certifier as the Rabi frequency is increased, as seen in fig. 5.2.5 (c), however the sequence must be completed sufficiently fast such that qubit decoherence does not become detrimental. The frequency used, 90 kHz, is chosen to optimise these constraints, and limits the certifier value to $C = 1.69$ in simulations.

The model is not consistent with the measured data at the 1-σ level, and this is principally

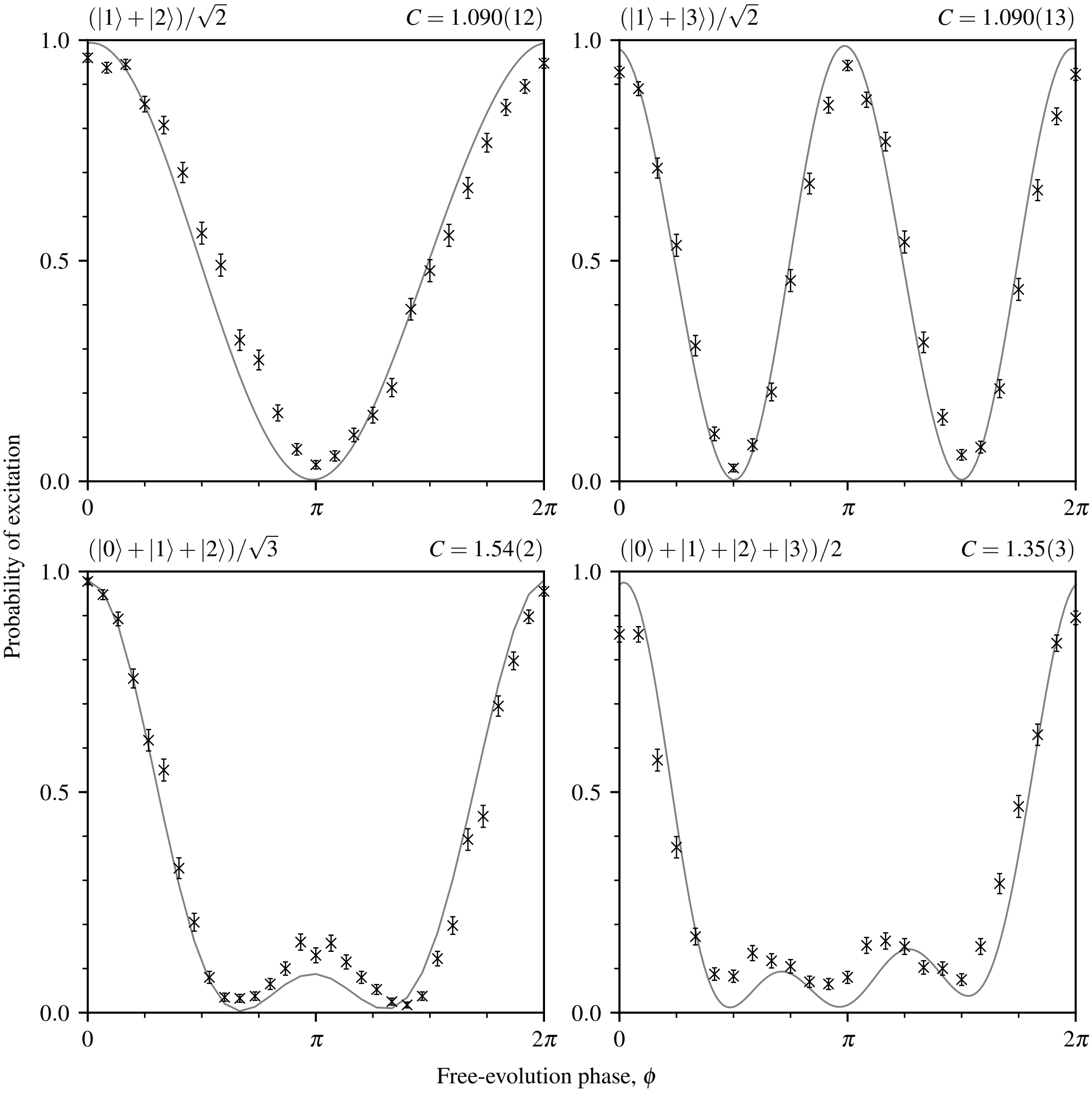

Figure 5.2.4: Interference patterns for coherence certification of 2, 3, and 4 coherent states, taken with a trap frequency of $\omega_z/2\pi = 1\,\mathrm{MHz}$ and a Rabi frequency on the carrier of $\Omega_0/2\pi = 90\,\mathrm{kHz}$. The plotted points (crosses) are the average of 400 shots each, and the solid line a theoretical model of the interference pattern using calibrated parameter values. The certifier C values are obtained by numerical integration of the data.

a result of detuning errors. The sensitivity of the certifier to carrier and trap detunings is shown in fig. 5.2.5 (a) and (b) for Rabi frequencies of 30 and 80 kHz. The initial detuning, and drift of the carrier coupling strength and frequency over the course of the experiment, reduces the certifier value, but high Rabi frequencies are less sensitive to these errors. Additionally any population not initially in the ground motional state will reduce the certifier value, as seen in fig. 5.2.5 (d). This is because the harmonic oscillator states have different sideband strengths, and the creation and mapping sequence is optimised for the initial state $|\downarrow, 0\rangle$. Fitting the model to the measured data by floating the initial motional state and the detunings from carrier and trap frequency over time is unreasonable, as different sources of error have a similar effect on the interference pattern. However this shows the clear advantage of this certifier, which unequivocally shows this state is 3-coherent despite the presence of uncontrollable sources of experimental error.

As the error in qubit rotations quickly compounds, and is further reduced by drift of the carrier, it was not possible to reach the 4-coherent threshold of 1.86, with a measured value of $C = 1.35(3)$. Off-resonant effects reduce the maximum obtainable value of the certifier to $C = 1.89$ in simulations, and all drift process are enhanced over the significantly longer sequence, as seen in fig. 5.2.5.

Discussion

Whilst any mapping operation $\mathcal{U}_m$ will not cause the certified value to increase above an incorrect threshold, there are physical mechanisms which may cause such an effect. Incoherent processes reduce the visibility of interference patterns, and consequently the certifier value, however this is not necessarily the case for time or phase dependent processes. The free evolution is achieved by varying the phase applied to sideband pulses in the mapping operation, with the phase and frequency set by the AWG. Each point in a scan is therefore of the same duration, and any error is not dependent on the magnitude of the applied shift. Implementation of the correct phase advancement is seen by the expected periodicity of the scans, and is verified independently. Furthermore any periodic drift is converted into white noise by randomising the order in which points are taken. Each plotted point in fig. 5.2.4 is composed of 4 scans of 100 shots, with the point order randomised on each scan.

Systematic miscalibration of experimental parameters, such as Stark shift compensation

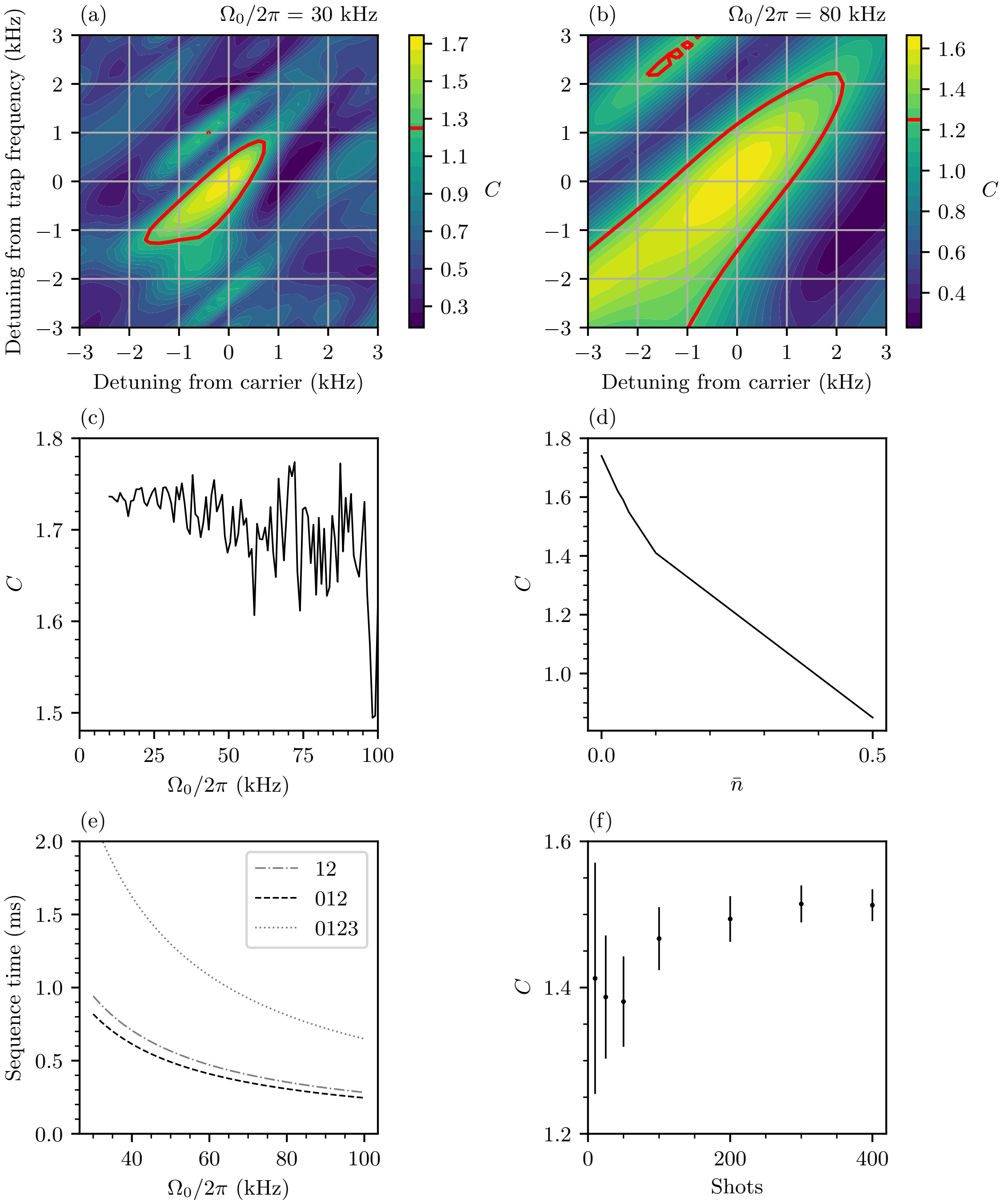

Figure 5.2.5: Mechanisms which reduce the maximum value that can be returned by the certifier. For the 3-coherent state contour plots (a) and (b) show the sensitivty of the certifier value to detuning errors for Rabi frequencies of 30 and 80 kHz. The red lines show the region above the 3-coherent threshold of 1.25. (c) Increasing the Rabi frequency however increases off-resonant excitation of the carrier, which reduces the certifier value. (d) An additional contribution to the reduction in the obtained value of C is the starting thermal state, simulated data from Jake Lishman. (e) The total time taken to complete the creation and mapping pulses is shown as a function of the carrier Rabi frequency. This highlights how much longer the 4-coherent verification sequence is. (f) Estimation of the certifier is also dependent on the statistical properties of the data. 400 shots are more than sufficient to give a reasonable error bound for the certifier. This plot shows the measured values of a certification phase scan. The effects shown in plots (a)-(d) combine to reduce the certifier value further than each acting independently, however as parameters drift over the course of an experiment, it is hard to predict an expected certifier value.

pulses or calibration of π times, can lead to an additional phase dependence of the measurement sequence. The calibration is checked by observing full visibility oscillations when driving the red and blue sidebands from $|\uparrow, 0\rangle$ and $|\downarrow, 0\rangle$ with the compensation pulses. It is also observed that any miscalibration tends to rapidly reduce the visibility of an interference pattern, and the certifier quickly drops below the target threshold. Drift of the carrier frequency requires constant recalibration, however it does mean that any coherent off-resonant processes, which contribute to the spikiness of fig. 5.2.5 (c), will be averaged out.

The certifier C uses low order moments, and therefore requires the probability to be sampled at fewer phase values than for higher order moments. Incomplete statistics can still alter the value of the certifier, which is reflected in the uncertainty of the measurement. A simple triangular integration of the moments will cause a systematic bias upwards, and this is addressed in ref [122]. As seen in fig. 5.2.5 (f), taking 400 shots gives a small error relative to the spacing of threshold values.

5.2.4 Conclusions

With this work the authors have shown that interference pattern experiments which extend the famous Ramsey experiment can verify the level of coherence present in the state of a quantum system. The technique is valid even if the measurement is performed on a basis that is coupled to the coherent basis of interest, enabling insight into systems that cannot otherwise be observed. This is the case for the harmonic motion of a trapped ion, which is coupled to the electronic qubit used to measure the state of the system. The ability to create higher order superpositions in the motion and to entangle qubits via shared modes is what enables an advantage in quantum technologies. This technique now allows critical information, the number of motional states that are coherently superimposed, to be extracted from the system using the most straightforward operations.

The main limitation in this particular experiment is from the fidelity of first order sideband rotations, which causes a build up of phase errors over time. These are increased further by drift in the carrier frequency over the experiment, as the laser used to address the optical qubit is locked to an external cavity. These are not fundamental limits in a trapped ion system, where single qubit gate errors of 1×10^{-6} are reported, and coherence times of 50 s [128]. Additionally a Raman qubit is far less subject to drift as the qubit frequency is derived from a frequency shift applied by an AOM, which is very stable. It is therefore conceivable that much higher levels of coherence can be created and certified in the motion of trapped ions, and this work presents the initial proof of principle. The technique is also applicable to other quantum systems where the state is not accessible to measurement fields, such as in cavity optomechanics, and is therefore of wider utility. A final advantage is that the method is robust in the face of imperfect implementation, and is therefore well suited to current noisy intermediate scale devices.

Chapter 6

Outlook

This thesis has described the initial development of a new ion trapping system, which has replaced the Imperial Penning trap after many years of reliable operation. The first experiment in the rf trap was presented in the previous chapter, and shows a high level of control over the motional states of a single ion. This concludes the first phase of the project, and attention can now be turned to characterising and reducing the remaining sources of noise, discussed in section 6.1, and to the main focus of the project. This is, initially, to show proof-of-principle improvements in the fidelity of two-qubit gates outside the Lamb–Dicke regime, and a brief discussion of further experimental requirements is given in section 6.2.

6.1 Linear Paul Trap Development

Establishing the new ion trap initially required the design of electrodes and vacuum system, which maintains the UHV regime. In addition to this the laser optical systems and experimental control were replaced, which enable complex experiments to be built with simple scripts. This provides a good platform for further development of the experimental apparatus in order to engineer more exotic interactions. Much work can be done on the stabilisation of laser, electric, and magnetic fields, which limit the fidelity of state preparation, readout, and qubit manipulation to the 99% level. Further development in the control of laser fields can also help to suppress an array of environmental noise sources, and is a useful area to investigate for the control of noisy quantum systems.

Laser Power Stabilisation

The power of any laser at the ion is affected by both drift in the absolute power and the polarisation, which is converted into power noise by polarising optics. The power and polarisation fluctuate primarily due to thermal expansion of the fibres, and is minimised by aligning the laser field and polarisation-maintaining fibre axes. There is still however a slow drift observed on the photodiode monitoring the spectroscopy laser, which could be fed back to the amplitude of the rf signal sent to the AOM in order to stabilise the laser on medium to long timescales. A function running on the FPGA would be able to correct for any power drift between points, and potentially between shots. Continuous power stabilisation is only possible before the AOM, and therefore before a second fibre, but would reduce faster noise.

Laser Frequency Stabilisation

A limiting factor in the ability to perform repeated operations with high fidelity is the drift of the spectroscopy laser cavity, which means transitions are driven off-resonantly. The time needed for calibration of the carrier frequency could be reduced from $\approx 1\,\mathrm{min}$ by extracting the same information from fewer shots, in order to be used during scans. Estimation of the excitation probability with Wilson's modification gives more accurate results from less data, and it would be interesting to investigate the minimum number of points required to define the peak at the sub-kHz level. This laser is required for state readout, whatever operations are performed, and drift will limit the fidelity of ion shelving.

A separate concern are the servo bumps, seen in the locking signal in fig. 4.1.4, which implies the laser includes frequency components at this position. This is seen by excitation of the ion at the frequency of the servo bumps, typically 400 to 700 kHz, and this unaccounted for excitation limits the fidelity of logic pulses.

Electromagnetic Field Stabilisation

The dc electric fields used in axial trapping and radial compensation are passively filtered, and no significant drift is observed in the magnitude of the applied voltages. The axial voltage is produced by a high stability power supply, however the dynamic potential applied to two of the radial blades leads to rf pickup on the other electrodes. Although these are rf grounded, oscillation is observed in the voltage at endcap electrodes, and this may be a cause of axial motional heating.

Noise in the quantisation field at the ion is the leading cause of optical decoherence, as the coherence time is shown to be reduced in qubits that are more sensitive to the magnitude of the field through Zeeman splitting. This is a fundamental limitation of this isotope of calcium, as the frequency separation of the states in both optical and Raman qubits depend linearly on the magnetic field magnitude. Without the ability to make the ion less sensitive to the environment, a key area of investigation is the fast magnetic field noise which leads to decoherence. Drift of the magnetic field over the mains period at 50 Hz is observed through its effect on the qubit carrier frequency, and the development of passive or active cancellation could reduce this measurable shift. However as this process does not randomise the additional phase gained in the interaction, in theory this is not the leading cause of optical decoherence.

Arbitrary Control Fields

The high frequency off-resonant excitation of the carrier during first order red and blue sideband pulses can mean the desired qubit rotation is not achieved. By ramping the power of the interaction laser up and down, whilst fixing the pulse area, off-resonant effects are suppressed at the start and end of pulses, and the pulse area can be more accurately enclosed. In the coherence experiments presented in chapter 5, this pulse shaping did not reliably increase the certifier values obtained. However, while beyond the scope of this thesis, the ability to arbitrarily control the power, frequency components, and phase of the laser field using the AWG can account for any number of known sources of error, and will hopefully lead to exciting developments in the control of quantum systems.

6.2 Towards Robust Two-qubit Gates

All two qubit gates that are implemented in trapped ions require cooling of the bus mode that mediates the entanglement into the Lamb–Dicke (LD) regime. This results in simplified dynamics, meaning, for example, that the Mølmer–Sørensen entangling interaction can be engineered by a driving field with two frequency components at a fixed detuning from the red and blue sidebands. The higher order terms in the qubit motional coupling outside the LD regime reduce the fidelity of the gate as they are not accounted for, and gates are therefore driven weakly to preserve the validity of the LD approximation. In a recent proposal [46], it has been shown that high fidelity entangling gates can be achieved outside the LD regime, where the coupling between qubit and motional states is far stronger. This means gates can potentially be performed faster, and with motional states of the ion obtained after Doppler cooling. The higher order effects outside the LD regime are compensated by adding frequency components to the driving field detuned from the second order red and blue sidebands, which squeeze the motional state in phase space. This is again possible by the design of arbitrary laser fields with the AWG.

To show this experimentally it is necessary to increase the relative coupling strength of the ions to their shared motion. The strength of motional sidebands relative to the carrier transition is characterised by the LD parameter. This is dependent on the trap frequency ω and the wavevector k of the interaction laser,

$$\eta = k\cos(\theta)\sqrt{\frac{\hbar}{2NM\omega}}, \tag{6.2.1}$$

for N ions. The angle $\theta = 0$ is fixed by the requirement of projecting onto only the axial motion, limiting our interaction with the noisier radial motion, and maximising η. The scaling of the LD parameter for the optical qubit used in the multi-level coherence experiments is shown in fig. 6.2.1 (left), giving $\eta \approx 0.1$ for a mode frequency of 1 MHz with 1 ion. There is a limit to how far the trap frequency can be reduced to increase the LD parameter, however it is possible to increase the magnitude of the k-vector by reducing the wavelength of the light.

6.2.1 A Raman Qubit

The lower energy photons which excite the optical qubit are not well suited to investigating the strong coupling regime. A Raman interaction however imparts more momentum to the ion with high energy blue photons, as shown in fig. 6.2.1 (right), where the qubit states are mapped onto the two ground states $\mathrm{S}_{1/2,\pm1/2}$. These are coupled by two beams, derived from the same laser, which stimulate a two-photon transition between the ground state qubit levels if $\delta_1 = \delta_2$. This implies the frequency difference $\nu_1 - \nu_2$ is equal to the spacing between qubit levels. In the process a photon from the first laser field virtually excites the ion, and is emitted into the second laser field, with the magnitude of the detunings large

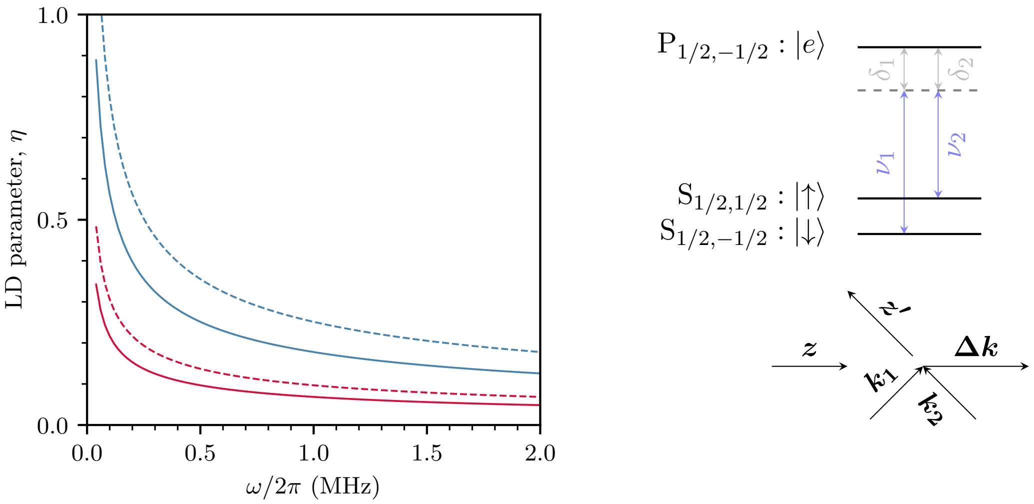

Figure 6.2.1: Scaling of the LD parameter with harmonic oscillator frequency ω (left). The Raman qubit (blue) has a larger η than the optical qubit (red) at the same trapping frequency, as more momentum is transferred to the ion on excitation of the qubit. The scaling is also shown for 1 (dashed) and 2 (solid) ions, where more ions reduces η. (right) Definition of parameters in Raman scheme. The laser wavevectors are viewed from the same angle as fig. 4.1.1, with the two Raman beams entering from the South–East and North–East viewports, and the effective wavevector aligned with the z-axis of the trap $\boldsymbol{z}$ (whereas $\boldsymbol{z'}$ is the quantisation axis).

such that the excited state $|e\rangle$ is not populated. The effective wavevector is given by the difference between absorbed and emitted wavevectors

$$\boldsymbol{\Delta k} = \boldsymbol{k_1} - \boldsymbol{k_2}. \tag{6.2.2}$$

This further increases η, which means stronger coupling between qubit and motion.

Another benefit of the Raman qubit is that the interaction frequency is derived by shifting one component of the same laser with an AOM. As the rf frequency applied is very stable, drift in the carrier transition can only be caused by the magnetic field.

6.2.2 Multiple Ions

Experiments with more than a single ion have not been presented in this thesis, and working with multiple ions will require modification to laser cooling and state manipulation techniques. Additionally, the same amount of information is obtained from the imaging camera and the number of PMT counts when measuring the state of a single ion; was it bright or not? With two ions, it is only possible to discriminate between zero, one, or two bright ions using the PMT, and so using the imaging camera is necessary to determine which of the ions was bright.

Appendices

Appendix A

Table of Parts

A large amount of new equipment has been purchased since the last Imperial Ion Trapping thesis. The following, whilst not exclusive, is an attempt to document the most significant items.

Part	**Supplier**	**Model**
	Vacuum System	
Chamber	Kimball/Scanwel	MCF600-SphOct-F2C8
Side viewport[i]	Lewvac	FSVP-UV-40CF
Re-entrant viewport[ii]	Lewvac	FSVP-UV-100CFRE
Base flange (fig. B.3)	Lewvac	FL-100CFL, FHP1-C8-W
Rf feedthrough	Lewvac	FHP5-50C4-40CF
Tee pieces	Lewvac	FL-T40CF
All metal valve	Lewvac	AVM40CF
Ion gauge filament	Agilent	9715014
Ion gauge controller	Agilent	XGS600H1M0C0
Ion pump	SAES	NEXTorr z100 5H0211
Ion pump power supply	SAES	NEXTorr 3B0408

---

[i] Anti-reflection coated on both sides [$\perp$: per surface, $R < 0.25\%$ @ 397 nm; $\approx 6.5\%$ above 700 nm].

[ii] AR coated on vacuum side. Modification shown in fig. B.4.

Part	**Supplier**	**Model**
	Power Supplies	
Endcaps	BK Precision	BK9185B
Compensation electrodes	RS	RS-3005P
Rf amplifier	ENI	325LA
Main coil	TTi	PL303QMD
Shim coils	Tenma	72-2550
	Laser Systems	
Wavemeter	HighFinesse	WS8-10
PI laser controller	Tui Optics	DC 100
375 laser/diode	Tui Optics/Nichia	DL 100, NDU4116
423 laser/diode	Tui Optics/Nichia	DL 100, NDV4A16
Diode laser controller	Toptica	DLC pro+
397 lasers	Toptica	DL pro HP 397
854, 866 lasers	Toptica	DL pro 850
AOM1,AOM2	G&H/pro-lite	AOMO 3080-120
AOM3	G&H/pro-lite	AOMO 3080-122
729 laser	Toptica	DL pro 729
729 locking electronics	Toptica	FALC 110
729 EOM	Photonics Technologies	EOM-02-25-V
Tapered amplifier (TA)	Moglabs	MOAL-002
AOM4	AA Opto-Electronics	MT200-B100A0,5-800
AWG	Keysight	P9336A
	Imaging System	
EMCCD camera	Andor	iXon Ultra 897
PMT	Hamamatsu	H11870-01
	Experimental Control Hardware	
FPGA	Sinara	Kasli
DDS	Sinara	Urukul
DIO	Sinara	
AIO	Sinara	

Table A.1: List of parts.

Appendix B

Technical Drawings

This appendix is intended to give sufficient detail for future modification of the trap and vacuum system, and other significant parts. A large number of components have been manufactured by Brian over the course of this project. Additionally several commercial items have been modified by the manufacturer to our specifications. All parts are shown in-situ in the SolidWorks assemblies, with technical drawings of the trap shown here.

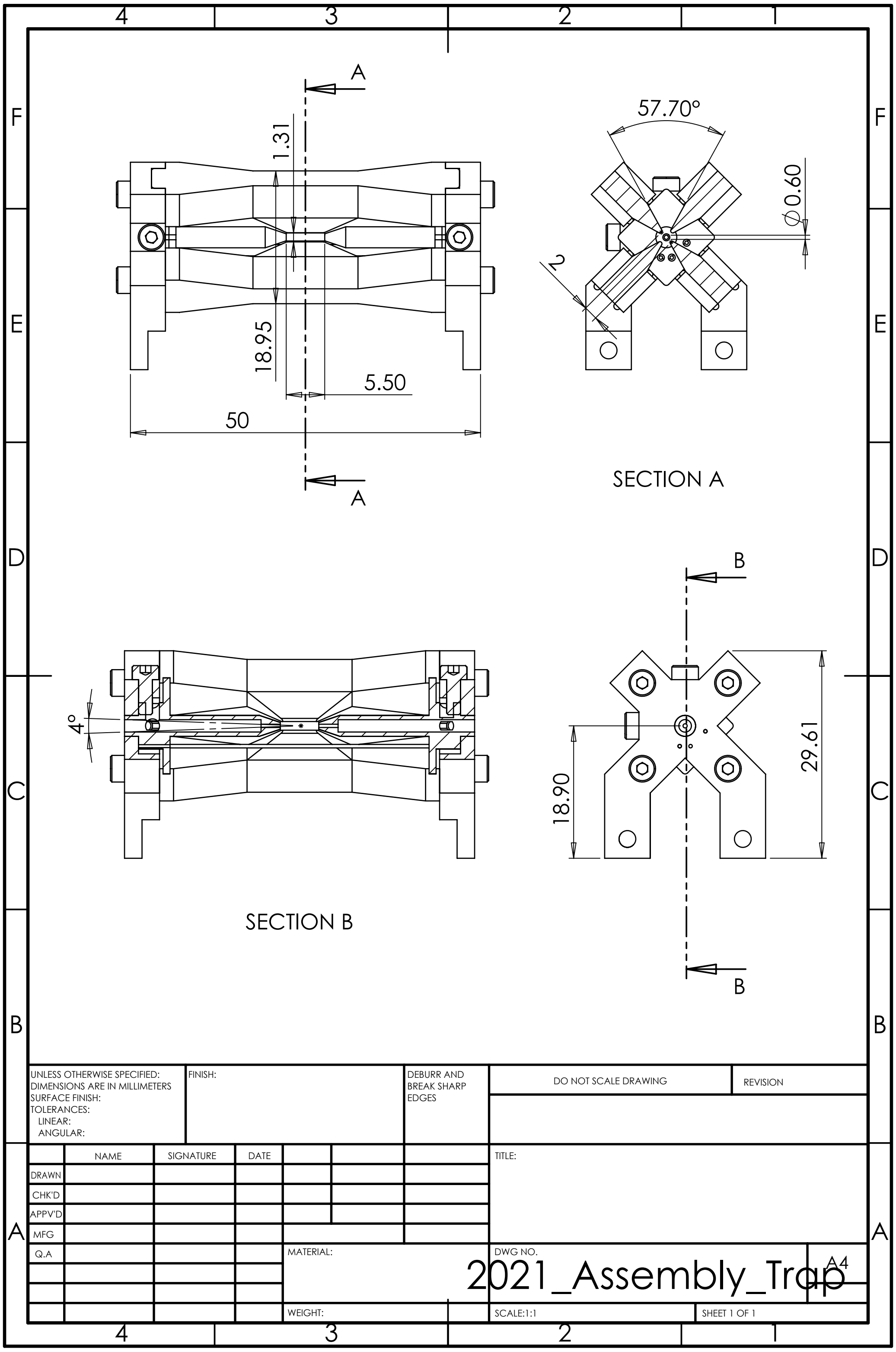

Figure B.1: Technical drawing of trap assembly. Units in mm.

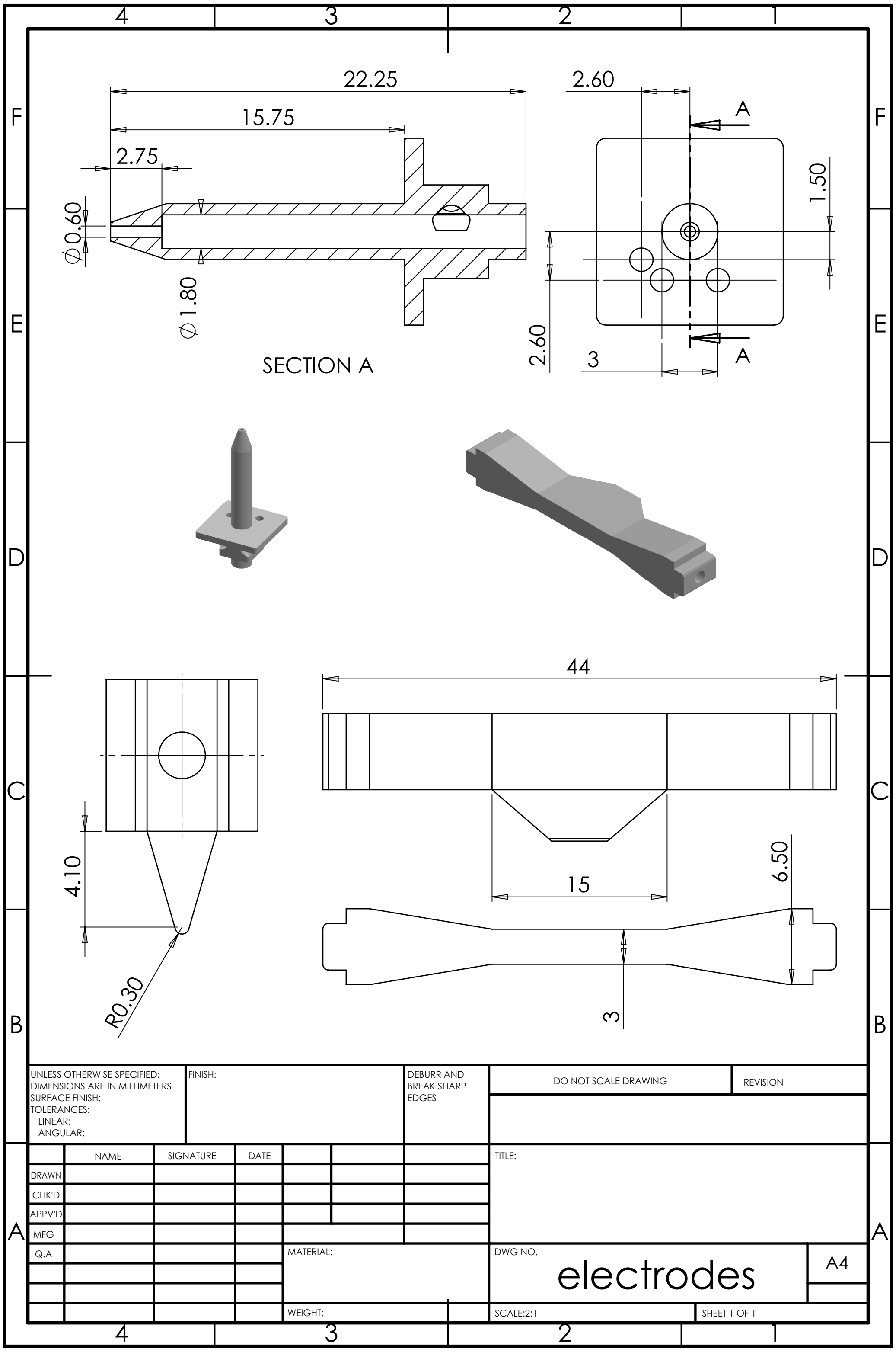

Figure B.2: Technical drawing of radial blade and axial endcap electrodes. Units in mm.

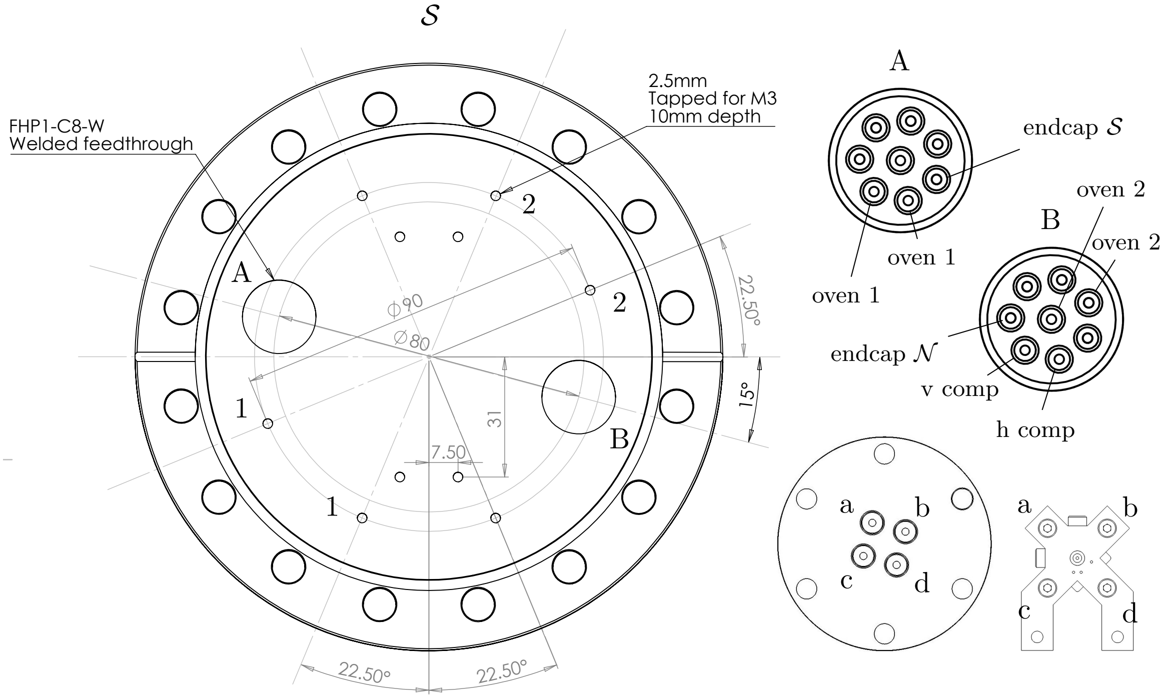

Figure B.3: Modified base flange FL-100CFL, with FHP1-C8-W dc feedthroughs (A and B) and tapped holes for attaching trap support and ovens. Drawing provided to manufacturer. Units in mm. The supports for ovens 1 and 2 are attached to the numbered tapped holes, and wired to the indicated dc feedthroughs. The endcap and compensation voltages are also connected through feedthroughts A and B. The rf feedthrough is wired on the inside to the south end of the trap as shown, where the feedthrough is viewed from the east and the trap south.

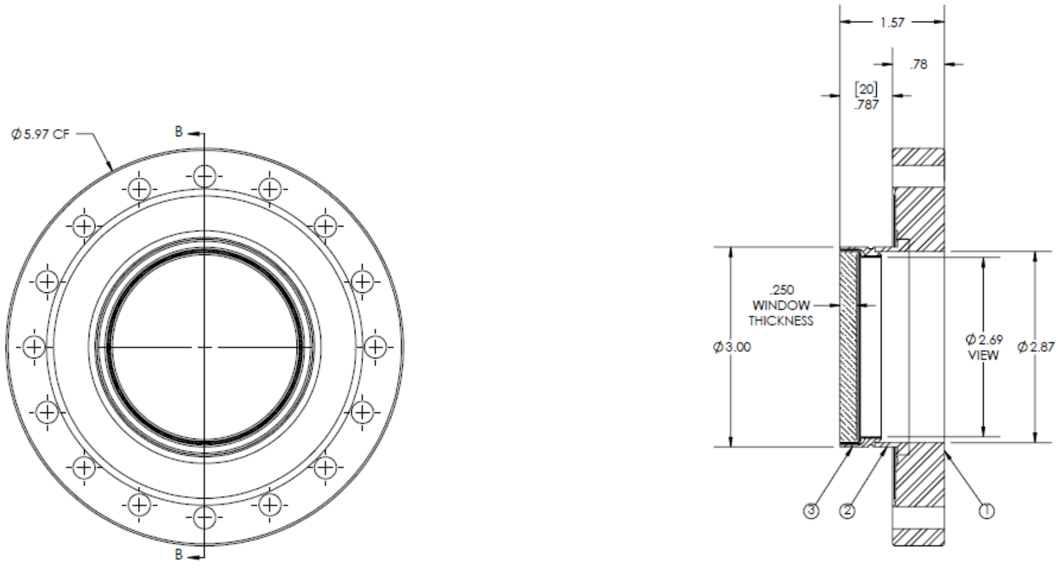

Figure B.4: Modified re-entrant viewport FSVP-UV-100CFRE. Drawing provided by manufacturer, depth (dimension *c* in part drawing) modified to 20 mm. Units in inches.

Appendix C

Line Trigger Circuit Diagram

The circuit diagram of the line trigger is shown in fig. C.1. The voltage is dropped down by a transformer. Due to forward biasing, the voltage after the diode is only positive, leading to a series of peaks at the mains frequency. The potential divider drops the amplitude of these peaks for input to the Schmitt-trigger, which gives a pulsed output whenever the voltage crosses a threshold. A part of the mains voltage is converted into a stable dc supply at 5 V which powers the Schmitt-trigger.

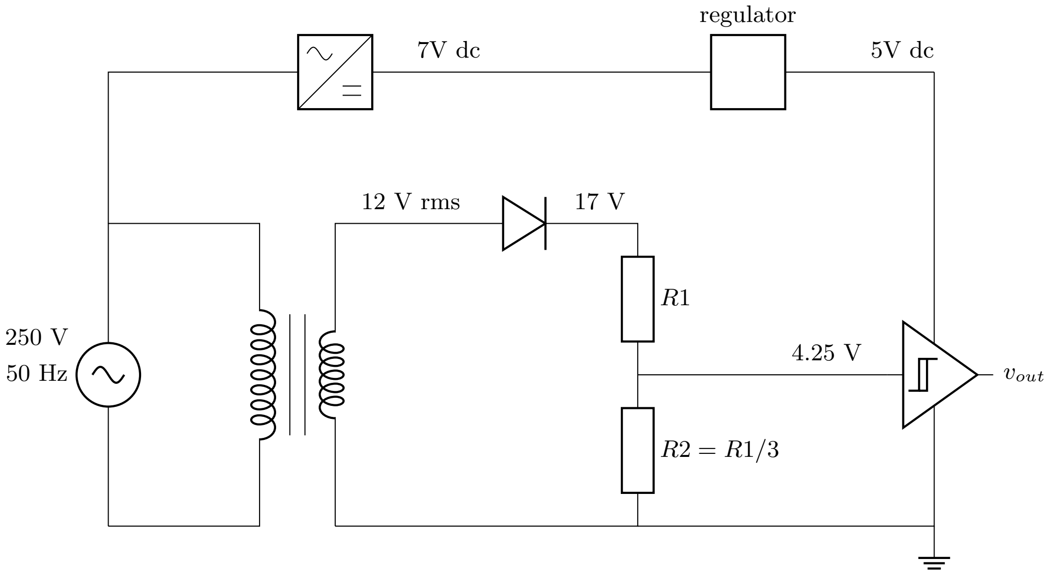

Figure C.1: Line trigger circuit diagram. The mains voltage is stepped down to 12 V rms, with a maximum amplitude of 17 V. This is reduced to a safe level for the Schmitt-trigger by a potential divider. The Schmitt-trigger produces a 5 V ttl pulse v_{out} on the rising edge of the mains cycle. The chip is also powered by the mains voltage with an ac-dc converter.

Appendix D

Code

D.1 Script for Plotting and Fitting Frequency Spectra

Listing D.1: Python code for fitting sideband cooled spectra with interaction model.

```python
import numpy as np
import matplotlib.pyplot as plt
import scipy.optimize as opt
import scipy.stats

from importlib import reload
import sideband_model_v2 as sm
reload(sm)

from plot_functions_v2 import plot_freq

from datetime import datetime


#--------------------------------------------------------------------------------#
#---------------------- IMPORT DATA
"""
DATA RIDS

13826 - rsb
13827 - bsb
13828 - carrier
13829 - full spec
"""


#--------------------------------------------------------------------
#--------------------------------------------------------------------

rids = [13829, 13826, 13827, 13828]

freqs , probs , errors , params = plot_freq(rids[0], 20)
freqs_rsb , probs_rsb , errors_rsb , _ = plot_freq(rids[1], 20)
freqs_bsb , probs_bsb , errors_bsb , _ = plot_freq(rids[2], 20)
freqs_car , probs_car , errors_car , _ = plot_freq(rids[3], 20)

fs_array = np.concatenate((freqs[3:50],freqs[60:-3],freqs_rsb ,freqs_bsb ,freqs_car))
ps_array = np.concatenate((probs[3:50],probs[60:-3],probs_rsb ,probs_bsb ,probs_car))
es_array = np.concatenate((errors[3:50],errors[60:-3],errors_rsb ,errors_bsb ,errors_car))

print(f'imported RID(s): {rids}. ')


#--------------------------------------------------------------------
#---------------------- MODEL CLASS - Set Rabi , trap freq , and nbar
#---------------------- Debug plots thermal dist and sb strengths
start_t = datetime.now()
current_time = start_t.strftime("%H:%M:%S")
```

```
print("Start time: ", current_time)

Rabi = 2*np.pi*36e3
trap = 2*np.pi*1.08e6
nbar = 0.02

mod = sm.Interaction(trap,nbar,Rabi,nmax=20,debug=False)

mod_t = datetime.now() - start_t
current_time = mod_t.total_seconds()
print(f"Interaction model created: ", current_time, "s")


#---------------------------------------------------------------------
#---------------------- TEST SPECTRUM FROM MODEL

fs = np.linspace(-1.2*(2*np.pi)*1e6, 1.2*(2*np.pi)*1e6, 5001)
probe = 145e-6
x_off = 0
y_off = 0.003
spec_start = datetime.now()

probs = mod.ex_spec(fs,probe,x_off,y_off)

spec_time = datetime.now() - spec_start
current_time = spec_time.total_seconds()
print("Spectrum created: ", current_time, "s")


#-------------------------------------------------------------------------------#
#---------------------- FITTED MODEL

def fit_mod(f,x_off,y_off,nbar,Rabi,trap):
    #t from this data set
    t = 145e-6
    f_mod = sm.Interaction(trap,nbar,Rabi)
    return f_mod.ex_spec(f,t,x_off,y_off)

p0 = [0,0,nbar,Rabi,trap]
bounds = [[-1e5,0,0,Rabi*0.1,trap*0.99],
            [1e5,0.1,5,Rabi*10,trap*1.01]]

popt, pcov = opt.curve_fit(fit_mod,fs_array*2*np.pi,ps_array,p0=p0,bounds=bounds,
                sigma=es_array,absolute_sigma=True)
perr = np.sqrt(np.diag(pcov))

print(f"""\
FIT RESULTS
f0            : {round(popt[0]/(2*np.pi))/1e3} ({round(perr[0]/(2*np.pi))/1e3}) kHz
background    : {round(popt[1],3)} ({round(perr[1],3)})
nbar          : {round(popt[2],3)} ({round(perr[2],3)})
Om            : {round(popt[3]/(2*np.pi))/1e3} ({round(perr[3]/(2*np.pi))/1e3}) kHz
om            : {round(popt[4]/(2*np.pi))/1e3} ({round(perr[4]/(2*np.pi))/1e3}) kHz""")

#np.save('sbc_fit',popt)
#np.save('sbc_fit_errors',perr)


#---------------------------------------------------------------------
#---------------------- PLOT FITTED SPECTRUM
sm.Interaction(popt[4],popt[2],popt[3],nmax=20,debug=False)

fig_f = plt.figure(constrained_layout=True)
gs = fig_f.add_gridspec(4,1)

cs = ['grey','crimson','k','steelblue']
for i in range(4):

    ax_f = fig_f.add_subplot(gs[i,0])
    ax_f.errorbar(fs_array/1e3, ps_array, yerr=es_array, fmt='x',color='k',ms=4,mew=0.5,
                elinewidth=0.5,capsize=1,zorder=0)
    ax_f.plot(fs/(2*np.pi)/1e3,fit_mod(fs,*popt),c=cs[i],linewidth=0.7)

    ax_f.set_ylim(0,1)
    ax_f.set_yticks([0,0.5,1])

    if i == 0:
        ax_f.set_xlim(-1200,1200)

    elif i == 1:
        ax_f.set_xlim(-1105,-1050)
        ax_f.set_xticks([-1100,-1080,-1060])
```

```
        ax_f.set_ylim(0,0.05)
        ax_f.set_yticks([0,0.05])

    elif i == 2:
        ax_f.set_xlim(-100,100)
        ax_f.set_xticks([-100,-50,0,50,100])

    elif i == 3:
        ax_f.set_xlim(1050,1105)
        ax_f.set_xticks([1060,1080,1100])

    ax_f.minorticks_on()

fig_f.supxlabel('Detuning from Carrier (kHz)')
fig_f.supylabel('Probability of Excitation')

#fig_f.savefig('sbc_spectrum.pdf')
plt.show()
```

D.2 Interaction Model Class

Listing D.2: Python class for interaction model used in data fitting.

```
import numpy as np
import scipy.special as sp
import matplotlib.pyplot as plt
from matplotlib.offsetbox import AnchoredText

hbar = 1.055e-34

class Interaction:
    """
    Class for modelling qubit--motion interaction dynamics.
    """
    def __init__(self,om,nbar,Om0,theta=0,k=1,nmax=250,debug=False):
        """
        om: trap frequency (angular)
        Om0: base rabi freq (angular)

        nbar: nbar
        nmax: sum over thermal dist nbar from n=0 to n=nmax.

        theta: angle between k-vector and motional axis.

        k:  Number of sidebands to precompute normalised Rabi frequencies.
            k = 0: carrier only
            k = 1: carrier and first order sbs
            k = 2: carrier, first, and second order sbs

        debug:  Plot sideband strengths from n to nmax for k sidebands.
                Plot thermal distribution nbar.
        """
        self._debug = debug
        self._om = om
        self._eta = self.get_LDpar(theta=theta)
        self._k = k
        self._Om0 = Om0
        self._nbar = nbar
        self._nmax = nmax

        #calculate coupling strengths as function of initial n state for k sbs.
        #precomputation massively speeds up class creation.
        #define empty arrays
        self.carrier_rabi_n = np.zeros(self._nmax)
        self.red_rabi_n = np.zeros(self._nmax)
```

```
        self.blue_rabi_n = np.zeros(self._nmax)
        self.red2_rabi_n = np.zeros(self._nmax)
        self.blue2_rabi_n = np.zeros(self._nmax)

        self.thermal_dist_n = np.zeros(self._nmax)

        for n in range(self._nmax):
            self.carrier_rabi_n[n] = self.Om_n_m(n,0)
            self.thermal_dist_n[n] = self.get_therm_dist(n)

        if self._k == 1:
            for n in range(self._nmax):
                self.red_rabi_n[n] = self.Om_n_m(n,-1)
                self.blue_rabi_n[n] = self.Om_n_m(n,1)

        if self._k == 2:
            for n in range(self._nmax):
                self.red_rabi_n[n] = self.Om_n_m(n,-1)
                self.blue_rabi_n[n] = self.Om_n_m(n,1)
                self.red2_rabi_n[n] = self.Om_n_m(n,-2)
                self.blue2_rabi_n[n] = self.Om_n_m(n,2)

        if self._debug == True:

            label = AnchoredText(f'''
                    Om0:    {round(self._Om0/(2*np.pi))/1e3} kHz
                    om:     {round(self._om/(2*np.pi))/1e3} kHz
                    nbar:   {round(self._nbar,3)}

                    eta:    {round(self._eta,3)}
                    ''',loc=1)

            fig0 = plt.figure()
            ax0 = fig0.add_subplot(111)

            ax0.plot(self.carrier_rabi_n/self._Om0,'k-')
            ax0.plot(self.red_rabi_n/self._Om0,'r-')
            ax0.plot(self.blue_rabi_n/self._Om0,'b-')
            ax0.bar(np.arange(0,nmax,1),self.thermal_dist_n ,color='grey')

            ax0.set_xlabel('n')
            ax0.set_ylabel('normalised strength')

            ax0.add_artist(label)
            plt.show(block=False)

    def Om_n_m(self ,n,m):
        """
        Caclculate modified rabi freq between state n and n+m

        t1: exp^-eta^2/2
        t2: eta^abs(m)
        t3: sqrt[min(n,n+m)!/max(n,n+m)!]
        t4: Laguerre (eta^2,min(n,n+m),abs(m))
        """
        t1 = np.exp(-self._eta**2/2)
        t2 = self._eta**np.abs(m)

        #sp.factorial is very slow and limited to 170!
        #conditional statements enable much faster computation of t3 for |m| < 3
        if m >= 0:
            if m == 0:
```

```python
                t3a = 1
            elif m == 1:
                t3a = np.sqrt(1/(n+1))
            elif m == 2:
                t3a = np.sqrt(1/((n+1)*(n+2)))
            elif m > 2 and n < 150:
                nf = sp.factorial(n)
                nmf = sp.factorial(n+m)
                t3a = np.sqrt(nf/nmf)
            else:
                raise ValueError('sum is limited to 150 for |m| > 2')

            t3 = t3a
            t4 = np.abs(sp.assoc_laguerre(self._eta**2,n,np.abs(m)))

        else:
            if m == -1:
                if n == 0:
                    t3a = 1
                else:
                    t3a = np.sqrt(1/n)
            elif m == -2:
                if n == 0 or n == 1:
                    t3a = 1
                else:
                    t3a = np.sqrt(1/(n*(n-1)))
            elif m < -2 & n < 150:
                nf = sp.factorial(n)
                nmf = sp.factorial(n+m)
                t3a = np.sqrt(nmf/nf)
            else:
                raise ValueError('sum is limited to 150 for |m| > 2')

            t3 = t3a
            t4 = np.abs(sp.assoc_laguerre(self._eta**2,n+m,np.abs(m)))

        return self._Om0*t1*t2*t3*t4

    def get_LDpar(self,lam=729e-9,theta=0,m=6.655e-26):
        """
        Caclculate LD param from motional freq and photon wavelength
        om: angular trap frequency
        lam: interaction laser wavelength
        theta: angle between laser and oscillation axis
        """
        k = 2*np.pi/lam *np.cos(theta)
        return k*np.sqrt(hbar/(2*m*self._om))

    def get_therm_dist(self,n):
        """
        Return occupation probability of state n for thermal dist, nbar.
        """
        therm_ratio = self._nbar/(self._nbar+1)
        return therm_ratio**n/(self._nbar+1)

    def prob_ex_m(self,m,t,delta):
        """
        probability of excitation on sb m
        takes probe time t and detuning delta

        limited to |m| < 3
        """
```

```python

        prob = 0

        for n in range(self._nmax):
            if m == 0:
                Om = self.carrier_rabi_n[n]
            elif m == -1:
                Om = self.red_rabi_n[n]
            elif m == 1:
                Om = self.blue_rabi_n[n]
            elif m == -2:
                Om = self.red2_rabi_n[n]
            elif m == 2:
                Om = self.blue2_rabi_n[n]
            else:
                print('m = -2,-1,0,1,2')

            therm_weight = self.thermal_dist_n[n]

            Om_s = Om**2
            Om_delta_s = Om_s + delta**2
            Om_ratio = Om_s / Om_delta_s

            Om_r = np.where(np.isnan(Om_ratio), 1, Om_ratio)

            p_e_sq =  therm_weight * Om_r * np.sin(np.sqrt(Om_delta_s)/2*t)**2
            prob += p_e_sq

        return prob

    def ex_spec(self,f,t,x_off,y_off):
        """
        Returns excitation spectrum over k order sidebands, range fs
        function of probe time, t
        order of sidebands, k   ---  default = 1 (r,c,b)
        k = 2    --- (r2,r,c,b,b2)
        """

        freq = f - x_off

        carrier_prob = self.prob_ex_m(0,t,freq)
        red_prob = self.prob_ex_m(-1,t,freq+self._om)
        blue_prob = self.prob_ex_m(1,t,freq-self._om)
        probs = carrier_prob + red_prob + blue_prob

        if self._k == 2:
            red2_prob = self.prob_ex_m(-2,t,freq+2*self._om)
            blue2_prob = self.prob_ex_m(2,t,freq-2*self._om)

            probs += red2_prob + blue2_prob




        probs = (1-y_off) * (probs + y_off)

        return probs


    def probe_m(self,m,t_lim=1e-3,npoints=1001):
        """
        Returns time scan on sideband m
```

```python

        """
        times = np.linspace(0,t_lim,npoints)
        probs = np.zeros(npoints)
        for t in range(npoints):
            probs[t] = self.prob_ex_m(m,times[t],0)

        return times, probs
```

D.3 Data Plotting Functions

Listing D.3: Python functions for plotting data files.

```python
from load_h5 import load_h5
import numpy as np
import matplotlib.pyplot as plt



def plot_time(rid,threshold=-1):
    '''load time scan'''

    data, metadata = load_h5(rid)

    params = metadata['params']
    time = data['scan.time']

    #counts after probe
    countsA = data['scan.countsA']
    #counts during cool
    countsB = data['scan.countsB']

    nsteps = sum(np.isfinite(time))
    nruns = countsA.shape[1]

    if threshold == -1:
        t_count = params['threshold']

    else:
        t_count = threshold

    n_bright = np.sum(countsA[:nsteps,:] > t_count,1)
    n_dark = np.sum(countsA[:nsteps,:] <= t_count,1)

    #set cooling threshold , prob_bright during cool > 0.11
    pr_br_B = np.sum(countsB[:nsteps,:] <= t_count,1)/nruns
    n_bright[np.where(pr_br_B > 0.15) [0]] = 0
    n_dark[np.where(pr_br_B > 0.15) [0]] = 0


    #normal approximation
    #p_ex = n_dark/nruns

    #normal 95% confidence interval
    z = 1.96
    #error = z/nruns * np.sqrt(n_dark*n_bright/nruns)

    #wilson score
    p_ex = (n_dark + 0.5*z**2)/(nruns + z**2)

```

```
    errors = z/(nruns + z**2) * np.sqrt(n_dark*n_bright/nruns + z**4/4)



    times = time[:len(p_ex)]
    probs = p_ex



    return times, probs, errors, params

def plot_phase(rid,threshold=-1):
    '''load phase scan'''

    data, metadata = load_h5(rid)

    params = metadata['params']
    phase = -1*data['scan.phase']

    #counts after probe
    countsA = data['scan.countsA']
    #counts during cool
    countsB = data['scan.countsB']

    nsteps = sum(np.isfinite(time))
    nruns = countsA.shape[1]

    if threshold == -1:
        t_count = params['threshold']

    else:
        t_count = threshold

    n_bright = np.sum(countsA[:nsteps,:] > t_count,1)
    n_dark = np.sum(countsA[:nsteps,:] <= t_count,1)

    #set cooling threshold , prob_bright during cool > 0.11
    pr_br_B = np.sum(countsB[:nsteps,:] <= t_count,1)/nruns
    n_bright[np.where(pr_br_B > 0.11) [0]] = 0
    n_dark[np.where(pr_br_B > 0.11) [0]] = 0


    #normal approximation
    #p_ex = n_dark/nruns

    #normal 95% confidence interval
    z = 1.96
    #error = z/nruns * np.sqrt(n_dark*n_bright/nruns)

    #wilson score
    p_ex = (n_dark + 0.5*z**2)/(nruns + z**2)

    errors = z/(nruns + z**2) * np.sqrt(n_dark*n_bright/nruns + z**4/4)



    phases = phase[:len(p_ex)]
    probs = p_ex



    return phases, probs, errors, params
```

```
def plot_freq(rid,threshold=-1,normalise_freqs = True):
    '''load frequency scan'''

    data, metadata = load_h5(rid)

    params = metadata['params']
    freq = data['scan.freq']

    if normalise_freqs == True:
        car_base_freq = params['car_freq']
        freq = -1 * (freq - car_base_freq)

    #counts after probe
    countsA = data['scan.countsA']
    #counts during cool
    countsB = data['scan.countsB']

    nsteps = sum(np.isfinite(freq))
    nruns = countsA.shape[1]

    if threshold == -1:
        t_count = params['threshold']

    else:
        t_count = threshold


    n_bright = np.sum(countsA[:nsteps,:] > t_count,1)
    n_dark = np.sum(countsA[:nsteps,:] <= t_count,1)

    #set cooling threshold , prob_bright during cool > 0.11
    pr_br_B = np.sum(countsB[:nsteps,:] <= t_count,1)/nruns
    n_bright[np.where(pr_br_B > 0.11) [0]] = 0
    n_dark[np.where(pr_br_B > 0.11) [0]] = 0


    #normal approximation
    #p_ex = n_dark/nruns

    #normal 95% confidence interval
    z = 1.96
    #error = z/nruns * np.sqrt(n_dark*n_bright/nruns)

    #wilson score
    p_ex = (n_dark + 0.5*z**2)/(nruns + z**2)

    error = z/(nruns + z**2) * np.sqrt(n_dark*n_bright/nruns + z**4/4)



    freqs = freq[:len(p_ex)]
    probs = p_ex

    return freqs, probs, error, params

def plot_397(rid):
    '''load 397 scan'''

    data, metadata = load_h5(rid)

```

```
    freqs = data['fl_scan.laser_freq']
    counts = data['fl_scan.counts']
    errors = 1/np.sqrt(counts)

    nsteps = sum(np.isfinite(freqs))

    return freqs[:nsteps], counts[:nsteps], errors[:nsteps]

def plot_866(rid):
    '''load 866 scan'''

    data, metadata = load_h5(rid)

    freqs = data['fl_scan.laser_freq']
    counts = data['fl_scan.countsA']
    errors = 1/np.sqrt(counts)

    nsteps = sum(np.isfinite(freqs))

    return freqs[:nsteps], counts[:nsteps], errors[:nsteps]


def plot_comp(rid):
    '''load compensation scan'''

    data, metadata = load_h5(rid)

    return data, metadata
```

Bibliography

[1] W. Paul, "Nobel Lecture: Electromagnetic traps for charged and neutral particles," nobelprize.org (1989), [Accessed at `https://www.nobelprize.org/prizes/physics/1989/paul/lecture` on 20/9/2021].

[2] P. H. Dawson, *Quadrupole Mass Spectrometry and its Applications* (Elsevier, 1976).

[3] J. J. Thomson, "Rays of positive electricity," The London, Edinburgh, and Dublin Philosophical Magazine and Journal of Science **20**, 752–767 (1910).

[4] F. W. Aston, "A positive ray spectrograph," The London, Edinburgh, and Dublin Philosophical Magazine and Journal of Science **38**, 707–714 (1919).

[5] F. M. Penning, "Die glimmentladung bei niedrigem druck zwischen koaxialen zylindern in einem axialen magnetfeld," Physica **3**, 873 – 894 (1936).

[6] J. R. Pierce, *Theory and Design of Electron Beams* (Van Nostrand Company, 1949).

[7] W. Paul, H. P. Reinhard, and U. von Zahn, "The electrical mass filter as a mass spectrometer and isotope separator," Zeitschrift für Physik **152**, 143–182 (1958).

[8] E. Fischer, "Three-dimensional stabilization of charge carriers in a quadrupole field," Zeitschrift für Physik **156**, 1–26 (1959).

[9] H. G. Dehmelt, *Radiofrequency Spectroscopy of Stored Ions I: Storage*, Vol. 3 (Academic Press, 1968) pp. 53 – 72.

[10] D. J. Wineland, R. E. Drullinger, and F. L. Walls, "Radiation-pressure cooling of bound resonant absorbers," Phys. Rev. Lett. **40**, 1639–1642 (1978).

[11] R. Blatt and P. Zoller, "Quantum jumps in atomic systems," European Journal of Physics **9**, 250–256 (1988).

[12] C. Monroe, D. M. Meekhof, B. E. King, and D. J. Wineland, "A 'Schrödinger cat' superposition state of an atom," Science **272**, 1131–1136 (1996).

[13] D. J. Wineland, "Nobel Lecture: Superposition, entanglement, and raising Schrödinger's cat," nobelprize.org (2012), [Accessed at `https://www.nobelprize.org/prizes/physics/2012/wineland/lecture` on 20/09/2021].

[14] F. Diedrich, J. C. Bergquist, Wayne M. Itano, and D. J. Wineland, "Laser cooling to the zero-point energy of motion," Phys. Rev. Lett. **62**, 403–406 (1989).

[15] C. Monroe, D. M. Meekhof, B. E. King, S. R. Jefferts, W. M. Itano, D. J. Wineland, and P. Gould, "Resolved-sideband Raman cooling of a bound atom to the 3d zero-point energy," Phys. Rev. Lett. **75**, 4011–4014 (1995).

[16] J. F. Goodwin, G. Stutter, R. C. Thompson, and D. M. Segal, "Resolved-sideband laser cooling in a Penning trap," Phys. Rev. Lett. **116**, 143002 (2016).

[17] P. Hrmo, M. K. Joshi, V. Jarlaud, O. Corfield, and R. C. Thompson, "Sideband cooling of the radial modes of motion of a single ion in a Penning trap," Phys. Rev. A **100**, 043414 (2019).

[18] K. Wright, K. M. Beck, S. Debnath, J. M. Amini, Y. Nam, N. Grzesiak, J. S. Chen, N. C. Pisenti, M. Chmielewski, C. Collins, K. M. Hudek, J. Mizrahi, J. D. Wong-Campos, S. Allen, J. Apisdorf, P. Solomon, M. Williams, A. M. Ducore, A. Blinov, S. M. Kreikemeier, V. Chaplin, M. Keesan, C. Monroe, and J. Kim, "Benchmarking an 11-qubit quantum computer," Nature Communications **10**, 5464 (2019).

[19] I. Pogorelov, T. Feldker, Ch. D. Marciniak, L. Postler, G. Jacob, O. Krieglsteiner, V. Podlesnic, M. Meth, V. Negnevitsky, M. Stadler, B. Höfer, C. Wächter, K. Lakhmanskiy, R. Blatt, P. Schindler, and T. Monz, "Compact ion-trap quantum computing demonstrator," PRX Quantum **2**, 020343 (2021).

[20] J. Preskill, "Quantum computing 40 years later," arXiv **2106.10522** (2021).

[21] J. R. Powell, "The quantum limit to Moore's law," Proceedings of the IEEE **96**, 1247–1248 (2008).

[22] M. A. Nielsen and I. L. Chuang, *Quantum Computation and Quantum Information* (Cambridge University Press, 2010).

[23] D. E. Deutsch and R. Penrose, "Quantum theory, the Church–Turing principle and the universal quantum computer," Proceedings of the Royal Society of London. A. Mathematical and Physical Sciences **400**, 97–117 (1985).

[24] P. W. Shor, "Polynomial-time algorithms for prime factorization and discrete logarithms on a quantum computer," SIAM J. Comput. **26**, 1484–1509 (1997).

[25] D. E. Deutsch and R. Penrose, "Quantum computational networks," Proceedings of the Royal Society of London. A. Mathematical and Physical Sciences **425**, 73–90 (1989).

[26] W. K. Wootters and W. H. Zurek, "A single quantum cannot be cloned," Nature **299**, 802–803 (1982).

[27] P. W. Shor, "Scheme for reducing decoherence in quantum computer memory," Phys. Rev. A **52**, R2493–R2496 (1995).

[28] D. P. DiVincenzo, "The physical implementation of quantum computation," Fortschritte der Physik **48**, 771–783 (2000).

[29] C. Monroe, R. Raussendorf, A. Ruthven, K. R. Brown, P. Maunz, L.-M. Duan, and J. Kim, "Large-scale modular quantum-computer architecture with atomic memory and photonic interconnects," Phys. Rev. A **89**, 022317 (2014).

[30] B. Lekitsch, S. Weidt, A. G. Fowler, K. Mølmer, S. J. Devitt, C. Wunderlich, and W. K. Hensinger, "Blueprint for a microwave trapped ion quantum computer," Science Advances **3**, e1601540 (2017).

[31] J. D. Wong-Campos, S. A. Moses, K. G. Johnson, and C. Monroe, "Demonstration of two-atom entanglement with ultrafast optical pulses," Phys. Rev. Lett. **119**,

230501 (2017).

[32] V. M. Schäfer, C. J. Ballance, K. Thirumalai, L. J. Stephenson, T. G. Ballance, A. M. Steane, and D. M. Lucas, "Fast quantum logic gates with trapped-ion qubits," Nature **555**, 75–78 (2018).

[33] J. Preskill, "Quantum Computing in the NISQ era and beyond," Quantum **2**, 79 (2018).

[34] J. G. Bohnet, B. C. Sawyer, J. W. Britton, M. L. Wall, A. M. Rey, M Foss-Feig, and J. J. Bollinger, "Quantum spin dynamics and entanglement generation with hundreds of trapped ions," Science **352**, 1297–1301 (2016).

[35] J. Zhang, G. Pagano, P. W. Hess, A. Kyprianidis, P. Becker, H. Kaplan, A. V. Gorshkov, Z. X. Gong, and C. Monroe, "Observation of a many-body dynamical phase transition with a 53-qubit quantum simulator," Nature **551**, 601–604 (2017).

[36] Y. Nam, J. S. Chen, N. C. Pisenti, K. Wright, C. Delaney, D. Maslov, K. R. Brown, S. Allen, J. M. Amini, J. Apisdorf, K. M. Beck, A. Blinov, V. Chaplin, M. Chmielewski, C. Collins, S. Debnath, K. M. Hudek, A. M. Ducore, M. Keesan, S. M. Kreikemeier, J. Mizrahi, P. Solomon, M. Williams, J. D. Wong-Campos, D. Moehring, C. Monroe, and J. Kim, "Ground-state energy estimation of the water molecule on a trapped-ion quantum computer," NPJ Quantum Information **6**, 33 (2020).

[37] J. I. Cirac and P. Zoller, "Quantum computations with cold trapped ions," Phys. Rev. Lett. **74**, 4091–4094 (1995).

[38] A. Sørensen and K. Mølmer, "Quantum computation with ions in thermal motion," Phys. Rev. Lett. **82**, 1971–1974 (1999).

[39] C. A. Sackett, D. Kielpinski, B. E. King, C. Langer, V. Meyer, C. J. Myatt, M. Rowe, Q. A. Turchette, W. M. Itano, D. J. Wineland, and C. Monroe, "Experimental entanglement of four particles," Nature **404**, 256–259 (2000).

[40] F. Schmidt-Kaler, S. Gulde, M. Riebe, T. Deuschle, A. Kreuter, G. Lancaster, C. Becher, J. Eschner, H. Häffner, and R. Blatt, "The coherence of qubits based on single Ca^+ ions," Journal of Physics B: Atomic, Molecular and Optical Physics **36**, 623–636 (2003).

[41] D. Leibfried, B. DeMarco, V. Meyer, D. Lucas, M. Barrett, J. Britton, W. M. Itano, B. Jelenković, C. Langer, T. Rosenband, and D. J. Wineland, "Experimental demonstration of a robust, high-fidelity geometric two ion-qubit phase gate," Nature **422**, 412–415 (2003).

[42] D. Leibfried, E. Knill, S. Seidelin, J. Britton, R. B. Blakestad, J. Chiaverini, D. B. Hume, W. M. Itano, J. D. Jost, C. Langer, R. Ozeri, R. Reichle, and D. J. Wineland, "Creation of a six-atom 'Schrödinger cat' state," Nature **438**, 639–642 (2005).

[43] T. Monz, P. Schindler, J. T. Barreiro, M. Chwalla, D. Nigg, W. A. Coish, M. Harlander, W. Hänsel, M. Hennrich, and R. Blatt, "14-qubit entanglement: Creation and coherence," Phys. Rev. Lett. **106**, 130506 (2011).

[44] C. J. Ballance, T. P. Harty, N. M. Linke, M. A. Sepiol, and D. M. Lucas, "High-

fidelity quantum logic gates using trapped-ion hyperfine qubits," Phys. Rev. Lett. **117**, 060504 (2016).

[45] J. P. Gaebler, T. R. Tan, Y. Lin, Y. Wan, R. Bowler, A. C. Keith, S. Glancy, K. Coakley, E. Knill, D. Leibfried, and D. J. Wineland, "High-fidelity universal gate set for ^{9}Be$^+$ ion qubits," Phys. Rev. Lett. **117**, 060505 (2016).

[46] M. Sameti, J. Lishman, and F. Mintert, "Strong-coupling quantum logic of trapped ions," Phys. Rev. A **103**, 052603 (2021).

[47] R. Landauer, "Irreversibility and heat generation in the computing process," IBM Journal of Research and Development **5**, 183–191 (1961).

[48] A. Bérut, A. Arakelyan, A. Petrosyan, S. Ciliberto, R. Dillenschneider, and E. Lutz, "Experimental verification of Landauer's principle linking information and thermodynamics," Nature **483**, 187–189 (2012).

[49] E. Magesan, J. M. Gambetta, and J. Emerson, "Scalable and robust randomized benchmarking of quantum processes," Phys. Rev. Lett. **106**, 180504 (2011).

[50] J. P. Gaebler, A. M. Meier, T. R. Tan, R. Bowler, Y. Lin, D. Hanneke, J. D. Jost, J. P. Home, E. Knill, D. Leibfried, and D. J. Wineland, "Randomized benchmarking of multiqubit gates," Phys. Rev. Lett. **108**, 260503 (2012).

[51] P. K. Ghosh, *Ion Traps* (Clarendon Press, 1995).

[52] J. T. Barreiro, M. Müller, P. Schindler, D. Nigg, T. Monz, M. Chwalla, M. Hennrich, C. F. Roos, P. Zoller, and R. Blatt, "An open-system quantum simulator with trapped ions," Nature **470**, 486–491 (2011).

[53] K. Kim, M. S. Chang, S. Korenblit, R. Islam, E. E. Edwards, J. K. Freericks, G. D. Lin, L. M. Duan, and C. Monroe, "Quantum simulation of frustrated ising spins with trapped ions," Nature **465**, 590–593 (2010).

[54] B. P. Lanyon, C. Hempel, D. Nigg, M. Müller, R. Gerritsma, F. Zähringer, P. Schindler, J. T. Barreiro, M. Rambach, G. Kirchmair, M. Hennrich, P. Zoller, R. Blatt, and C. F. Roos, "Universal digital quantum simulation with trapped ions," Science **334**, 57–61 (2011).

[55] T. Monz, D. Nigg, E. A. Martinez, M. F. Brandl, P. Schindler, R. Rines, S. X. Wang, I. L. Chuang, and R. Blatt, "Realization of a scalable shor algorithm," Science **351**, 1068–1070 (2016).

[56] A. Bermudez, X. Xu, R. Nigmatullin, J. O'Gorman, V. Negnevitsky, P. Schindler, T. Monz, U. G. Poschinger, C. Hempel, J. Home, F. Schmidt-Kaler, M. Biercuk, R. Blatt, S. Benjamin, and M. Müller, "Assessing the progress of trapped-ion processors towards fault-tolerant quantum computation," Phys. Rev. X **7**, 041061 (2017).

[57] S. Jain, J. Alonso, M. Grau, and J. P. Home, "Scalable arrays of micro-Penning traps for quantum computing and simulation," Phys. Rev. X **10**, 031027 (2020).

[58] L. S. Brown and G. Gabrielse, "Geonium theory: Physics of a single electron or ion in a Penning trap," Rev. Mod. Phys. **58**, 233–311 (1986).

[59] R. C. Thompson and D. C. Wilson, "The motion of small numbers of ions in a Penning trap," Zeitschrift für Physik D **42**, 271–277 (1997).

[60] W. M. Itano and D. J. Wineland, "Laser cooling of ions stored in harmonic and Penning traps," Phys. Rev. A **25**, 35–54 (1982).

[61] E. S. Phillips, R. J. Hendricks, A. M. Abdulla, H. Ohadi, D. R. Crick, K. Koo, D. M. Segal, and R. C. Thompson, "Dynamics of axialized laser-cooled ions in a Penning trap," Phys. Rev. A **78**, 032307 (2008).

[62] S. Bharadia, *Towards laser spectroscopy of highly charged ions*, Ph.D. thesis, Imperial College London (2011).

[63] M. Vogel and W. Quint, "Trap-assisted precision spectroscopy of highly charged ions," J. Phys. B **42**, 154016 (2009).

[64] S. Bharadia, M. Vogel, D. M. Segal, and R. C. Thompson, "Dynamics of laser-cooled Ca^+ ions in a Penning trap with a rotating wall," App. Phys. B **107**, 1105–1115 (2012).

[65] S. Mavadia, J. F. Goodwin, G. Stutter, S. Bharadia, D. R. Crick, D. M. Segal, and R. C. Thompson, "Control of the conformations of ion Coulomb crystals in a Penning trap," Nature Comms **4**, 2571 (2013).

[66] S. Mavadia, G. Stutter, J. F. Goodwin, D. R. Crick, R. C. Thompson, and D. M. Segal, "Optical sideband spectroscopy of a single ion in a Penning trap," Phys. Rev. A **89**, 032502 (2014).

[67] S. Mavadia, *Motional sideband spectra and Coulomb crystals in a Penning trap*, Ph.D. thesis, Imperial College London (2013).

[68] J. F. Goodwin, *Sideband cooling to the quantum ground state in a Penning trap*, Ph.D. thesis, Imperial College London (2015).

[69] G. Stutter, P. Hrmo, V. Jarlaud, M. K. Joshi, J. F. Goodwin, and R. C. Thompson, "Sideband cooling of small ion Coulomb crystals in a Penning trap," Journal of Modern Optics **65**, 549–559 (2018).

[70] V. Jarlaud, *Sideband cooling of ion Coulomb crystals in a Penning trap*, Ph.D. thesis, Imperial College London (2018).

[71] P. Hrmo, *Ground state cooling of the radial motion of a single ion in a Penning trap and coherent manipulation of small numbers of ions*, Ph.D. thesis, Imperial College London (2018).

[72] W. Paul, "Electromagnetic traps for charged and neutral particles," Rev. Mod. Phys. **62**, 531–540 (1990).

[73] K. Deng, H. Che, Y. Lan, Y. P. Ge, Z. T. Xu, W. H. Yuan, J. Zhang, and Z. H. Lu, "Design of blade-shaped-electrode linear ion traps with reduced anharmonic contributions," Journal of Applied Physics **118**, 113106 (2015).

[74] D. Gerlich, *Inhomogeneous RF Fields: A Versatile Tool for the Study of Processes with Slow Ions* (John Wiley and Sons, Ltd, 2007) pp. 1–176.

[75] E. M. Landau, L. D. Lifshitz, *Mechanics* (Pergamon Press Ltd., Oxford, 1960).

[76] D. J. Douglas, A. S. Berdnikov, and N. V. Konenkov, "The effective potential for ion motion in a radio frequency quadrupole field revisited," International Journal of Mass Spectrometry **377**, 345 – 354 (2015).

[77] D. J. Berkeland, J. D. Miller, J. C. Bergquist, W. M. Itano, and D. J. Wineland, "Minimization of ion micromotion in a paul trap," Journal of Applied Physics **83**, 5025–5033 (1998).

[78] F. Schmidt-Kaler, H. Häffner, S. Gulde, M. Riebe, G. Lancaster, T. Deuschle, C. Becher, W. Hänsel, J. Eschner, C. F. Roos, and R. Blatt, "How to realize a universal quantum gate with trapped ions," Applied Physics B **77**, 789–796 (2003).

[79] R. J. Reid, "Procedures for the cleaning of vacuum items," ed.ac.uk (2003), [Accessed at `https://www2.ph.ed.ac.uk/~td/isol-srs/spc-003-Cleaning%20of%20Vacuum%20Items.pdf` on 6/8/2021].

[80] J. D. Siverns, L. R. Simkins, S. Weidt, and W. K. Hensinger, "On the application of radio frequency voltages to ion traps via helical resonators," Applied Phys. B **107**, 921–934 (2012).

[81] R. S. Van Dyck, P. B. Schwinberg, and H. G. Dehmelt, "New high-precision comparison of electron and positron g factors," Phys. Rev. Lett. **59**, 26–29 (1987).

[82] D. Hanneke, S. Fogwell, and G. Gabrielse, "New measurement of the electron magnetic moment and the fine structure constant," Phys. Rev. Lett. **100**, 120801 (2008).

[83] J. DiSciacca and G. Gabrielse, "Direct measurement of the proton magnetic moment," Phys. Rev. Lett. **108**, 153001 (2012).

[84] H. Nagahama, C. Smorra, S. Sellner, J. Harrington, T. Higuchi, M. J. Borchert, T. Tanaka, M. Besirli, A. Mooser, G. Schneider, K. Blaum, Y. Matsuda, C. Ospelkaus, W. Quint, J. Walz, Y. Yamazaki, and S. Ulmer, "Sixfold improved single particle measurement of the magnetic moment of the antiproton," Nature Comms **8**, 14084 (2017).

[85] W. Neuhauser, M. Hohenstatt, P. E. Toschek, and H. G. Dehmelt, "Localized visible Ba^+ mono-ion oscillator," Phys. Rev. A **22**, 1137–1140 (1980).

[86] D. J. Heinzen and D. J. Wineland, "Quantum-limited cooling and detection of radio-frequency oscillations by laser-cooled ions," Phys. Rev. A **42**, 2977–2994 (1990).

[87] M. Bohman, A. Mooser, G. Schneider, N. Schön, M. Wiesinger, J. Harrington, T. Higuchi, H. Nagahama, C. Smorra, S. Sellner, K. Blaum, Y. Matsuda, W. Quint, J. Walz, and S. Ulmer, "Sympathetic cooling of protons and antiprotons with a common endcap Penning trap," Journal of Modern Optics **65**, 568–576 (2018).

[88] T. Meiners, M. Niemann, A. G. Paschke, J. Mielke, A. Idel, M. Borchert, K. Voges, A. Bautista-Salvador, S. Ulmer, and C. Ospelkaus, "Towards quantum logic inspired cooling and detection for single (anti-)protons," in *Proceedings of the 12th international conference on low energy antiproton physics (LEAP2016)* (2017).

[89] S. S. Liaw, "Ab initio calculation of the lifetimes of $4p$ and $3d$ levels of Ca^+," Phys. Rev. A **51**, R1723–R1726 (1995).

[90] D. F. V. James, "Quantum dynamics of cold trapped ions with application to quantum computation," Applied Physics B **66**, 181–190 (1998).

[91] M. Chwalla, J. Benhelm, K. Kim, G. Kirchmair, T. Monz, M. Riebe, P. Schindler, A. S. Villar, W. Hänsel, C. F. Roos, R. Blatt, M. Abgrall, G. Santarelli, G. D. Rovera,

and Ph. Laurent, "Absolute frequency measurement of the $^{40}\text{Ca}^{+}$ $4s\ ^2s_{1/2} - 3d\ ^2d_{5/2}$ clock transition," Phys. Rev. Lett. **102**, 023002 (2009).

[92] C. J. Foot, *Atomic Physics* (Oxford University Press, 2005).

[93] P. van der Straten and H. Metcalf, *Atoms and Molecules Interacting with Light: Atomic Physics for the Laser Era* (Cambridge University Press, 2016).

[94] D. Leibfried, R. Blatt, C. Monroe, and D. J. Wineland, "Quantum dynamics of single trapped ions," Rev. Mod. Phys. **75**, 281–324 (2003).

[95] D. J. Wineland and W. M. Itano, "Laser cooling," Physics Today **40**, 34–40 (1987).

[96] G. Savard, St. Becker, G. Bollen, H. J. Kluge, R. B. Moore, Th. Otto, L. Schweikhard, H. Stolzenberg, and U. Wiess, "A new cooling technique for heavy ions in a Penning trap," Physics Letters A **158**, 247–252 (1991).

[97] C. Lee, "Early stage assessment," Unpublished (2019), see future Ph.D. thesis.

[98] E. D. Black, "An introduction to Pound–Drever–Hall laser frequency stabilization," American Journal of Physics **69**, 79–87 (2001).

[99] M. K. Joshi, *Coherent dynamics of trapped ions within and outside the Lamb-Dicke regime*, Ph.D. thesis, Imperial College London (2018).

[100] J. Mosca Toba, *Design of an imaging system and implementation of photoionisation for a linear Paul trap*, Master's thesis, Imperial College London (2019).

[101] T. G. Ballance, J. F. Goodwin, B. Nichol, L. J. Stephenson, C. J. Ballance, and D. M. Lucas, "A short response time atomic source for trapped ion experiments," Review of Scientific Instruments **89**, 053102 (2018).

[102] J. Lishman, *Robust coherence and entanglement creation in trapped ions*, Ph.D. thesis, Imperial College London (2022).

[103] Edwin B. Wilson, "Probable inference, the law of succession, and statistical inference," Journal of the American Statistical Association **22**, 209–212 (1927).

[104] A. H. Tavabi, C. B. Boothroyd, E. Yücelen, S. Frabboni, G. C. Gazzadi, R. E. Dunin-Borkowski, and G. Pozzi, "The Young–Feynman controlled double-slit electron interference experiment," Scientific Reports **9**, 10458 (2019).

[105] S. Frabboni, A. Gabrielli, G. C. Gazzadi, F. Giorgi, G. Matteucci, G. Pozzi, N. Semprini Cesari, M. Villa, and A. Zoccoli, "The Young–Feynman two-slits experiment with single electrons: Build-up of the interference pattern and arrival-time distribution using a fast-readout pixel detector," Ultramicroscopy **116**, 73–76 (2012).

[106] S. Frabboni, G. C. Gazzadi, and G. Pozzi, "Nanofabrication and the realization of Feynman's two-slit experiment," Applied Physics Letters **93**, 073108 (2008).

[107] C. K. Hong, Z. Y. Ou, and L. Mandel, "Measurement of subpicosecond time intervals between two photons by interference," Phys. Rev. Lett. **59**, 2044–2046 (1987).

[108] O. Nairz, M. Arndt, and A. Zeilinger, "Quantum interference experiments with large molecules," American Journal of Physics **71**, 319–325 (2003).

[109] M. Hillery, "Coherence as a resource in decision problems: The Deutsch–Jozsa algorithm and a variation," Phys. Rev. A **93**, 012111 (2016).

[110] H. Shi, S. Liu, X. Wang, W. Yang, Z. Yang, and H. Fan, "Coherence depletion in the grover quantum search algorithm," Phys. Rev. A **95**, 032307 (2017).

[111] W. H. Miller, "Perspective: Quantum or classical coherence?" The Journal of Chemical Physics **136**, 210901 (2012).

[112] R. Horodecki, "Quantum information," arXiv **2103.07712** (2021).

[113] F. Levi and F. Mintert, "A quantitative theory of coherent delocalization," New Journal of Physics **16**, 033007 (2014).

[114] D. Girolami, "Observable measure of quantum coherence in finite dimensional systems," Phys. Rev. Lett. **113**, 170401 (2014).

[115] A. Streltsov, G. Adesso, and M. B. Plenio, "Colloquium: Quantum coherence as a resource," Rev. Mod. Phys. **89** (2017).

[116] X. Yuan, H. Zhou, Z. Cao, and X. Ma, "Intrinsic randomness as a measure of quantum coherence," Phys. Rev. A **92**, 022124 (2015).

[117] T. Baumgratz, M. Cramer, and M. B. Plenio, "Quantifying coherence," Phys. Rev. Lett. **113**, 140401 (2014).

[118] A. Winter and D. Yang, "Operational resource theory of coherence," Phys. Rev. Lett. **116**, 120404 (2016).

[119] M. Ringbauer, T. R. Bromley, M. Cianciaruso, L. Lami, W. Y. S. Lau, G. Adesso, A. G. White, A. Fedrizzi, and M. Piani, "Certification and quantification of multilevel quantum coherence," Phys. Rev. X **8**, 041007 (2018).

[120] K. von Prillwitz, Ł. Rudnicki, and F. Mintert, "Contrast in multipath interference and quantum coherence," Phys. Rev. A **92**, 052114 (2015).

[121] B. Dive, N. Koukoulekidis, S. Mousafeiris, and F. Mintert, "Characterization of multilevel quantum coherence without ideal measurements," Phys. Rev. Research **2**, 013220 (2020).

[122] O. Corfield, J. Lishman, C. Lee, J. Mosca Toba, G. Porter, J. M. Heinrich, S. C. Webster, F. Mintert, and R. C. Thompson, "Certifying multilevel coherence in the motional state of a trapped ion," PRX Quantum **2**, 040359 (2021).

[123] W. Zurek, "Quantum darwinism," Nature Physics **5**, 181–188 (2009).

[124] N. Ramsey, "Nobel Lecture: Experiments with separated oscillatory fields and hydrogen masers," nobelprize.org (1989), [Accessed at `https://www.nobelprize.org/prizes/physics/1989/ramsey/lecture` on 11/10/2021].

[125] J. Preskill, "Notes on noise," caltech.edu (2021), [Accessed at `http://theory.caltech.edu/~preskill/papers/decoherence_notesv2.pdf` on 13/11/2021].

[126] S. Szalay, "Multipartite entanglement measures," Phys. Rev. A **92**, 042329 (2015).

[127] S. A. Gardiner, J. I. Cirac, and P. Zoller, "Nonclassical states and measurement of general motional observables of a trapped ion," Phys. Rev. A **55**, 1683–1694 (1997).

[128] T. P. Harty, D. T. C. Allcock, C. J. Ballance, L. Guidoni, H. A. Janacek, N. M. Linke, D. N. Stacey, and D. M. Lucas, "High-fidelity preparation, gates, memory, and readout of a trapped-ion quantum bit," Phys. Rev. Lett. **113**, 220501 (2014).